Adv Polym Sci (2010) 230: 1–71
DOI:10.1007/12_2009_13

Published online: 26 August 2009

Shear-Induced Transitions and Instabilities in Surfactant Wormlike Micelles

Sandra Lerouge and Jean-François Berret

Abstract In this review, we report recent developments on the shear-induced transitions and instabilities found in surfactant wormlike micelles. The survey focuses on the nonlinear shear rheology and covers a broad range of surfactant concentrations, from the dilute to the liquid-crystalline states and including the semidilute and concentrated regimes. Based on a systematic analysis of many surfactant systems, the present approach aims to identify the essential features of the transitions. It is suggested that these features define classes of behaviors. The review describes three types of transitions and/or instabilities: the shear-thickening found in the dilute regime, the shear-banding which is linked in some systems to the isotropic-to-nematic transition, and the flow-aligning and tumbling instabilities characteristic of nematic structures. In these three classes of behaviors, the shear-induced transitions are the result of a coupling between the internal structure of the fluid and the flow, resulting in a new mesoscopic organization under shear. This survey finally highlights the potential use of wormlike micelles as model systems for complex fluids and for applications.

Keywords Instabilities under shear · Lyotropic mesophases · Shear-banding · Shear-thickening · Surfactant · Viscoelasticity · Wormlike micelles

Contents

S. Lerouge and J.-F. Berret (✉)
Laboratoire Matière et Systèmes Complexes (MSC), UMR 7057 CNRS-Université Paris-Diderot, 10 rue Alice Domon et Léonie Duquet, F-75205 Paris Cedex 13, France
e-mail: sandra.lerouge@univ-paris-diderot.fr; jean-francois.berret@univ-paris-diderot.fr

Abbreviations and Notations

$Al(NO_3)_3$	Aluminum nitrate
$AlCl_3$	Aluminum chloride
CP/Sal	Cetylpyridinium salicylate
CPCl	Cetylpyridinium chloride
$CPClO_3$	Cetylpyridinium chlorate
C_8F_{17}	Perfluorooctyl butane trimethylammonium bromide
$C_{12}E_5$	Penta(ethylene glycol) monododecyl ether
C_{12}TAB	Dodecyltrimethylammonium bromide
C_{14}TAB	Tetradecyltrimethylammonium bromide
C_{14}DMAO	Tetradecyldimethylamine oxide
C_{16}TAB	Hexadecyltrimethylammonium bromide
C_{16}TAC	Hexadecyltrimethylammonium chloride
C_{18}TAB	Octadecyltrimethylammonium bromide
C_{18}-C_8DAB	Hexadecyloctyldimethylammonium bromide
C_nTAB	Alkyltrimethylammonium bromide
CTAHNC	Cetyltrimethylammonium 3-hydroxy-2-naphthalenecarboxylate
CTAT	Hexadecyltrimethylammonium *p*-toluenesulfonate
CTAVB	Cetyltrimethylammonium benzoate
Dec	Decanol
DJS	Diffusive Johnson–Segalman
DLS	Dynamic light scattering
DR	Drag reduction
EHAC	Erucyl bis(hydroxyethyl)methylammonium chloride
FB	Flow birefringence
FI	Faraday instability
Gemini 12-2-12	Ethane diyl-1,2-bis-(dodecyl dimethylammonium bromide)

Hex	Hexanol
HPC	Hydroxypropyl cellulose
I/N	Isotropic-to-nematic
KBr	Potassium bromide
LAPB	Laurylamidopropyl betaine
LSI	Light scattering imaging
LCP	Liquid crystalline polymer
NaCl	Sodium chloride
NaClBz	Sodium chlorobenzoate
$NaClO_3$	Sodium chlorate
$NaNO_3$	Sodium nitrate
NaSal	Sodium salicylate
NaTos	Sodium *p*-toluenesulfonate or sodium tosylate
NH_4Cl	Ammonium chloride
NMR	Nuclear magnetic resonance
PBLG	Poly(benzyl-L-glutamate)
PEO	Poly(ethylene oxide)
PIV	Particle image velocimetry
PTV	Particle tracking velocimetry
SANS	Small-angle neutron scattering
SALS	Small-angle light scattering
SAXS	Small-angle X-ray scattering
SDBS	Sodium dodecyl benzyl sulfonate
SDES	Sodium dodecyl trioxyethylene sulfate
SdS	Sodium decylsulfate
SDS	Sodium dodecyl sulfate
SIP	Shear-induced phase
SIS	Shear-induced structure
TTAA	*Tris*(2-hydroxyethyl)-tallowalkyl ammonium acetate
USV	Ultrasonic velocimetry

1 Introduction

Wormlike micelles are elongated and semiflexible aggregates resulting from the self-assembly of surfactant molecules in aqueous solutions. Wormlike micellar solutions have received considerable attention during the past few decades because of their remarkable structural and rheological properties.

Sixty years ago, Debye and his group in Cornell undertook an extensive study of surfactant solutions using the light scattering technique. The goal of these investigations was to measure the dissymmetry of scattered light in order to gain information regarding the molecular weight and thereby the shape of surfactant aggregates. The dissymmetry of scattered light was defined as the intensity ratio at two scattering angles far apart from each other. If this ratio was one, the micelles were assumed to

be spherical; if it increased, the micelles were assumed to grow in size. In a famous paper, Debye and Anacker had discovered that the addition of an inorganic salt, potassium bromide, to aqueous solutions of hexadecyltrimethylammonium bromide caused the colloidal aggregates to increase in size [1]. Based on these dissymmetry experiments, it was suggested that the micelles undergo a morphological transition, from spherical aggregates at low salt content to rodlike aggregates at high salt content. More than half a century later, the very same systems, now known as wormlike micelles, continue to attract interest from a broad scientific community.

Going from the structure to the rheology was not a straightforward path. One important contribution after that of Debye was that of Nash who mapped viscoelastic regions of surfactant solutions again using hexadecyltrimethylammonium bromide and various naphthalene derivatives. The viscoelasticity was determined visually by looking at how fast a swirl applied by hand to a solution decayed with time [2]. Some years later, Gravsholt established that other additives, such as salicylate or chlorobenzoate counterions, could be solubilized by the micelles and efficiently promote their uniaxial growth [3]. It was proposed that the viscoelasticity of these solutions had the same origin as that of polymer solutions, namely entanglements and reptation.

In the early 1980s, as more and more groups were involved in this research, discoveries were made at a faster pace. By a combination of light scattering, rheology and magnetic birefringence, it was first shown that, under certain conditions, cylindrical micelles could be very long, up to 1 μm in contour length, and flexible [4–10]. The terminology introduced was that of giant [5, 11, 12] or wormlike [6, 8–10] micelles, instead of rodlike aggregates some years before. For several surfactants, Ikeda and collaborators reported electron microscopy images showing thread-like and tortuous filaments, later referred to as worms [8, 9]. Again, using light scattering experiments, Candau and his group demonstrated the existence of a cross-over between dilute and semidilute regimes and of scaling laws as a function of the concentration, two features that were known from polymers [7, 13, 14]. These authors pointed out a formal analogy between surfactant wormlike micelles and polymer solutions. This analogy was completed by the extensive investigations of phase behaviors of surfactant aqueous solutions, and the evidence of isotropic-to-nematic and a nematic-to-hexagonal transitions at high concentrations [12, 15–18]. Figure 1 provides a schematic illustration of the different concentration regimes that will be surveyed in the present review. The analogy with polymers, as well as a marked viscoelasticity, attracted attention from rheologists, who were at first interested in the linear mechanical response of these fluids.

A decisive step towards the description of the micellar dynamics was taken with the first quantitative measurements of the linear viscoelastic response of these solutions. The pioneering works were those of Rehage, Hoffmann, Shikata, and Candau and their coworkers [14, 19–33]. The most fascinating result was that the viscoelasticity of entangled wormlike micelles was characterized by a single exponential in the response function. The stress relaxation function $G(t)$ was found of the form $G(t) = G_0 \exp(-t/\tau_R)$ over a broad temporal range, where G_0 denotes the elastic modulus and τ_R is the relaxation time. Since then, this property was found repeatedly

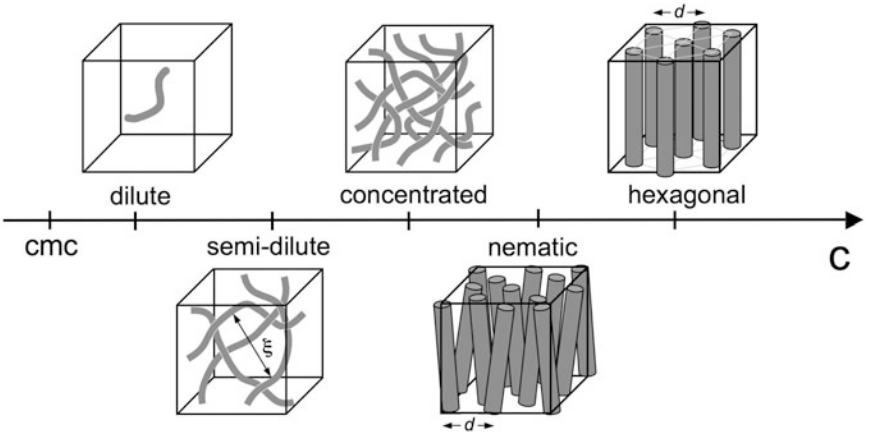

Fig. 1 Illustrations of the different concentrations regimes encountered in wormlike micellar solutions with increasing concentration. ξ is the mesh size of the entangled network in the semidilute regime and d denotes the average distance between colinear micelles in the concentrated isotropic, nematic and hexagonal phases. An estimate of d can be gained from the position of the structure peak in the scattering function

in semidilute wormlike micellar solutions. This rule has become so general that it is now recognized that a single relaxation time in the linear rheology is a strong indication of the wormlike character of self-assembled structures. A simple viscoelastic behavior, together with the fact that micellar solutions are easy to prepare and not susceptible to aging or degradation, have incited several groups to utilize wormlike micelles as reference for the testing of new rheological techniques [34–39].

On the theoretical side, the challenge was to account for this unique time of the mechanical response. This was done by Cates and coworkers in the late 1980s with the reptation-reaction kinetics model [40]. The reptation-reaction kinetics model is based on the assumption that the breaking and recombination events of the chains are coupled to the reptation [41], and as such accelerate the overall relaxation of the stress. In the fast breaking limit, a given micelle undergoes several scission and recombination reactions on the time scale of the reptation. Thus, all initial deformations of the tube segments relax at the same rate, this rate being driven by the reversible scission.

In the present review, we focus on the shear-induced transitions and instabilities that were disclosed in wormlike micellar systems during the last decade or so. The thermodynamics, structure, and rheology of the aggregates at rest or under small deformation have been reviewed many times in the past [19, 25, 28, 42–44], and they will not be treated here. Our survey of the nonlinear rheology now covers all concentration regimes, from the dilute to the liquid-crystalline states, including the semidilute and concentrated regimes (Fig. 1). The present approach aims to demonstrate that the features of the shear instabilities are specific to a concentration regime. Sometimes, the characteristics of a transition extend over a broader concentration

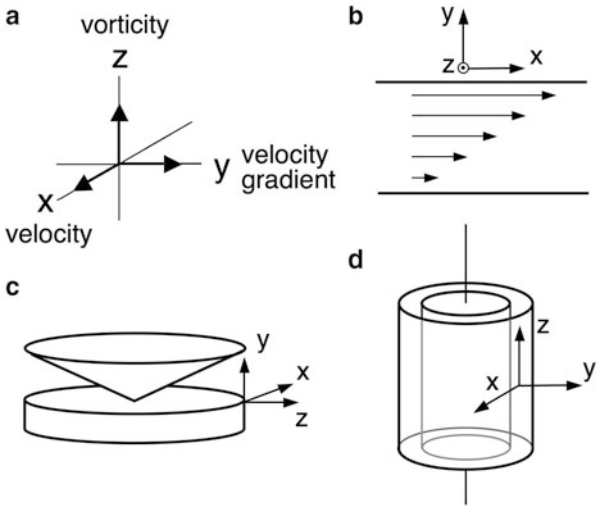

Fig. 2 (**a**) Conventions adopted in this review for the velocity, velocity gradient and vorticity axes characterizing shear flows. Most common geometries of shearing devices producing shear flows: (**b**) planar Couette, (**c**) cone-and-plate, (**d**) cylindrical Couette

range. This is the case for the shear-thickening that was evidenced in the dilute and semidilute regimes. Another goal is to establish correspondences between the shear-induced and the equilibrium phases. A good illustration is that of the isotropic-to-nematic transition, for which the induced nematic exhibits the same orientation and rheological properties as the nematic phase found in the equilibrium phase diagram at high volume fraction.

Although elongational flows have also been imposed on semidilute solutions [45–49], the review will focus essentially on shear flows. The most common devices for shear are the cylindrical Couette and the cone-and-plate geometries (Fig. 2). In a cylindrical Couette system, the sample is contained between two concentric cylinders and the shear is applied by rotating the inner or outer cylinder. If the inner cylinder is rotated, inertia effects may cause a transition from laminar flow to Taylor vortex flow at high shear rates [50]. As for the results discussed in the review, the Reynolds numbers remained below or even much below than that of the Taylor instability. Compared to Couette systems, cone-and-plate devices have more uniform stress, provided the cone angle is small. Figure 2 also specifies the geometrical conventions used throughout the review for the velocity, velocity gradient, and vorticity directions. Another convention concerns the surfactant concentrations. Due to the fact that wormlike micelles were studied by scientists from various research fields, the surfactant concentrations appear in the literature with different units, including molar concentration, volume fraction, weight percent, or weight per volume. In order to allow comparison between different surfactant systems, we have adopted the following rule. We have kept the units used by the authors in reference to their work, and we have added, when necessary, the value of the weight percent concentration

c (units wt). For ternary systems made of a surfactant and an additive (this additive being a hydrotope, a cosurfactant, or an alcohol molecule), c denotes the total surfactant and additive concentration. The molar ratio between additive and surfactant is expressed as R.

The review is organized as follows: Sect. 2 deals with the shear-thickening behavior found in dilute and very dilute surfactant solutions. Section 3 examines the shear-banding instability and the isotropic-to-nematic transition revealed in the semidilute and concentrated regimes, respectively. The last part focuses on the wormlike micellar nematics under shear, and emphasizes the analogy with liquid-crystalline polymers.

2 Shear-Thickening in Dilute Micellar Solutions

2.1 Introduction

Among the rich variety of shear-induced instabilities and transitions encountered in surfactant systems, one of the most puzzling is the shear-thickening effect observed in dilute or very dilute solutions. This transition was first noticed by Rehage and Hoffmann [52] in 1981 for the system cetylpyridinium salicylate (CP/Sal) at a molar concentration of 0.9 mM ($c = 0.04$ wt. %). In their original work, the shear stress was recorded as a function of time over several minutes, and it revealed an unexpected behavior. Above a critical shear rate, the transient stress exhibited a period of induction during which the viscosity increased and then stabilized around 10 times the viscosity of water. This early evidence of the shear-thickening has been reproduced in Fig. 3. The phenomenon was explained by postulating the formation of a supramolecular structure during flow [51, 52].

In the same decade, shear-thickening solutions have attracted much interest because of their potential applications in fluid mechanics. In a number of practical

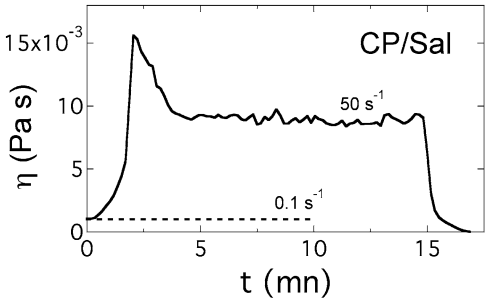

Fig. 3 Shear viscosity as a function of time for equimolar cetylpyridinium salicylate (CP/Sal) at 0.9 mM ($c = 0.04$ wt. %) and temperature $T = 20\,^{\circ}\mathrm{C}$. The transient response at $\dot{\gamma} = 0.1\,\mathrm{s}^{-1}$ exhibits a regular steady behavior for such dilute solution, whereas the response at $50\,\mathrm{s}^{-1}$ shows a period of induction during which the viscosity increases and then stabilizes around ten times the viscosity of water. Figure reprinted with permission from [51]

situations such as fire-fighting operations and transportation of fluids along cylindrical pipes, turbulence occurs near the solid surface and increases the energy losses associated to the flow. It was suggested that additives dispersed in water, e.g., polymers or surfactant, could diminish considerably the turbulent skin friction [53]. Bewerdorff and coworkers have shown that some surfactants reduced effectively the friction factor in turbulent pipe flows [54–56]. Using tetradecyltrimethylammonium with salicylate counterions at concentrations as low as 0.1 wt. %, these authors were able to correlate the drag reduction to the increase of viscosity at high shear rates. Since these early studies, the interest in this transition has increased, especially in the context of the study of complex fluids under shear flow.

In this part, we are dealing with the shear-thickening transition in dilute surfactant solutions. Only solutions with zero-shear viscosity close to that of the solvent and for which no apparent viscoelasticity is observed at rest will be considered. Systems showing both viscoelasticity and shear-thickening have also been found and will be evoked in the part devoted to the semidilute regime.

The features of the shear-thickening transition are summarized as follows:

1. Shear-thickening occurs for surfactants that self-assemble into cylindrical micelles.
2. Under steady shear, above a critical shear rate, the shear viscosity increases as a new and more viscous phase develops. This shear-induced state is called SIS for shear-induced structure [55] or SIP for shear-induced phase [57] in the literature.
3. An induction time is necessary to induce the SIS. At steady state, the stress displays fluctuations that are larger than the instrumental noise response.
4. In the shear-induced state, the solutions are birefringent and exhibit a strongly anisotropic scattering in light and neutron experiments. This anisotropy is compatible with a strong alignment of the shear-induced structures in the flow.
5. The shear stress vs shear rate curve depends on the geometry of shearing cells, and also of the thermal and shear histories experienced by the fluid prior to rheological testing.

In the following (Sect. 2.2) we will first provide a list of surfactant molecules that exhibit shear-induced structures in accordance with points 1–5 and then describe the phenomenology of the transition. The rheology (Sect. 2.3), the orientation properties (Sect. 2.4), and the structure of the flow field (Sect. 2.5) for these fluids will then be examined.

2.2 Shear-Thickening Surfactants

In comparison with the total number of surfactants available by now, only a few of them exhibit a shear-thickening transition in accordance with points 1–5 above. Table 1 lists these systems, with their counterions and/or their hydrotopes. In Table 1 it can be seen that all the surfactants are cationic and that the number of carbon atoms ranges from 13 to 18 per elementary charge. Most of the rheological

Table 1 List of surfactants and additives found to exhibit shear-thickening described by points 1–5. Column 4 makes an inventory of the experimental techniques employed to investigate the SIS

Surfactant	Additive	Salt	Experiment	References
CPCl	NaSal		FB	(a)
C_{14}TAB	NaSal		SANS, FB, DR	(b)
C_{16}TAB	NaSal		FI, FB, DR, SALS, PIV	(c)
C_{16}TAB	NaTos (*)		SANS, FB	(d)
C_{16}TAC	NaClBz		DR	(e)
C_{18}TAB	NaSal			(f)
C_{14}DMAO	SDS		SANS, FB, SALS	(g)
Gemini 12-2-12		Br^-	SANS, FB, SALS	(h)
TTAA	NaSal		LSI, PIV, DR	(i)
C_8F_{17}		Br^-		(j)

(*) For the system hexadecyltrimethylammonium *p*-toluenesulfonate without monovalent counterions, the notation CTAT is prefered to C_{16}TAB/Tos. (a) [51, 52, 58], (b) [54–56, 59–61], (c) [55, 60, 62–74], (d) [68, 71, 75–82], (e) [83, 84], (f) [61], (g) [85–87], (h) [88–95], (i) [57, 96–99], (j) [93]

studies have been performed on systems of the alkyltrimethylammonium bromide class (C_nTAB), using strongly binding counterions or hydrotopes. Well-known examples of hydrotopes are salicylate, *p*-toluenesulfonate, and chlorobenzoate, which all contain an aromatic phenyl group.

In Table 1, for the sake of simplicity, we have given the abbreviations of the surfactants and hydrotopes with their monovalent counterions. Tetradecyltrimethylammonium bromide with sodium salicylate thus becomes in short C_{14}TAB/NaSal. In some cases [51, 52, 59, 60], the small monovalent counterions have been removed by ion exchange procedures, yielding a surfactant salt that is now abbreviated C_{14}TA/Sal [59]. In the following, the abbreviations will take into account these variations. Systems with hydrotopes were generally prepared at equimolar 1:1 conditions. It is interesting to note that, according to Lu et al. [83], only chlorobenzoate isomers with the chlorine in the para-position yields significant shear-thickening and drag reduction, when put in combination with alkytrimethylammonium surfactants (in contrast to the ortho- and meta-isomers). More recently, surfactant systems without hydrotopes were uncovered. The double tail gemini 12-2-12 (ethanediyl-1,2-bis(dodecyl dimethylammonium bromide)) [88–92] and the partially fluorinated surfactant (perfluorooctyl butane trimethylammonium bromide) [93] are among the most surveyed systems of this kind. Concerning the class of gemini surfactants, some molecules with specific architecture were also shown to self-assemble into micelles with more complex topologies, such as ring-like [100] and branched [101] structures. Note finally a system made from oppositely charged surfactants, tetradecyl dimethylamine oxide (C_{14}DMAO) and dodecyl sulfate (SDS), which displays the above properties only for mole fractions [C_{14}DMAO]/([C_{14}DMAO] + [SDS]) between 0.5 and 0.8 [85–87]. In Table 1, again for simplicity, we have omitted commercial surfactants showing a polydispersity of the aliphatic tails, or chemical structures that are less well characterized [102].

2.3 Rheology

The shear-thickening transition in dilute surfactant solutions was investigated using both strain- and stress-controlled rheometry. Due to the low viscosity of the solutions, Couette geometries either with single or double Couette walls were preferred (Fig. 2). Due to the long transients in the kinetics of the SIS formation, the shear stress vs shear rate curves were determined by measuring the time dependence of the stress, and by recording its stationary value. The flow curves were then constructed point by point so as to ensure that they corresponded to the stationary state of flow.

2.3.1 Strain-Controlled Rheometry

Figure 4 displays the general behavior of the shear-thickening transition observed with imposed shear rate. The steady shear stress $\sigma(\dot{\gamma})$ and the steady apparent shear viscosity $\eta(\dot{\gamma})$ are shown as a function of the applied shear rate for the hexadecyltrimethylammonium *p*-toluenesulfonate (CTAT) at $c = 0.41$ wt. %. For this system, the overlap concentration was estimated at $c^* = 0.5$ wt. % and the shear-thickening to be present over the range 0.05–0.8 wt. % [75, 103].

In Fig. 4, three flow regimes can be distinguished:

- *Regime I*. At low shear rates, the stress increases linearly with the rate, indicating a Newtonian behavior.
- *Regime II*. At $\dot{\gamma}_c$, the viscosity increases and deviates progressively from the Newtonian behavior. The transition toward the shear-thickened state is continuous.
- *Regime III*. The apparent viscosity passes through a maximum, at a level that is several times that of the solvent viscosity, and then shear-thinning is observed.

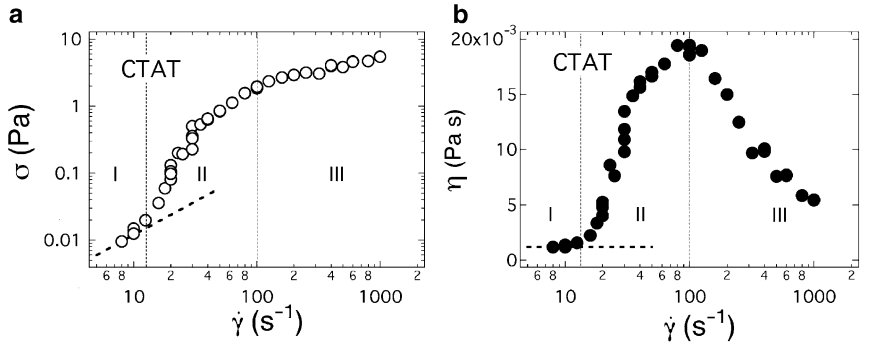

Fig. 4 Steady state shear stress (**a**) and viscosity (**b**) vs shear rate for hexadecyltrimetylammonium *p*-toluenesulfonate (CTAT) at $c = 0.41$ wt. % and $T = 23\,^{\circ}$C. With increasing shear rates, three flow regimes are encountered. At low shear rates (Regime I), the stress increases linearly with the rate with a constant slope η_0, indicating a Newtonian behavior (*dashed lines*). At $\dot{\gamma}_c = 14 \pm 2\ s^{-1}$, the viscosity increases and deviates progressively from the Newtonian behavior. In Regime III, the viscosity passes through a maximum, and shear-thinning is observed. Figure adapted from [75]

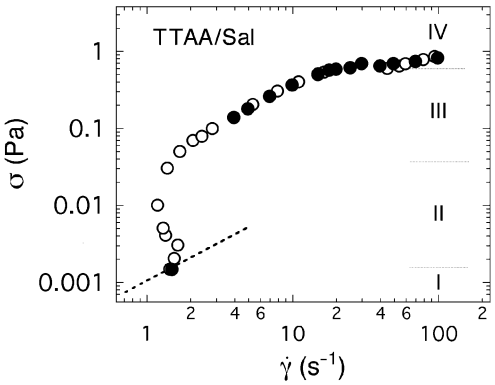

Fig. 5 Steady state rheological behavior of 1.7/1.7 mM *tris*(2-hydroxyethyl)-tallowalkyl-ammoniumacetate/sodium salicylate (TTAA/Sal), corresponding to a total weight concentration $c = 0.10$ wt. %. For this system, four flow regimes were reported, as indicated. Note the re-entrant shear stress vs shear rate curve for the stress-controlled data (*open symbols*), and the discontinuity for the strain-controlled data (*closed symbols*). Figure reprinted with permission from [99]

The three regimes are indicated in the figures by dashed vertical lines. Similar data, and in particular the observation of a continuous viscosity increase in Regime II, were obtained on various systems of Table 1, namely on C_{16}TA/NaSal [62–65, 104] gemini 12-2-12 [88, 89]. Note that, for TTAA/Sal, a discontinuous transition between Regime I and Regime III was reported with controlled strain rates, as illustrated in Fig. 5 and discussed in details below [99].

2.3.2 Stress-Controlled Rheometry

Stress-controlled rheometry has been operated on fewer systems, as compared to strain-controlled rheometry. In C_{16}TAB with salicylate and *p*-toluenesulfonate counterions, Hartmann et al. observed a phenomenology close to that reported in Fig. 4, that is the occurrence of the sequence Newtonian (I) – shear-thickening (II) – shear-thinning (III) [68]. Pine and coworkers were the first to notice the existence of a re-entrant flow curve above the critical shear rate (Fig. 5). These results were obtained on a 1.7/1.7 mM *tris*(2-hydroxyethyl)-tallowalkyl ammonium acetate/sodium salicylate (TTAA/Sal), in which TTAA represents a mixture of C_{16} and C_{18} alkyl chain surfactants [57, 96–99, 105]. The total weight concentration of this sample was $c = 0.10$ wt. %. Careful transient measurements allowed to confirm the existence of stationary flows at shear rate below $\dot{\gamma}_c$ (re-entrant behavior). These findings were interpreted as strong evidence that a more viscous phase was building up under constant stress. With increasing shear stress, the $\sigma(\dot{\gamma})$-flow curve of TTAA/Sal was found similar to that of most compounds, showing a transition toward a shear-thinning at high shear stress. Unlike most rheological characterizations, Pine and coworkers reported four flow regimes, noted I to IV on the figure. There, Regimes I, II, and IV correspond to the three regimes of Fig. 4, whereas Regime III sets the

limits of a range where the viscosity stays constant as a function of $\dot{\gamma}$. Using stress-controlled rheometry, Walker and coworkers also observed a slightly re-entrant behavior above the critical stress in the CTAT dilute solutions [76].

2.3.3 Transient Rheology

As already mentioned, considerable care was taken by experimentalists in order to ensure the actual determination of the steady state. Most procedures used start-up experiments, which consisted of imposing the shear rate (respectively, stress) on freshly poured solutions and measuring the stress (respectively, rate) as a function of time. This approach had already been suggested by the work of Hoffmann and Rehage (see Fig. 3). Start-up experiments have revealed two major results that were later corroborated on most systems:

- In Regimes II and III, the shear-thickening state was reached after an induction time noted $t_{\rm ind}$.
- As noticed by most of the earlier reports, this induction time varied as $1/(\dot{\gamma}-\dot{\gamma}_c)$ [77], or as $1/\dot{\gamma}$ far from the critical conditions [86,87,89,98,106]. In other words, the closer the shear rate was from the critical value, the longer was the time to reach stationary state. This result was interpreted as an indication that the relevant quantity for the induction of the SIS was the total deformation $\dot{\gamma}t_{\rm ind}$ applied. These findings were observed for CP/Sal [51,52], C_{16}TAB/NaSal [63] and TTAA/NaSal [98].

More recently, a closer inspection of the transient stress rheology for thickening systems has revealed more complicated patterns, such as structural memory effects. Berret et al. [78] and Oeschlager et al. [93, 107] have observed that the transient mechanical response also depended on the thermal and shear histories. Samples having been treated thermally, e.g., heated up to 90 °C for 2 h, behaved very differently from samples freshly prepared or already sheared. The induction time could last several hours, and was not proportional to the inverse shear rate, as mentioned previously. It was concluded that the lack of reproducibility under certain thermal and shear conditions might indicate that these surfactant solutions were characterized by long-lived metastable states.

Other transient experiments commonly carried out on these solutions were stop-flow measurements. When sheared in the thickening regime, at the abrupt arrest of the shearing cell, the shear stress was found to relax via a double exponential decay, the shortest time being of the order of 1 s (associated to the reorientation dynamics) [89], and the longest time being of the order of seconds or minutes. Concerning this longer time, values in the range 1–1000, 5–500, and 5–40 s were observed for C_{14}TA/Sal [55], gemini 12-2-12 [89], and CTAT [108] dilute solutions respectively. The above ranges correspond to different conditions of temperature and/or concentration. Because of the monoexponential character of the long-time relaxation, and also because semidilute micellar solutions respond to stop-flow similarly [21], the

vanishing of the stress was ascribed to the relaxation of entangled wormlike micelles. Such a conclusion implicitly assumes that the micelles have grown under shear, although this was not formulated in such terms in the literature. We will come back to this point later.

2.3.4 Concentration and Temperature Dependence

With increasing concentrations, all the reported surfactants exhibit a transition between a dilute and a semidilute regime at c^*. Below c^*, micelles are short and do not overlap, whereas above c^*, chain entanglements slow down considerably the dynamics of the network and the zero-shear viscosity increases sharply [59,61,65,66,75,96,99,103]. The shear-thickening transition has been observed for concentrations below and above the overlap concentration. Shear-thickening in solutions with viscosities up to 1000 times that of water were reported [99]. Concerning the concentration dependence of the critical shear rate $\dot{\gamma}_c$, no universal behavior could be evidenced. $\dot{\gamma}_c$ was found to increase in CTAT (with D_2O as a solvent) [75] and in TTAA/NaSal [99], and to decrease in C_{14}DMAO/SDS [85], in gemini 12-2-12 [89] and in C_{16}TAB/NaSal [67]. In some other systems, it was found to remain concentration independent [75].

Much stronger dependences were observed as a function of the temperature. All systems investigated exhibited an Arrhenius-type behavior for the critical shear rate $\dot{\gamma}_c$, i.e.:

$$\dot{\gamma}_c(T) \sim \exp\left(-\frac{E_a}{k_B T}\right), \tag{1}$$

where E_a is an activation energy, k_B the Boltzmann constant, and T the absolute temperature. Activation energies E_a were found in the range 20–120 $k_B T$ ($T = 300\,K$), or equivalently between 50 and 300 kJ mol^{-1}. Concomitant to the shift of $\dot{\gamma}_c$ to larger values, the amplitude of the shear-thickening effect diminished with increasing temperature [55,62,63,75,89]. Ultimately, above 50 °C, the shear-thickening vanished. The origin of the underlying activated process in shear-thickening systems has not yet been identified.

In addition to concentration and temperature, other parameters capable of modifying the transition have been studied. These were (i) the shearing cell geometry, and in particular the gap of the Couette cell [55,58,62,96,99,104], (ii) the ionic strength [68, 85], and (iii) the addition of polymeric additives, such as PEO (poly(ethylene oxide)) or HPC (hydroxypropyl cellulose) [103]. Among these parameters, the geometry effect is certainly the most intriguing. Already present in the work by Ohlendorf and Wunderlich [55,62], it was noticed that smaller gaps shifted the critical shear rate towards higher values, and reduced the amplitude of the viscosity jumps. The gap effects were later interpreted by Pine and coworkers as a consequence of the slipping of the SIS along the walls, through the presence of a thin lubricating layer (see Fig. 8 for details) [96].

2.4 Structure and Orientation Under Shear

2.4.1 Small-Angle Scattering Under Shear

Thanks to an excellent neutron scattering contrast of hydrogenated surfactants in deuterated water (D_2O), small-angle neutron scattering (SANS) has become a privileged tool for the investigation of dilute shear-thickening solutions. Most of the systems in Table 1 have been investigated by SANS in quiescent conditions [54, 56, 75, 76, 85, 90, 103, 108]. All these studies have revealed a unique behavior: the surfactants self-assemble into cylindrical micelles. The radius of the micelles was also determined, and found to be around 2 nm [54, 56, 75, 76, 85, 90, 103, 108]. The other feature revealed by SANS was the occurrence of a structure factor indicative of strong repulsive interactions between the micellar threads. These interactions were attributed to the electrostatic charges at the surfaces of the rods. Electrostatic structure factors were observed on salt-free solutions of C_{14}DMAO/SDS [85], gemini 12-2-12 [88, 90], and CTAT [75, 79, 108]. During the last two decades, neutron [54, 56, 75, 76, 79, 85, 88, 90, 103, 108] and light [87, 91–93, 106, 107] scattering under shear were performed repeatedly on dilute thickening systems. As early as 1986, Bewersdorff and coworkers set up a Couette cell on a neutron spectrometer in order to detect the anisotropy of the scattering induced by the shearing [54]. In a series of runs performed on C_{14}TA/Sal, it was shown that, under shear, the scattered intensity collected on a two-dimensional detector was highly anisotropic, the scattering being predominantly in the direction perpendicular of the velocity. It was concluded that the shear-induced phase corresponded to a highly aligned state of cylindrical micelles [54]. An illustration of this anisotropy shown in Fig. 6a for

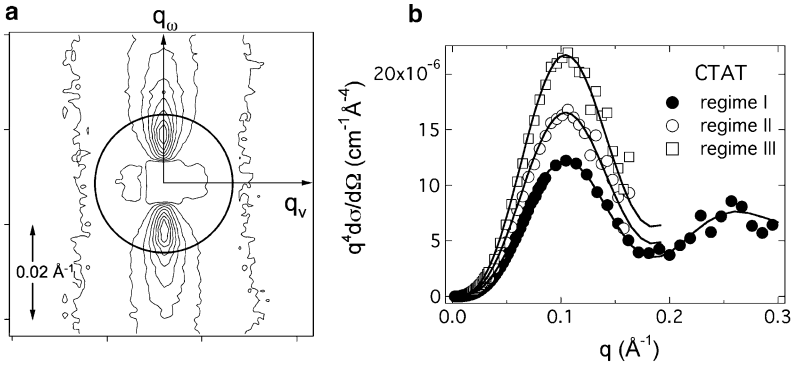

Fig. 6 (**a**) Two-dimensional neutron scattering pattern characteristic of the shear-induced phase in hexadecyltrimethylammonium *p*-toluenesulfonate dilute solutions. The solvent here is D_2O, the concentration $c = 0.26$ wt. %, and the shear rate $\dot{\gamma} = 188\,s^{-1}$ (Regime III in Fig. 4). $\mathbf{q}_v$ and $\mathbf{q}_w$ are, respectively, parallel to the velocity and vorticity directions of the flow. The ring shows the wave-vector at which the scattering cross-section is maximum in the quiescent state. (**b**) Porod representation of the neutron scattering intensities in Regimes I, II, and III (intensity in the vorticity direction). The oscillations in the form factors for the three set of data are in agreement with a morphology of cylindrical micelles with radius $R_c = 1.95$ nm, with a standard deviation of 0.2 nm (*continuous lines*). Figure adapted from [79]

CTAT ($c = 0.26$ wt. %, $\dot{\gamma} = 188\,s^{-1}$ corresponding to Regime III) is representative for this class of materials. An approach in terms of orientation distribution function was performed on the neutron spectra by analogy with the data analysis of nematic phases [109] (see Sect. 4). The order parameter of the micellar orientations was then derived and found to be 0.8. This value is close to unity, which designates a perfect alignment. On the same CTAT specimen, additional information could be gained from the study of the position of the structure factor as functions of surfactant concentration and shear rate. Below c^*, the structure factor peak of the SIS was found to shift to lower wave-vectors by 30% as compared to its value in the Newtonian regime (Fig. 6a). It actually moved down to the semidilute $q^{1/2}$-scaling law that was determined from solutions above c^*. This shift was interpreted as an indication of a shear-induced growth of the micelles, from short rodlike to wormlike aggregates. Similar shifts of the structure factor were observed for the gemini 12-2-12 surfactants [88, 90].

Concerning the shear-thickening transition, the question was raised about a possible transition of morphology, a transition where the original microstructure would be changed into heterogeneous patterns showing stippled or sponge-like textures [105]. It was also suggested by others that the micellar threads would eventually undergo a transition towards a bundle state [110]. Figure 6b shows the scattering intensities in the direction perpendicular to the flow velocity in Regimes I, II (shear-thickening), and III (shear-thinning), again for the CTAT system [79]. There, the Porod representation ($q^4 \times d\sigma(q)/d\Omega$ vs q) has been used in order to emphasize the local morphology at rest and under shear. As a result, all three data sets exhibit oscillations consistent with a cylindrical micelles with radius $R_c = 1.95$ nm. Qualitatively, the fact that the position of the first maximum remains unchanged under shear supports the conclusion that the local morphology remains rodlike. Similar rodlike. Similar results were found in gemini 12-2-12 dilute they were not interpreted using the Porod representation [111].

More recently, on gemini surfactants Weber and Schosseler have investigated the light scattering properties under shear, in order to probe the sheared fluid at length scales larger than those accessible by SANS [91]. For a 18.3 mM solution ($c = 1.0$ wt. %), an intense streak pattern perpendicular to the velocity direction was observed in the shear-thickening regime. The patterns exhibited strong fluctuations in amplitude, as well as a spatial modulation along the vorticity axis. A correlation length of the order of 30 µm was derived from this modulation. It was finally argued that these 30 µm were not compatible with the intermicellar distance, estimated in this solution at a few tens of nm. The light scattering data were interpreted in terms of a strongly aligned and heterogeneous gel-like layers in the gap of the Couette cell.

2.4.2 Flow Birefringence

A remarkable property of the shear-induced phase is its flow birefringence. Flow birefringence experiments on shear-thickening surfactant solutions were introduced

by Hoffmann and coworkers more than two decades ago [55, 59]. Wunderlich et al. have shown, for instance, that, for C_{14}TA/Sal [59], the onset of flow birefringence coincided with the increase of viscosity. Such results were found on all shear-thickening systems studied by this technique. Flow birefringence was measured by transmission using a Couette geometry. With this configuration, the polarized light propagates along the vorticity direction and the transmitted light reads

$$I = \frac{I_0}{2} \sin^2 \frac{\delta}{2} \sin^2(2(\chi - \theta)), \tag{2}$$

where I_0 is the incident light intensity, $\delta = 2\pi h \Delta n/\lambda$ the phase angle, χ the extinction angle, and θ the angle made by the polarization of the incident beam with the flow velocity (in the expression of the phase angle, h is the height of the Couette cell and λ the wavelength of light). The values of the birefringence Δn were found to be negative, lying between -10^{-5} and -10^{-7}, depending on the weight concentration. The flow birefringence was essentially measured at steady state as a function of the shear rate and under various conditions of temperature, concentration, and ionic strength [59, 61, 77, 78, 85, 89, 106].

The two main results of birefringence are illustrated in Fig. 7 for the 3/3 mM C_{14}TAB/NaSal solution ($c = 0.15$ wt. %) [61]. They are:

- An increase of Δn in Regime II, followed by saturation in Regime III.
- An abrupt decrease of the extinction angle at the onset of thickening toward a value close to 0°, both in Regimes II and III.

Figure 7 illustrates that, as soon as the new phase is induced, it is strongly oriented by the flow. In some reports, χ-data shown as a function of the shear rate have revealed that the extinction angle undergoes a discontinuity from $\chi = 45°$ to $\chi \sim 0°$

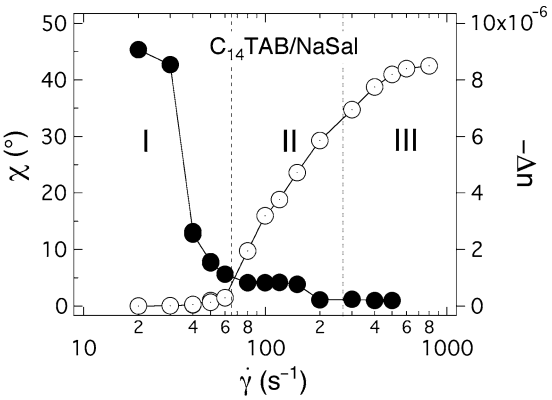

Fig. 7 Shear rate dependences of the flow birefringence Δn (*right scale*, *open symbols*) and of the alignment angle χ (*closed symbols*, *left scale*) for 3/3 mM tetradecyltrimethylammonium bromide and sodium salicylate (C_{14}TAB/NaSal), corresponding to a total weight concentration $c = 0.15$ wt. %. Regimes I, II, and III were determined from steady shear viscosity. Figure adapted from [61], courtesy J.P. Decruppe

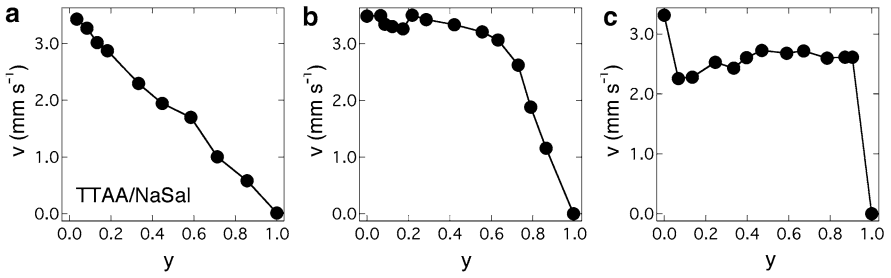

Fig. 8 Time development of the velocity profile in a 4-mm gap Couette cell for a 1.7/1.7 mM TTAA/NaSal solution. The time frames (**a**), (**b**), and (**c**) correspond to 6, 438, and 3,071 s, respectively, after the inception of shear ($\dot{\gamma} = 1\ s^{-1}$). The coordinates are referenced with respect to the inner cylinder (gap position 0) and to the outer cylinder (gap position 1). Figure adapted from [96]

at $\dot{\gamma}_c$ [77]. Recent measurements have confirmed this feature [61]. Time- and space-resolved studies of the flow birefringence were also attempted [77]. In CTAT, these studies have revealed that, once the SIS was initiated, it spread over the whole gap of the cell, and no regime of coexisting states (such as birefringent and nonbirefringent) could be detected.

2.4.3 Particle Image Velocimetry

Flow velocimetry measurements on shear-thickening include works by Koch and coworkers on C_{14}TA/Sal and C_{16}TA/Sal [60] and by Hu et al. on TTAA/NaSal micelles [96], both using particle image velocimetry (PIV). One of the reasons for the few PIV studies lies in the fact that the critical shear rates are high (in general some tens of s^{-1}) and that under such conditions, measurements of flow velocities using seeding particles remain challenging. Figure 8 shows three cartoons of the velocity profiles determined at different times during a start-up experiment. The system placed under scrutiny was TTAA/NaSal at 1.7 mM and at 1:1 ratio between surfactant and aromatic counterions (weight concentration 0.10 wt. %) [96]. The gap of the Couette cell was 4 mm and the inner cylinder (gap position 0) was moving. After the inception of shear (Fig. 8a), the linear velocity profile for a homogeneous shear flow was observed. As the SIS began to grow from the inner wall (Fig. 8b), a progressively thicker region of uniform velocity developed, with a steeper velocity gradient near the outer cylinder. For long times (Fig. 8c) the velocity field remained uniform over most of the gap, with two thin and fast layers near the walls. Hu and coworkers concluded that, at steady state, the SIS fills most of the center of the gap and behaves as a "solid" body in rotation (plug flow) [96]. Although less documented than Hu et al.'s paper, the data from Koch et al. displayed typically the same effect, namely that the shear-induced structure was associated with a highly nonhomogeneous flow, with slippage at the walls [60]. Convincing evidence of wall slip was also reported by Sung et al. [58] in CPCl/NaSal solutions from direct rheological measurements.

2.5 Conclusion

In the preceding sections, we have shown that the surfactants listed in Table 1 share identical properties when submitted to shear: above a critical shear rate, a structure that is more viscous than the suspending solvent is induced, yielding an increase in the apparent viscosity of the fluid. In the following, we recapitulate the milestones that are important in the present experimental context, and suggest a minimal scenario for the transition.

1. *The local micellar structure does not change under shear*
   By restricting ourselves to the dilute case, it can be concluded that the rodlike micelles are unentangled at rest and in the Newtonian domain. There, the viscosity is close to, or a few times, that of water. Small-angle neutron scattering shows conclusive evidence that the cylindrical structure of the rods is preserved at all shear rates. The hypothesis suggested in the past, according to which the shear-thickening could originate from a modification of the local structure of the surfactant assemblies, can reasonably be ruled out [105, 110].
2. *Shear-thickening is associated with micellar growth*
   The structural modifications of the aggregates occur in contrast at a larger scale, namely at the scale of their length. Using light and neutron scattering, it was demonstrated that the shear-thickening transition is accompanied by a uniaxial growth of the micelles, which hence undergo a transition from rodlike to wormlike aggregates [79, 87, 90].
3. *The shear-induced structure is viscoelastic*
   The second indication of the wormlike micellar character of the SIS is its viscoelasticity. The viscoelasticity of the shear-induced phase was observed in stop flow experiments in a series of systems [52, 55, 59, 78, 85, 89, 108]. According to the definition of viscoelasticity [112], the long time seen in these experiments can be ascribed to the intrinsic relaxation of the shear-induced state. With this in mind, the Weissenberg number (the product of the shear rate and relaxation time) for these micellar fluids can be estimated. In Regimes II and III, the Weissenberg numbers reach values lying between 10 (at $\dot{\gamma}_c$) and 1000. Depending on the system, this range can go even higher, as in gemini 12-2-12 [89] or CTAT [108]. Hence, once the micelles have grown in size, they are directly brought to a state that is strongly sheared on the time scale of the fluid. At high Weissenberg numbers, the sheared solutions could undergo elastic instabilities, that could then generate more complex flows such as flows along the vorticity direction [113]. Three-dimensional flows associated with the shear-thickening in dilute regime have not been reported so far.

In Fig. 9, a schematic diagram accounts for a possible scenario of the shear-thickening transition. There, curve A denotes the apparent viscosity of a dilute surfactant solution containing nonoverlapping rodlike micelles (Newtonian), whereas curve B corresponds to the flow curve of the same solution, but for which the micelles are long and entangled (shear-thinning). At the transition rate, the fluid jumps from branch A to branch B. With decreasing shear rate, starting from the induced phase, the SIS vanishes reversibly as the micelles disassemble into short rodlike

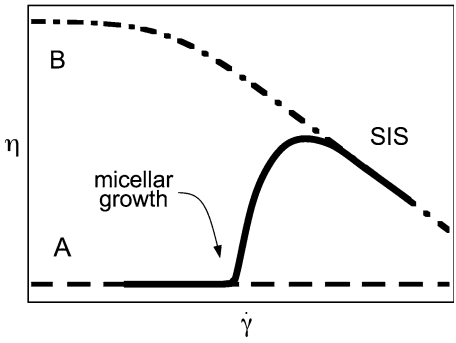

Fig. 9 Schematic diagram accounting for the shear-thickening transition in dilute surfactant solutions

aggregates. From this minimal scenario, it can be understood that the micelles are strongly aligned in the flow, or that the flow becomes nonhomogeneous [60, 96, 99] or turbulent in the shear-thinning regime [96, 98]. The hydrodynamic instabilities of dilute wormlike micelles and in turbulent flows remain one of the most promising issues of this field.

Concerning the mechanism of growth induced by shear, many theories and models were developed during the last three decades, and none of them were fully satisfactory. Most models were based on the assumption that the increase of viscosity was related to a shear-induced "gelation." Many phenomenological models were constructed assuming a banded state of coexisting gel and fluid phases [114, 115]. Some microscopic theoretical attempts had anticipated that "gelation" could be connected to a shear-induced micellar growth [116–118]. Concerning these earlier models, however, the predicted critical shear rates were too large as compared to the experimental values [108]. It is out of the scope of the present review to survey the theoretical treatments of the shear-thickening transition. We rather refer to recent and exhaustive reviews by Cates and Fielding [119] and by Olmsted [120].

The structural memory effects found in different systems (such as CTAT, gemini 12-2-12 and in the fluorocarbon surfactant C_8F_{17}), and discussed in the transient rheology section, suggest that the aggregation in the quiescent state and the thickening transition are interrelated. It is certainly not easy to conceive that dilute and very dilute solutions could exhibit exotic behaviors, in particular in reference to the self-assembly mechanism. One possible explanation would be that the surfactant solutions are in a metastable self-assembled state, due, for instance, to the long range electrostatic interactions. This metastable state could then be described as a coexistence state of of short rodlike aggregates and slowly evolving supramolecular structures, such as huge micelles or pieces of entangled network. This additional and unexpected populations of large micelles have been recently observed in two systems, again the gemini 12-2-12 studied by Schosseler and coworkers and in the fluorcarbon surfactant by Oehlschager et al. [93]. Light scattering performed on quiescent solutions have shown the coexistence of short, intermediate, and very large micelles, which respective populations varied with the thermal and shear histories. It remains now to demonstrate that these large structures are playing the role of initiators for the shear-thickening transition, as well as to understand the metastability of the different self-assemblies.

3 Shear Banding Transition in Semidilute and Concentrated Giant Micelles

3.1 Introduction

This part is devoted to the nonlinear rheology of semidilute and concentrated giant micelles systems. In the semidilute regime, characterized by concentrations ranging typically from 0.1 to $\simeq$10 wt. %, wormlike micelles form a viscoelastic network and, are supposed, by analogy with polymers, to follow simple scaling laws [25, 40]. In the concentrated regime, corresponding typically to weight concentrations between $\simeq$10 wt. % and c_{I-N}, the isotropic-to-nematic phase boundary, the mesh size of the entangled micellar network becomes of the order of or shorter than the persistence length (see Fig. 1).

When submitted to simple shear flow, giant semidilute and concentrated micelles show original nonlinear responses. A number of experimental publications suggest that micellar solutions undergo a shear-banding transition. This transition, due to the coupling between the internal structure of the fluid and the flow, is usually associated with a new mesoscopic organization of the system. In turn, the modification of the supramolecular architecture of the fluid affects the flow itself and generates shear localization effects generally characterized by a splitting of the system into two macroscopic layers bearing different shear rates and stacked along the velocity gradient direction.

This transition from a homogeneous towards a nonhomogeneous flow has been reported in complex fluids of various microstructure such as lyotropic micellar and lamellar phases [44, 121, 122], triblock copolymers solutions [123, 124], viral suspensions [125], thermotropic liquid crystal polymers [126], electro-rheological fluids [127], soft glassy materials [128], granular materials [129, 130], or foams [131–133].

Among these systems, the shear banding flow of reversible wormlike micelles is particularly well documented [44]. The rheological signature of this type of flow has been observed for the first time in the pioneering work of Rehage et al. [28]: the measured flow curve $\sigma(\dot{\gamma})$ is composed of two stable branches respectively of high and low viscosities separated by a stress plateau at $\sigma = \sigma_p$ extending between two critical shear rates $\dot{\gamma}_1$ and $\dot{\gamma}_2$ (see Fig. 10a). When the imposed shear rate $\dot{\gamma}$ is lower than $\dot{\gamma}_1$, the state of the system is described by the high viscosity branch which is generally shear-thinning: the micellar threads are slightly oriented with respect to the flow direction and the flow is homogeneous. For macroscopic shear rates above $\dot{\gamma}_1$, the flow becomes unstable and evolves towards a banded state where the viscous and fluid phases coexist at constant stress σ_p (see Fig. 10b). The modification of the control parameter is only supposed to affect the relative proportions f and $1-f$ of each band according to a simple lever rule that results from the continuity of the velocity at the interface:

$$\dot{\gamma} = f\dot{\gamma}_1 + (1-f)\dot{\gamma}_2. \tag{3}$$

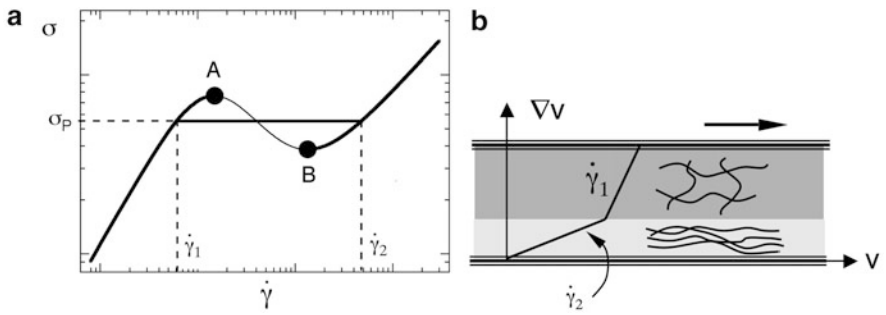

Fig. 10 (**a**) Nonmonotonic constitutive relation for giant micelles composed of two stable branches separated by an unstable region AB. The corresponding steady-state flow curve presents a stress plateau at $\sigma = \sigma_p$, extending between two critical shear rates $\dot{\gamma}_1$ and $\dot{\gamma}_2$, and associated with the shear-banding transition. (**b**) Scheme of the shear-banding scenario in giant micelles systems

Above $\dot{\gamma}_2$, the system is entirely converted into the fluid phase: the induced structures are strongly aligned along the flow direction and the homogeneity of the flow is recovered. This scenario, due to the existence of a nonmonotonic relation between the shear stress and the shear rate as schematized in Fig. 10, was predicted by Cates and coworkers more than 15 years ago [134]. Since then, it has been the subject of intense experimental and theoretical studies. From an experimental point of view, shear banding has been identified unambiguously in wormlike micelles using various techniques probing either the local flow field or the structure of the system.

In the following, we review the phenomenology of shear banding flow in semidilute and concentrated wormlike micelles. This part is organized as follows. In Sect. 3.2, we describe the mechanical signature of the shear-banding transition. Section 3.3 is devoted to the characterization of the local flow field, while in Sect. 3.4, we focus on the structural properties of the banded state.

3.2 Nonlinear Rheology

3.2.1 Steady-State Rheology

Standard Behavior

In order to illustrate the typical nonlinear mechanical response of wormlike micelles under steady shear flow, we chose to focus on the cetylpyridinium (CPCl)/sodium salicylate (NaSal) system. It is often considered as a model system since it follows the right scaling laws for the concentration dependence of the static viscosity and plateau modulus [32]. Moreover, for concentrations ranging from 1 to 30 wt. %, the samples behave, in the linear regime, as almost perfect Maxwellian elements with a single relaxation time τ_R and a plateau modulus G_0. This system has been

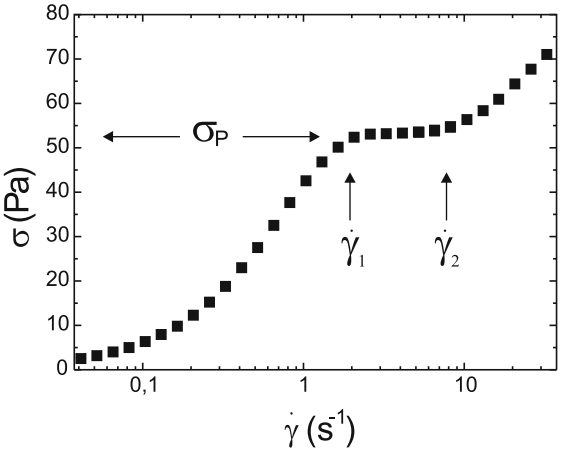

Fig. 11 Experimental steady-state flow curve of a semidilute binary mixture made of cetylpyridinium chloride/sodium salicylate diluted in 0.5 M NaCl brine at a temperature of 25 °C. The total weight fraction is 6.3 wt. % and the molar ratio R =[Sal]/[CPCl]= 0.5. The shear stress is measured under strain-controlled conditions in a cone and plate geometry

extensively studied during the last two decades [28,33,135–141] and the description of its mechanical behavior is certainly one of the most complete.

Figure 11 displays, on a semilogarithmic plot, the evolution of the shear stress σ as a function of the shear rate $\dot{\gamma}$ for a sample at a total weight fraction $c = 6.3$ wt. % obtained under strain-controlled conditions in a cone and plate geometry [33]. This flow curve is made up of two increasing branches separated by a stress plateau extending between two critical shear rates $\dot{\gamma}_1$ and $\dot{\gamma}_2$. The high viscosity branch is Newtonian at very low shear rates and becomes shear-thinning when approaching the first threshold $\dot{\gamma}_1$, whereas the low viscosity branch above the second critical shear rate $\dot{\gamma}_2$ is usually purely shear-thinning, indicating that the constitutive behavior of the induced structures is non-Newtonian. At the critical shear rate $\dot{\gamma}_1$, the shear stress reaches a value $\sigma = \sigma_p$ and the flow curve exhibits a strong change of slope followed by a stress plateau that can extend over several decades in shear rates, depending on the composition of the sample. In some cases, the stress plateau presents a significant slope and is generally well fitted by a power-law $\sigma \sim \dot{\gamma}^{\alpha}$ with exponent α between 0.1 and 0.3. This shear rate dependence is usually explained by the coupling between flow and concentration fluctuations [142, 143].

Various shear histories have been applied in order to test the robustness of the stress plateau. The latter has been found to be unique and history independent. This reproducibility is a crucial feature of the nonlinear rheology of wormlike micellar systems [33, 138, 140, 144].

The mechanical behavior described above concerns most semidilute wormlike micelles. The situation for concentrated samples is analogous with minor changes: the low shear rate branch is purely Newtonian and the transition towards the stress plateau is more abrupt [137].

Table 2 Systems of wormlike micelles known to exhibit a stress plateau in their steady flow curve

Surfactant	Additive	Salt	Conc. regime	Experiment	References
CPCl	NaSal		sd	NMR, FB, PIV, SANS, SALS	(a)
CPCl	NaSal	NaCl	sd/c	NMR, FB, DLS, PTV, PIV, USV, FI	(b)
C_{16}TAB			c	NMR, FB, USV, SANS	(c)
$CPClO_3$		$NaClO_3$	c	SANS	(d)
C_{16}TAB	NaSal		sd	FB, USV, SANS, LSI, SALS	(e)
C_{16}TAB		KBr	sd/c	FB	(f)
C_{16}TAB		$NaNO_3$	sd/c	FB, LSI, SALS	(g)
CPCl	Hex	NaCl	c	SANS, FB	(h)
CTAT			sd/c	...	(i)
CTAT		NaCl	sd	...	(j)
C_{16}TAC	NaSal		sd/c	FB	(k)
C_{12}TAB	NaSal		sd	...	(l)
SDS		$Al(NO_3)_3$	sd	...	(m)
EHAC		NH_4Cl	sd	...	(n)
EHAC		NaCl	sd	FB, SANS, SALS	(o)
EHAC	NaSal		sd	FB, SANS, SALS	(p)
CTAHNC			sd	...	(q)
CTAT	SDBS		sd	FB, SANS	(r)
SDES		$AlCl_3$	sd	...	(s)
SDS	LAPB	NaCl	sd	...	(t)
CTAVB			sd	...	(u)

Column 5 lists the experimental techniques that were used to study shear-banding. The abbreviations are "sd" for semidilute and "c" for concentrated. The letters in the last column denote sets of references detailed below. (a) [28, 135, 136, 140, 141, 145–154], (b) [33, 137–139, 150, 151, 155–165], (c) [166–172], (d) [173], (e) [23, 30, 72, 154, 174–187], (f) [30, 188–191], (g) [144, 165, 192–196], (h) [197–199], (i) [80, 200–205], (j) [200, 206, 207], (k) [208–211], (l) [212], (m) [213], (n) [49], (o) [214], (p) [214, 215], (q) [95, 216], (r) [217, 218], (s) [219], (t) [220], (u) [221]

Hence, the stress plateau in the flow curve $\sigma(\dot{\gamma})$ is the central feature of the nonlinear rheology semidilute and concentrated giant micelles systems and appears as the mechanical signature of the shear-banding transition. The first experimental evidence for such a behavior is due to Rehage and Hoffmann [28] on the semidilute CPCl (100 mM)/NaSal (60 mM) ($c = 4.5$ wt. %) solution. From that time, the stress plateau in wormlike micelles has generated an abundant literature. It is now reported, using various flow geometries such as cylindrical Couette, cone and plate, plate and plate or vane-bob and capillary rheometer, in many other surfactant systems with or without additive and/or salt as illustrated in Table 2.

If normalized shear stress σ/G_0 and shear rate $\dot{\gamma}\tau_R$ are introduced, it is possible to summarize the overall nonlinear rheological behavior measured at different concentrations and temperatures on a master dynamic phase diagram as shown in Fig. 12 [137]. The flow curve at 21 wt. %, a concentration close to the I–N transition, makes the link with the concentrated regime. As concentration decreases, stress

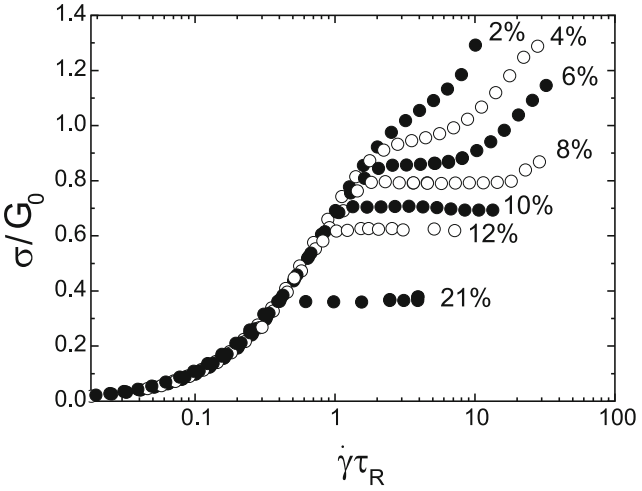

Fig. 12 Generalized "flow phase diagram" obtained for CPCl/NaSal system derived from a superimposition between flow curves at different concentrations and temperatures, using normalized coordinates σ/G_0 and $\dot{\gamma}\tau_R$. No stress plateau is observed beyond the critical conditions $\sigma_p/G_0 > 0.9$ and $\dot{\gamma}\tau_R \simeq 3 \pm 0.5$. From Berret et al. [137]

plateaus are still observed, but the normalized stress and shear rate at which the discontinuity occurs are shifted to larger values. At 6 wt. % and below, the transition between the high viscosity branch and the stress plateau becomes much smoother and the shear stress levels off without discontinuity. Beyond the following critical conditions $\sigma_p/G_0 > 0.9$ and $\dot{\gamma}\tau_R \simeq 3 \pm 0.5$, the stress plateau is replaced by an inflexion point. In other words, the above critical conditions suggest that, by choosing the concentration, temperature or salt content adequately, it is possible to find a stress plateau comprised between $\sigma_p/G_0 \simeq 0$ and 0.9, and of onset $\dot{\gamma}\tau_R$ between 0 and 3. A striking point in Fig. 12 is that the set of normalized flow curves is strongly reminiscent of the phase diagram of a system undergoing an equilibrium phase transition.

All the data presented and discussed until now have been gathered with the shear rate as control parameter. However, numerous studies dealing with the effect of an imposed shear stress have been performed both on semidilute and concentrated wormlike micellar systems [30, 140, 166, 188, 192, 208, 215, 217, 219, 222]. Steady-state flow curves obtained in stress-controlled mode have been found to coincide with flow curves measured under strain-controlled conditions. However, there is a major difference for systems with flat plateaus: it is not possible to reach a stationary coexistence state at imposed stress, since the system directly switches from the low to the high shear rate branch.

Finally, it is also important to emphasize that the nonlinear rheology of viscoelastic surfactant solutions is characterized by the existence of normal stresses of nonnegligible magnitude. In steady-state flow, a nonzero first normal stress difference N_1 has been detected once the first stable branch becomes shear-thinning. N_1 was found to increase with $\dot{\gamma}$ and a slight change of slope was observed at the

onset of the banding regime ($\dot{\gamma} > \dot{\gamma}_1$) [28, 149, 161, 220]. Normal stresses in shear-banded flows are much less documented than their shear counterpart. However, they are well-known to drive elastic instabilities for sufficiently high shear rates [113]. Their role is probably essential to explain some fluctuating behaviors observed in shear-banded flows of wormlike micelles [223–225].

The steady-state mechanical behavior described in this paragraph is representative for entangled wormlike micelles solutions. In the semidilute concentration range, however, a few exceptions to this standard behavior have been reported, as briefly discussed below.

Nonstandard Behaviors

In this paragraph, we mention some marginal rheological behaviors encountered in semidilute wormlike micelles. This list is not exhaustive but allows the illustration of the rheological diversity in these systems.

If the stress plateau is the most encountered feature in the rheology of giant micelles, it is also possible to find solutions for which the Newtonian branch is followed by shear-thinning where the flexible chains simply align along the flow direction as in the case of classical polymer solutions. Such a phenomenology has been reported for samples with low or high concentrations of strongly binding counterions [28, 149, 211].

Another system showing a nonstandard behavior is the equimolar solution made of cetylpyridinium chloride and sodium salicylate, the concentration of each component being fixed at 40 mM. This corresponds to a total weight fraction of 2.1 wt. %. This peculiar system has been extensively studied, especially by Fischer's group during the last few years [169, 222, 226–229] and more recently by Marin-Santibanez et al. [230]. Its nonlinear rheology has been investigated in various flow geometries: at very low shear rates, the solution is Newtonian and then shear-thins, the stress smoothly reaching a pseudo-plateau but without evidence of shear-banding. This regime is followed by a pronounced shear-thickening behavior above a reduced shear rate $\dot{\gamma}\tau_R \simeq 3$ associated with vorticity banding and complex dynamics. We will come back on that point in the section dedicated to time-dependent evolutions.

At the lowest concentrations in the class of semidilute systems, typically ranging from 0.1 to 1 wt. %, a simple shear flow can lead to strong thickening above a critical stress [57, 96, 98, 99]. This is the case of the TTAA/NaSal solutions, already discussed in the part devoted to the shear-thickening transition (Sect. 2). The overall rheological behavior of such systems resembles in some respect that of the equimolar CPCl/NaSal 40 mM solution just evoked above. At concentrations around 10 mM, the micellar network is entangled and the static viscosity is larger than that of the solvent by a factor of 10–1000. As the shear rate is increased, there is first shear-thinning and an abrupt shear-thickening at the critical stress. In addition, concomitantly with the shear-thickening transition, shear-induced structures grow from the inner cylinder, as in the shear-banding transition.

Finally, Hoffmann and coworkers [231] have investigated a binary mixture of hexadecyloctyldimethylammonium bromide (C_{18}–C_8DAB) in water at a concentration of 2.3 wt. %. The flow curve of this solution does not present a stress plateau. However, using small angle neutron scattering experiments under simple shear flow, the authors argued that this system undergoes an isotropic-to-hexagonal transition, where cylindrical micelles of different lengths coexist. The short ones contribute to the isotropic phase, while the long ones ensure the long range hexagonal order. This flow-induced transition presents strong similarities with the I/N transition under shear in concentrated wormlike micelles but without the mechanical signature described in Sect. 3.2.1

3.2.2 Time-Dependent Rheology

During the past decade, many authors have paid close attention to the evolution of the shear stress as a function of time in systems exhibiting a stress plateau. The aim was to identify the mechanisms responsible for the shear-banding transition. In most cases, shear stress time series in response to steady shear rate consists of a slow transient (compared to the relaxation time of the system) before reaching steady state. Nonetheless, more complex fluctuating behaviors such as erratic oscillations suggestive of chaos or periodic sustained oscillations of large amplitude have been observed in peculiar systems.

Standard Transient Behavior

The time-dependent mechanical response is collected from start-up of flow experiments: at $t = 0$, a step-like shear rate is suddenly applied to the sample at rest and the evolution of the shear stress as a function of time is recorded until steady-state is achieved. For imposed shear rates below $\dot{\gamma}_1$ and belonging to the Newtonian part of the high viscosity branch, the shear stress follows a monoexponential growth towards steady-state, with a characteristic time corresponding to the Maxwell time of the system [28, 138]. When the applied shear rate lies in the shear-thinning region of the high viscosity branch, the stress response shows an overshoot at short time before reaching steady-state, a feature classically observed in concentrated solutions of entangled polymers [232, 233].

The start-up curves for various imposed shear rates in the plateau region are displayed in Fig. 13. For all investigated shear rates, the shear stress exhibits an overshoot at short times, the amplitude (σ_{os}) of which increases significantly with $\dot{\gamma}$, followed by a slow relaxation towards a stationary value σ_{st}. This relaxation process comprises a latency period during which the stress remains practically constant at a value $\sigma = \sigma_M$ and then, a decay of sigmoidal shape whose time scale greatly exceeds the terminal relaxation time of the solution (Fig. 13a). The characteristic time τ_N of this slow relaxation diminishes with $\dot{\gamma}$ while σ_M increases (Fig. 13b). When the mean

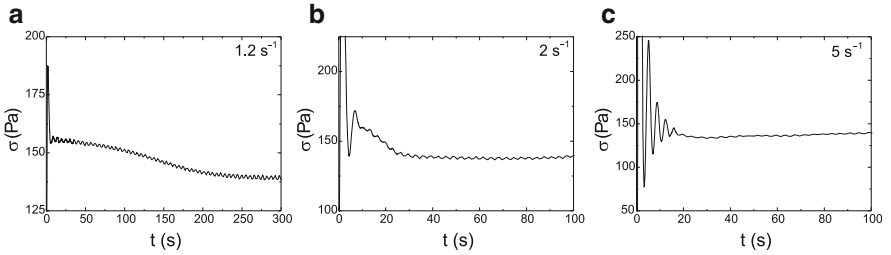

Fig. 13 Transient shear stress recorded after different step shear rates (**a**) $\dot{\gamma} = 1.2\ \mathrm{s}^{-1}$, (**b**) $2\ \mathrm{s}^{-1}$, and (**c**) $5\ \mathrm{s}^{-1}$ for a semidilute sample of CPCl/NaSal (12 wt. %) in 0.5 M NaCl brine at a temperature of $T = 20.3\,^{\circ}\mathrm{C}$. All the applied shear rates belong to the plateau region. Reprinted from Berret [138]

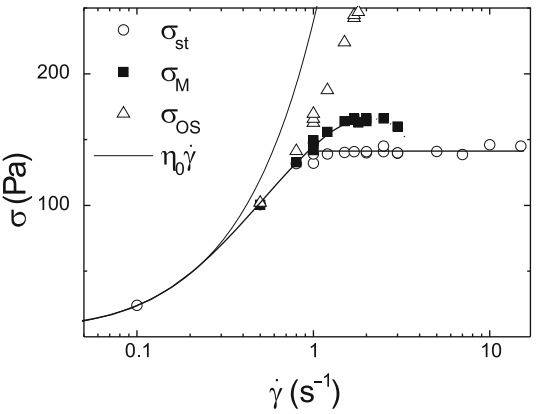

Fig. 14 Stress overshoot σ_{os}, initial shear stress before the onset of the long-time sigmoidal relaxation σ_M and steady-state shear stress σ_{st} gathered from start-up of flow experiments on the semidilute sample of CPCl/NaSal (12 wt. %) in 0.5 M NaCl brine. The purely Newtonian behavior ($\eta_0\dot{\gamma}$) has been added for comparison. Reprinted from Berret [138]

shear rate is incremented, $\sigma(t)$ shows oscillations at short times that precede the long sigmoidal decay. The variations of σ_{os}, σ_{st}, and σ_M with the mean shear rate are given in Fig. 14. The $\sigma_M(\dot{\gamma})$ curve provides evidence for the existence of a metastable branch in which the system is trapped on time scales much longer than the relaxation time τ_R. At higher strain rates, the stress response is dominated by damped oscillations (Fig. 13c). The period of the oscillations has been found to decrease with $\dot{\gamma}$ but, in contrast to nematic wormlike micelles, it does not scale with the inverse shear rate (see Sect. 4). For concentrated samples, a purely monoexponential decay has been observed [199]. Note that such transients are often prolonged by a small undershoot before the steady-state is achieved [33, 140, 144, 157, 191, 194–196].

This type of time-dependent behavior has been observed in various semidilute [23, 33, 138, 140, 144, 150, 157, 161, 174, 177, 180, 191, 195, 196, 203, 220] and

concentrated systems [33, 171, 172, 199]. The sigmoidal decay has been modeled by a stretched exponential of the form [33, 138, 199]:

$$\sigma(t) = \sigma_{st} + (\sigma_M - \sigma_{st}) \exp\left[-\left(\frac{t}{\tau_N}\right)^{\alpha}\right] \tag{4}$$

Depending on the system and on the applied shear rate, α has been found to vary between 1 and 4 [33, 138, 140, 144, 191, 199]. Such kinetics suggests metastability reminiscent of equilibrium first-order phase transitions and has been originally interpreted by Berret and coworkers [33,138] in terms of nucleation and one-dimensional growth of a fluid phase containing highly ordered entities. Other mechanisms involving the slow drift of a sharp interface to a fixed position in the gap of the cell have also been advanced to explain this slow kinetics [190, 234, 235].

Up to now, we have described the time-dependent behavior of the shear stress as a transient towards a steady-state value σ_{st}. However, the notion of steady-state shear stress has to be made clear. Strictly speaking, at long times, $\sigma(t)$ is not rigorously stationary since it presents fluctuations around an average value defined as σ_{st}. The relative amplitude of the fluctuations never exceeds 1% in most of cases. However, some authors have reported fluctuations of stronger amplitude (typically between 5% and 25% of the steady-state signal), revealing complex stress dynamics [80, 159, 169] that we address in the following paragraphs.

Rheochaos

Bandyopadhyay et al. focused on the time-dependent behavior of semidilute solutions of hexadecyltrimethylammonium *p*-toluenesulfonate (CTAT) at weight fractions around 2 wt. % in water, with and without addition of sodium chloride (NaCl). This system is well known to exhibit stress plateau or pseudo-plateau in the flow curve for concentrations ranging between 1.3 and 20 wt. % [80, 203, 206, 207, 236].

Typical time sequences observed in this system are illustrated in Fig. 15. In this data set, the shear rate is kept fixed and the shear stress is recorded as a function of time with the temperature as the control parameter. From the highest temperatures, the stress temporal patterns appear successively periodic and then quasi-periodic with two dominant frequencies (Fig. 15b, c). At lower temperature, the time series still present quasi-periodicity but disrupted by chaotic bursts, typical of intermittency (Fig. 15d). If the temperature is further decreased, the signal becomes finally chaotic (Fig. 15e). The existence of deterministic low-dimensional chaos generating erratic fluctuations in the time series is proved by positive Lyapunov exponent [237] and fractal correlation dimension greater than 2. The route to rheochaos is via type-II temporal intermittency with a Hopf bifurcation [207]. Similar time sequences for the shear rate have been gathered by decreasing the temperature at fixed stress. In that case, the route to rheochaos was found to be of type-III intermittency with period doubling bifurcation [207].

The route to rheochaos can thus be tuned by varying the temperature and consequently the mean micellar length at fixed stress or shear rate [207]. These results

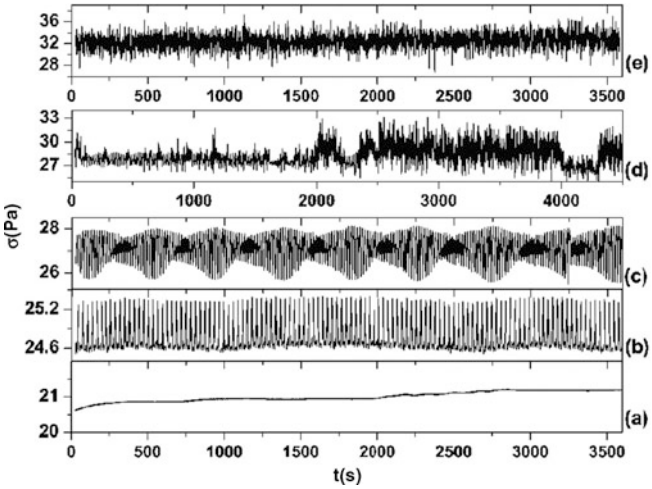

Fig. 15 Stress time series recorded after start-up of flow experiment at a fixed shear rate $\dot{\gamma} = 25\,s^{-1}$ for different temperatures (**a**) $T = 31.5\,°C$, (**b**) $T = 28.8\,°C$, (**c**) $T = 27.2\,°C$, (**d**) $T = 26.5\,°C$, (**e**) $T = 26\,°C$. The sample under scrutiny is made of hexadecyltrimethylammonium *p*-toluenesulfonate (CTAT) at 2 wt. % mixed with 100 mM NaCl in water. The time sequences are found to be (**a**) time-independent, (**b**) periodic, (**c**) quasi-periodic, (**d**) intermittent and (**e**) chaotic. Reprinted with permission from R. Ganapathy and A.K. Sood [207]

agree with recent theoretical predictions due to Fielding et al. [238] using the Diffusive Johnson Segalman (DJS) model and adding a coupling of the flow variables with the mean micellar length. Coupling between flow and concentration fluctuations is also supposed to play a major role in the observed complex dynamics [200, 236].

The same type of irregular time variations of the shear stress (respectively shear rate) at imposed shear rate (respectively shear stress) have been reported for a given temperature. In both cases, the sequence of Fig. 15 has been reproduced by increasing the control parameter [80, 203, 206].

Note that rheochaos has also been observed in solutions of mixed anionic-zwitterionic surfactants [220] and in other systems including shear-thickening wormlike micelles [239], lamellar, onion, and sponge surfactant phases [156, 240–243] and dense colloidal suspensions [244].

Case of the Vorticity Banding

In Sect. 3.2.1, we made reference to a complex constitutive behavior for an equimolar solution of CPCl/NaSal experiencing a shear-thinning to shear-thickening transition. The dynamics of this system has been extensively studied both in strain- and stress-controlled modes. Huge sustained oscillations of the measured quantities (shear and normal stresses or shear rate) as a function of time have been observed in

the shear-thickening regime [169, 227]. The authors showed that these oscillations are correlated with the existence of a banding pattern organized along the vorticity direction and exhibiting a complex dynamics (see Sect. 3.4.2). Note that, unlike the classical shear-thickening transition encountered in dilute surfactant systems and discussed previously, there is no induction time for the shear-induced structures to grow.

Similar stress dynamics has been observed in a semidilute solution of C_{16}TAB (50 mM) and NaSal (100 mM) ($c = 3.4$ wt. %) that also exhibits apparent shear-thickening [183]. However, for this system, the phenomenology is different insofar as the shear-thinning region preceding the apparent thickening transition is characterized by a stress plateau and gradient shear-banding. Besides, Decruppe et al. did not observe vorticity structuring in that case, the flow remaining homogeneous [187].

3.3 Structure of the Flow Field: Velocimetry

To elucidate the shear-banding scenario in wormlike micelles, different velocimetry techniques with high spatial resolution, typically between 10 and 50 µm, such as nuclear magnetic resonance (NMR) velocimetry, particle image velocimetry (PIV), particle tracking velocimetry (PTV), photon correlation spectroscopy (DLS), and ultrasonic velocimetry (USV) have been developed. All provide the velocity component along the flow direction taken from a one-dimensional slice across the gap. For details on these techniques, the reader is invited to refer to [245, 246].

3.3.1 Long-Time Response: Time-Averaged Velocity Profiles

Semidilute Systems

The early velocimetry studies of shear-banding flow in wormlike micellar systems have been performed by Callaghan's group using NMR imaging of the semidilute CPCl (100 mM)/NaSal (60 mM) ($c = 4.5$ wt. %) solution in different flow geometries [135, 145–148, 150]. The method is based on a combination of magnetic field gradient pulses and resonant radio-frequency pulses to encode the NMR signal both from the nuclear spin position as well as translational displacement. The typical spatial resolution is 30 µm. The acquisition times typically vary from 30 min to 4 h, the observed banding structures resulting from long time averages. In addition, the use of a specific encoding method allows the determination of pointwise velocity distribution [246].

In millimetric pipe flow, the increase of the flow rate from the Newtonian to the plateau regime was characterized by a transition from a nearly parabolic Poiseuille profile to an almost flat velocity profile with high shear bands near the tube walls, clearly distinguishable from slip [135]. The thickness of this high shear rate band

was found to grow with the apparent shear rate [139]. Broadening of the velocity distribution revealed fluctuations of the flow field on time scales larger than the encoding time (50 ms) and shorter than the total duration of the experiment [139,146]. Similar velocity profiles were also obtained from PIV measurements in capillary flow [152]. From this local description, the authors were able to reconstruct a complete macroscopic flow curve, consistent with that gathered from bulk rheology. Note that, for the PIV technique, a radial laser sheet illuminates a cross section of the sample in a plane $(\mathbf{v}, \nabla v)$. Images are taken from 90° to the laser sheet and velocity profiles are extracted from spatial correlation between pairs of images.

In cone-and-plate geometry, where the stress distribution is homogeneous in the small gap approximation, Britton et al. showed that the flow field along the plateau region was organized in three bands as displayed in Fig. 16 [150]. The gray scale images clearly show the presence of a central high shear band flanked by two adjacent low shear regions for all applied shear rates. Shear rate profiles computed along the white line point out the mid-gap position of the high shear band. As the mean applied shear rate is incremented, the high shear band expands in width at a constant maximum shear rate around $60\,\mathrm{s}^{-1}$. This value is not consistent with the critical shear rate $\dot{\gamma}_2 \simeq 100\,\mathrm{s}^{-1}$ at the upper limit of the stress plateau. This discrepancy has been ascribed to local fluctuations of the flow field. Velocity fluctuations of different time constants have been observed, depending on sample composition [139].

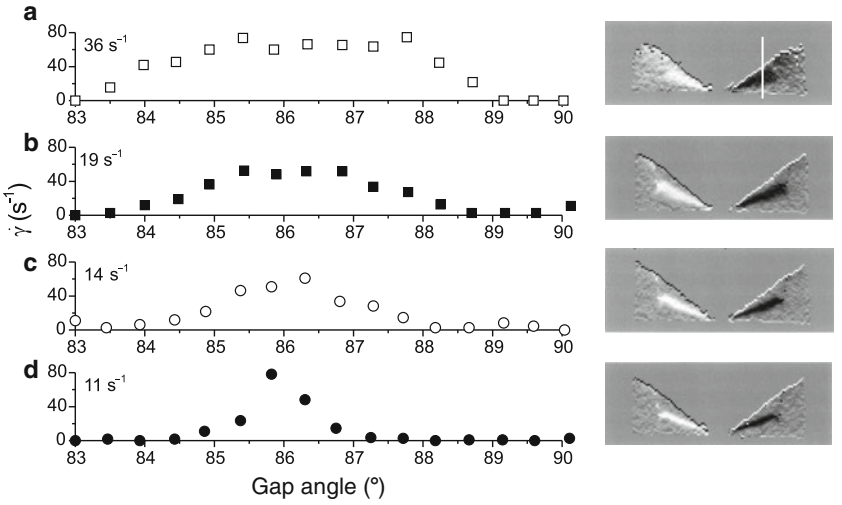

Fig. 16 Time-averaged shear rate profiles and corresponding gray scale images for the CPCl (100 mM)/NaSal (60 mM) ($c = 4.5$ wt. %) solution at $T = 25°$C, measured using NMR velocimetry in a 7° cone-and-plate at different applied macroscopic shear rates (**a**) $11\,\mathrm{s}^{-1}$, (**b**) $14\,\mathrm{s}^{-1}$, (**c**) $19\,\mathrm{s}^{-1}$, and (**d**) $36\,\mathrm{s}^{-1}$. The profiles are extracted along a line (*in white*) at fixed radius from the cone axis as illustrated on the images at *right*. The gray scale indicates the shear rate in arbitrary units. Note the opposite sign shear for the receding and advancing segments of fluid on opposite sides of the gap. The "free" surface of the fluid is in contact with a containment jacket in Teflon, leading to vanishing of the gradient banding structure beyond a critical radius. Each measurement requires an acquisition time of about 2 h. Reprinted with permission from Britton et al. [150]

In Couette geometry, a thin high-shear band ($\simeq$30 μm) near the inner cylinder but in the bulk of the fluid as well as wall slip have been detected [145, 146]. A different picture emerged from the NMR-study of the 10 wt. % CPCl/NaSal in brine [159]: the shear-banding structure was composed of two macroscopic layers bearing different shear rates, the lower one being compatible with the $\dot{\gamma}_1$ value. The width of the high shear rate band was found to increase significantly with the applied shear rate while wall slip was observed at the moving wall. Enhanced local velocity fluctuations have been reported in the high shear rate region at the vicinity of the inner rotating cylinder.

Very similar time-averaged velocity profiles in Couette geometry have also been determined using heterodyne dynamic light scattering (DLS). This technique, developed by Salmon and coworkers, is based on the analysis of the correlation function of the interference signal generated by the mixing of a reference beam and the light scattered by a small volume of sample (typically $(50\,\mu m)^3$) [247]. The scattering signal is enhanced by nanoparticles embedded in the fluid. A few seconds are required to yield the mean velocity for each scanned scattering volume, the total duration for the acquisition of a complete profile reaching a few minutes. This technique has been implemented to examine the precise local structure of the flow in the much-studied 6 wt. % CPCl/NaSal in brine [155, 156]. Figure 17 summarizes the typical velocity profiles gathered for various applied shear rates all along the flow curve, the latter being recorded in a simultaneous way. For $\dot{\gamma} < \dot{\gamma}_1$, the velocity profile is continuous and nearly linear, with a slight curvature typical of a weakly shear-thinning fluid, consistent with the evolution of the high-viscosity branch. For $\dot{\gamma}_1 < \dot{\gamma} < \dot{\gamma}_2$, the velocity profiles become discontinuous, and are composed of two linear regions of well-distinct slopes. The flow is then nonhomogeneous with two coexisting layers supporting very differing local shear rates, the values of which are compatible with $\dot{\gamma}_1$ and $\dot{\gamma}_2$. Note that rapid temporal fluctuations of the flow field in the high shear

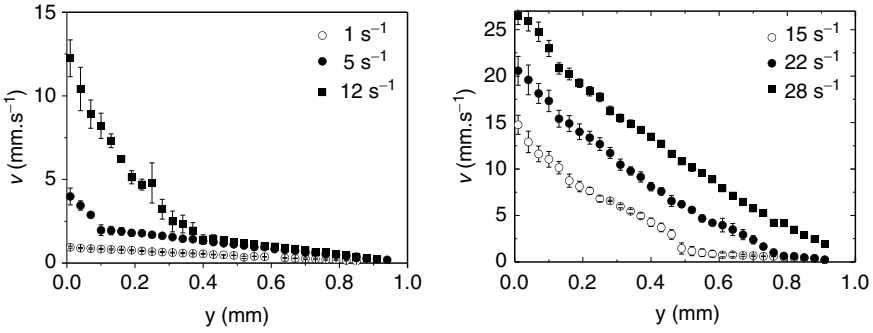

Fig. 17 Velocity profiles obtained using heterodyne dynamic light scattering for different mean shear rates along the flow curve: $\dot{\gamma} = 1\,s^{-1}$, $\dot{\gamma} = 5\,s^{-1}$, $\dot{\gamma} = 12\,s^{-1}$, $\dot{\gamma} = 15\,s^{-1}$, $\dot{\gamma} = 22\,s^{-1}$, and $\dot{\gamma} = 28\,s^{-1}$. For reference, the stress plateau extends from $\dot{\gamma}_1 \simeq 2.5\,s^{-1}$, and $\dot{\gamma}_2 \simeq 26\,s^{-1}$. The sample is 6 wt. % CPCl/NaSal in brine and is sheared in a Couette device at a temperature of 21.5 °C. The inner rotating and outer cylinders are marked, respectively by the positions $y = 0$ and $y = 1$ mm. The *errors bars* are representative of temporal fluctuations. Reprinted with permission from Salmon et al. [156]

rate band were reported. The increase of the applied shear rate $\dot{\gamma}$ along the stress plateau only affects the relative proportions f and $1-f$ of both bands: $1-f$ was found to increase linearly with $\dot{\gamma}$, hence satisfying the classical lever rule (Eq. 3). Finally, for $\dot{\gamma} > \dot{\gamma}_2$, the flow appears homogeneous again: the velocity profiles are characteristic of a strongly shear-thinning fluid, consistent with the evolution of the low viscosity branch. These experiments provided evidence for the classical shear-banding scenario invoked in the introduction (Sect. 3.1).

This type of velocity profiles, showing the coexistence of two differently sheared regions, the relative proportions of which vary with the applied shear rate, has also been measured using PIV and USV in Couette geometry on CPCl/NaSal in brine [157, 158] and C_{16}TAB/NaSal [187]. However, other features have sometimes been reported, including organization of the high shear band into multiple bands, variation of the local shear rate in each band with the control parameter, and wall slip at the moving inner wall.

Concentrated Systems

The structure of the flow field has also been explored in the concentrated regime. Fischer et al. carried out NMR velocimetry experiments in Couette geometry on a sample of C_{16}TAB/D_2O at 20 wt. %, a concentration just below c_{I-N}. For the investigated mean shear rates in the plateau region, the authors identified wall slip at the inner moving wall together with the following banding sequence: low-high-low shear rate bands stacked from the inner to the outer cylinder [169, 170]. The shape of the velocity profile near the moving inner cylinder was interpreted as evidence for near rigid body motion. As we shall see later in the section devoted to the microstructure of the coexisting phases, the comparison of these velocity profiles with ordering profiles simultaneously gathered from NMR spectroscopy experiments led the authors to argue that, surprisingly, the induced nematic state is a state of high viscosity, possibly associated with mesoscale ordering. In addition, local fluctuations of the flow field were suggested from the analysis of the velocity distribution at each pixel across the gap.

Bécu et al. studied the same system using high-frequency USV. This technique, developed by Manneville and coworkers [248], is based on cross-correlation of high frequency ultrasonic signals backscattered by the moving fluid. The signals consist of ultrasonic speckles resulting from the interferences of echoes from micrometric scatterers suspended in the fluid. The displacement of the scatterers is estimated from the time shift between two successive echoes. Full velocity profiles are recorded every 0.02–2 s, depending on the shear rate, with a spatial resolution of 40 µm. By averaging velocity profiles over 100 s, the authors observed a similar banding sequence, with an apparently unsheared region at the vicinity of the inner moving cylinder where the fluid velocity is slightly larger than the rotor velocity [172]. Their interpretation of these peculiar profiles differed somewhat from the previous one, incriminating a three-dimensional flow instability. We will come back on that point in Sect. 3.3.2.

Thereby, all these experiments confirm that the stress plateau in semidilute and concentrated micellar solutions is effectively associated with nonhomogeneous flow. They also reveal the existence of fluctuations of the flow field and address the question of the role played by wall slip. However, a unified picture of shear-banding has not emerged from the measurement of these time-averaged velocity profiles. A spatio-temporal approach with enhanced resolution is then required to get a better description of the shear-banding transition. Taking into account this need for high temporal resolution to follow the dynamics of the flow field, some groups have improved their velocimetry technique [249], while others have developed new powerful probes [157, 158, 248].

3.3.2 Time-Resolved Velocity Profiles

Transient Behavior

The early stages of banded-state formation have been studied on different solutions of CPCl/NaSal in brine [157, 158]. Using a PTV method, Hu et al. investigated the kinetics of shear-banding on the CPCl/NaSal (6.3 wt. %) in 0.5 M NaCl brine [157]. PTV only differs from PIV by the image processing, which is based on particle tracking rather than spatial correlation. This yields an improved spatial resolution ($\simeq$10 µm). Interestingly, the time evolutions of the velocity profiles and the shear stress have been monitored simultaneously, providing information on the correlation between local and global rheology. The transient stress response after start-up of flow of this system has been discussed in Sect. 3.2.2.

Figure 18 illustrates the corresponding transient velocity profiles. For $t < \tau_R$, the velocity profiles are linear across the gap of the Couette device: the flow is homogeneous with no wall slip at the walls (see Fig. 18a). When the stress overshoot occurs, the local behavior is found to depend on the applied shear rate. For huge overshoots, significant wall slip is detected at the inner wall, and the velocity profile takes an abnormal shape ($t = 0.9$ s). During the short-time relaxation of the stress overshoot, the homogeneous flow is restored. The velocity profile appears then slightly curved ($t = 2$ s), the local shear rate increasing towards the inner wall and decreasing towards the outer wall. This process has been ascribed to coupling between stress gradient inherent to the flow geometry and chain disentanglement. When the local shear rate at the outer wall reached the critical value $\dot{\gamma}_1$ ($t \simeq 3.6$ s), the low shear band begins to grow. The expansion of the low shear band towards the inner cylinder together with the increase of the local shear rate in the high shear band are linked to the slow stress relaxation towards steady state including the small undershoot (Fig. 18b). The stationary state is characterized by two well-defined shear bands with a relatively broad interface, the position of which fluctuates as a function of time. Contrary to the observations of [156], the local shear rates in each band varies with the imposed shear rate. Under stress-controlled conditions, the development of the banding structure was somewhat different: the kinetics was much slower and the curvature of the initial linear profile was followed by the nucleation and growth of

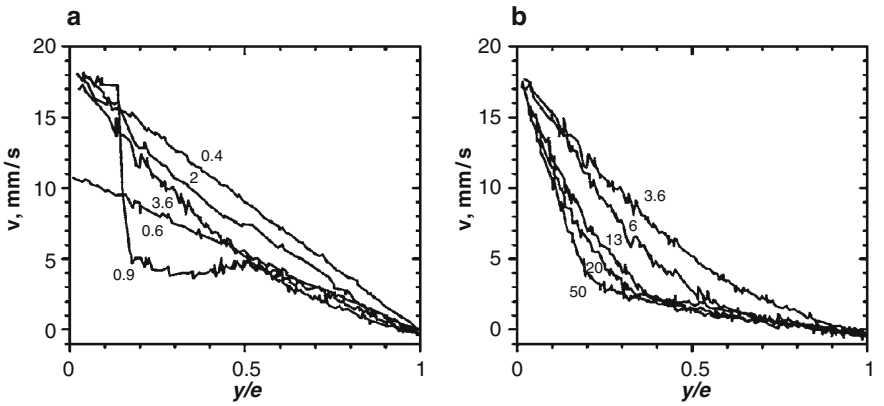

Fig. 18 Velocity profiles as a function of time at $\dot{\gamma} = 10\ s^{-1}$ obtained in a Couette device of gap e using PTV. The spatial resolution is 10 µm. The micellar system is the 6.3% w/v CPCl and NaSal at molar ratio $R = [Sal]/[CPCl] = 0.5$, in 0.5 M H_2O NaCl brine at $T = 23\,°C$. The kinetics of formation of the banding structure is composed of two main stages. (**a**) A short-time response where the flow stays homogeneous most of the time with increasing and decreasing local shear rates respectively at the inner and outer walls. (**b**) Growth of the low shear rate band from the outer wall. Reprinted with permission from Hu et al. [157]

the high shear rate band from the inner rotating cylinder. Note that, using PIV with a high-speed camera, Miller et al. also identified multi-stages development of the banding structure [158].

Fluctuating Behaviors

Using fast NMR velocimetry imaging, Lopez-Gonzalez et al. gathered two-dimensional full velocity profiles every second for a semidilute sample of CPCl/NaSal in 0.5 NaCl brine [161, 250]. The usable extension of the velocity map along the flow and the gradient directions was 5 mm and the data were averaged over 5 mm along the vorticity direction. The long-times flow dynamics was studied for a fixed applied shear rate $\dot{\gamma} = 37\,s^{-1}$. The corresponding stress time series, recorded independently, exhibited fluctuations of about 5% around its mean value. Time-resolved velocity profiles across the 1-mm gap extracted from a one-dimensional slice of the velocity map are displayed in Fig. 19. In addition to the banding structure described for this system in Sect. 3.3.1, the authors demonstrated that the position of the interface between bands strongly fluctuates as a function of time. The high shear rate band (light gray zone in Fig. 19) supports a roughly constant shear rate ($\dot{\gamma} \simeq 70\,s^{-1}$) and its width is strongly correlated to the degree of slip at the inner moving wall. The fluctuations are quasi-random or periodic, depending on sample preparation, and seem then to be driven by wall slip. A frequency analysis revealed that the correlation time ($\simeq$10 s) is of the same order of

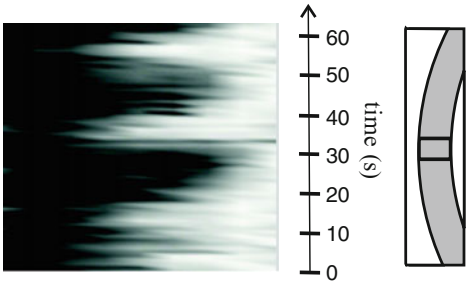

Fig. 19 Velocity profiles as a function of time, recorded at 1-s intervals using rapid NMR imaging in Couette device for an imposed shear rate $\dot{\gamma} = 37\,\mathrm{s}^{-1}$. The left and right sides of the gray scale map correspond respectively to the outer and inner cylinders. The gray levels give the magnitude of the velocity, ranging from 0 to $25\,\mathrm{mm\,s}^{-1}$. The spatial resolution is $100\,\mu\mathrm{m}$. The micellar system placed in the 1 mm gap is made of 10% w/v CPCl and NaSal at molar ratio $R = [\mathrm{Sal}]/[\mathrm{CPCl}] = 0.5$, in0.5 M H_2O/NaCl brine. The temperature is kept at 25 °C. Reprinted with permission from Lopez-Gonzalez et al. [160]

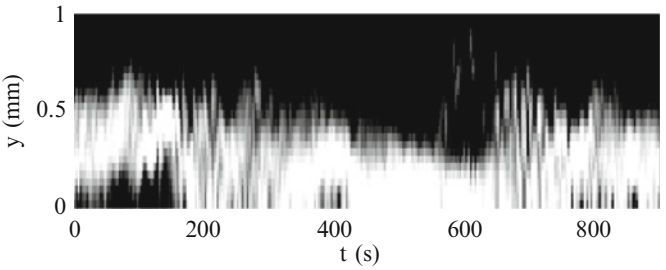

Fig. 20 Map of the local shear rate $\dot{\gamma}(y,t)$ determined using USV, for a 20 wt. % C_{16}TAB/D_2O concentrated micellar system after start-up of flow at a fixed shear rate $\dot{\gamma} = 50\,\mathrm{s}^{-1}$ in the banding regime. The extremum values of the gray scale are associated with $\dot{\gamma} = 0\,\mathrm{s}^{-1}$ (*black*) and $\dot{\gamma} > 120\,\mathrm{s}^{-1}$ (*white*). The positions $y = 0$ and $y = 1$ correspond, respectively, to the inner moving and outer fixed cylinders. The temperature is kept at 41 °C. Reprinted with permission from Bécu et al. [172]

magnitude as that observed in stress fluctuations. Moreover, along the 5 mm of the observation window in the velocity direction, the velocity profiles did not change.

Similar fluctuations of the banding structure have been observed on the C_{16}TAB/D_2O (20 wt. %) concentrated system using high frequency USV [171, 172]. The typical features of the flow dynamics in response to a step shear rate are illustrated in the gray scale map of $\dot{\gamma}(y,t)$ in Fig. 20. First, strong erratic fluctuations of the interface position between the two shear bands from $y \simeq 0.3$ to $y \simeq 0.5$ mm occur on time scales ranging from 3 to 200 s. They are correlated to the dynamics of the slip velocities. Second, an unsheared zone appears intermittently in the vicinity of the inner cylinder, with a spatial extension between 200 and 400 µm. During this process, the time-dependent velocity profiles are highly unstable and composed of three distinct shear bands. The authors emphasized that the local velocity in the unsheared region passes through a maximum that overcomes the rotor

velocity, a feature also observable in [170]. Taking into account their experimental configuration, they interpreted this particular shape of velocity profiles as the signature of three-dimensional flow. This assumption was reinforced by the organization of the ultrasonic tracers into patterns along the vorticity direction.

Vorticity Banding

Herle et al. [229] investigated the equimolar solution CPCl (40 mM) and NaSal (40 mM) ($c = 2.1$ wt. %) that exhibits a complex flow curve with successively Newtonian, shear-thinning, and shear-thickening regimes (see Sects. 3.2.1 and 3.2.2). They performed pointwise USV velocimetry measurements in Couette geometry with the stress as the control parameter. In the shear-thinning region, the flow was homogeneous. At the onset of the shear-thickening regime, the authors observed the presence of two radial bands supporting different shear rates. At higher imposed shear stresses, coexistence of both radial and vorticity bands has been identified. Large temporal oscillations of the velocity profiles have been reported, related to periodic appearance and disappearance of the vorticity bands.

Note that the same system has been explored using PIV in capillary flow [230]. The flow curve built from the local velocity profiles was consistent with that obtained from the bulk rheology. Above the critical wall stress, shear-thickening zones characterized by convexity in the velocity profiles were observed, extending roughly on half of the capillary diameter. Spatio-temporal oscillations of these profiles together with stick-slip were mentioned, leading to continuous creation and breakage of the induced structures. Similar coupling between changes in the microstructure and stick-slip has been also suggested to explain the "apparent" shear-thickening branch of the C_{16}TAB (50 mM)/NaSal (100 mM) ($c = 3.4$ wt. %) solution [187].

3.4 Structural Characterization of the Banded State: Rheo-Optics, Scattering, and Spectroscopy

In Sect. 3.3.2, the existence of shear bands at constant stress has been demonstrated. The shear bands have differing viscosities and consequently different internal structures. A way to collect additional information is then to probe the microstructural organization of the system. Different tools have been used to study the shear-banding transition in wormlike micelles, including flow birefringence (FB), small angle neutron and light scattering (SANS and SALS), and NMR spectroscopy. As in the case of the velocimetry, most of these experimental techniques have been improved to give a space- and time-resolved description of the transition. In the following, we focus on the local structure of the banded state and on the potential connections with the bulk rheology and the local flow field.

3.4.1 Characterization of the Shear-bands Under Steady Flow

Direct Observation Using Flow Birefringence

The first evidence for band separation in wormlike micellar solutions came from flow birefringence experiments performed on a concentrated solution by Decruppe and coworkers [167]. The experimental configuration was as follows: the sample, placed in the gap of a Couette geometry, was illuminated with a white light source and visualized between crossed polarizers. The transmitted intensity was recorded on a digital camera, the spatial resolution reaching 15 µm. Figure 21 shows six photographs of a 1-mm gap filled with a system CPCl/Hex in 0.2 M brine, illustrating the typical scenario observed in concentrated giant micelles [44]. Figure 21a is representative of the optical behavior along the high viscosity branch: the gap of the Couette cell appears dark and the birefringence intensity and the average orientation of the micellar medium are homogeneous. Once the first critical shear rate $\dot{\gamma}_1$ is reached, a highly birefringent bright band nucleates against the moving inner cylinder and coexists with a dark band of differing optical properties. The location of the induced band at the inner cylinder is explained by the stress gradient inherent to the Couette geometry [251, 252]. The stress varies as $1/r^2$ in the gap, implying that the state of higher stress is reached at the inner wall. When the applied shear rate is further increased along the stress plateau, the bright band broadens (see Fig. 21b–e), the orientation state of the system remaining unchanged in each band as demonstrated by pointwise FB [153, 158, 191]. Finally, above $\dot{\gamma}_2$ the gap is entirely filled by the highly birefringent and oriented shear-induced structures (Fig. 21f).

This scenario was originally interpreted as evidence of the shear-banding transition, the states of low and high shear rates being deduced from the molecular

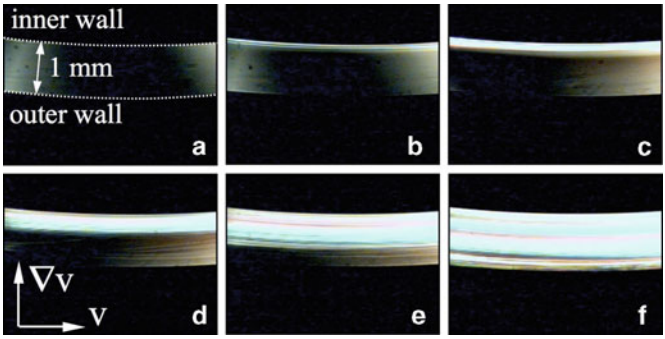

Fig. 21 Snapshots of the 1-mm gap of a Couette cell containing a concentrated solution of CPCl-Hex at respective concentrations $c_{CPCl} = 28$ wt. % and $c_{Hex} = 3.9$ wt. % for different applied shear rates along the flow curve. The sample is illuminated with white light and observed between crossed polarizer and analyser. The orientation of the polarizer is chosen to match the mean orientation of the micelles in the band adjacent to the fixed cylinder. This configuration makes the latter dark and improves the contrast between bands. Exposure times are typically of the order of milliseconds. With increasing shear rates (from **a** to **f**), the bright induced band fills up the gap progressively. Reprinted from Berret [44]

alignment in each band. From a general point of view, it has been observed in concentrated solutions such as C_{16}TAB in water and C_{16}TAB/D_2O [167, 168] and in several semidilute samples, e.g., in C_{16}TAC/NaSal [208, 211], C_{16}TAB/KBr/H_2O and –D_2O [188, 190, 191], CPCl/NaSal [137, 157], C_{16}TAB/NaSal [177, 186], and C_{16}TAB/$NaNO_3$ [144, 194]. Notwithstanding, careful examination of the "steady-state" banding structure revealed important differences in the spatial organization from a sample to another with, for example, heterogeneities of the induced bright band or multiple bands [137, 144, 153, 157, 158, 177, 188, 191].

In this context, the question of the correspondence between shear and birefringence bands has been raised by some authors [169, 170]. In recent studies of semidilute CPCl/NaSal solutions, simultaneous measurements of velocity profiles and optical visualizations were performed, showing a good agreement between shear and birefringence bands [157, 253]. However, this correlation did not seem so obvious for other systems [169, 170]. We will see later (Sect. 3.4.2) using time-resolved birefringence measurements that all these features could certainly be explained by the existence of fluctuations already revealed by velocimetry experiments.

Quantitative measurements of the birefringence intensity Δn and extinction angle χ (Eq. 2) carried out with convenient arrangements of optical components [254] have shown a general steady evolution compatible with that of the shear stress: the absolute value of Δn first increases linearly with $\dot{\gamma}$ while, in the same time, χ decreases smoothly from 45°, indicating a gradual alignment of the micelles with respect to flow direction. Above $\dot{\gamma}_1$, both quantities exhibit a discontinuity of slope followed by a plateau, characteristic of the coexistence of the dark and bright bands [144, 153, 158, 167, 174, 179, 191, 208]. Typically, dark and bright bands have birefringence intensity of the order of -10^{-5} and -10^{-3} (the negative sign of Δn is due to the anisotropy of the polarisability tensor associated with the monomeric surfactant chain [174, 255]), and extinction angle ranging from 20° to 40° for the dark band and of the order of a few degrees for the bright band. This indicates that the induced structures are strongly aligned with respect to the flow direction. Note that the stress-optical law, which establishes a linear relationship between stress and refractive index tensors, does not hold in the shear-banding regime [174, 189, 211, 255].

Nature of the Induced Phases

Concentrated Systems

Various micellar solutions, at a concentration close to the isotropic-to-nematic transition at rest, have been studied using SANS [168, 173, 197, 198] and NMR spectroscopy [169, 170].

SANS gives information on the orientational degrees of freedom of a fluid subjected to flow and has been used to probe the structure of these systems for shear rates all along the flow curve. The sample was placed in a Couette device and two-dimensional scattering patterns were collected in radial configuration, the incident neutron beam passing through the cell along the velocity-gradient direction. For

shear rates along the high viscosity branch, the scattering consists of an isotropic ring and exhibits a broad maximum resulting from strong translational correlations between the micellar threads. The order of magnitude of the distance between micelles, estimated from the position of this maximum, is typically 6–9 nm. In the plateau regime, the scattering function becomes anisotropic, with crescent-like peaks in the vorticity direction. Finally, along the low viscosity branch, at high shear rates, the ring-like structure vanishes and the scattering is dominated by anisotropic pattern, qualitatively analogous to that obtained from a micellar solution which is nematic at rest and subjected to a moderate shearing. These results, showing that the macroscopic phase separation observed in flow birefringence corresponds to shear-induced isotropic-to-nematic transition, have been reported in several systems such as $CPClO_3/NaClO_3$ [173], CPCl/Hex [197, 198], and $C_{16}TAB/D_2O$ [168]. In addition, the nematic order parameter and the proportions and concentrations of each phase as a function of shear rate in the plateau regime could be derived from the SANS spectra. Breakdown of the simple lever rule has been observed [168, 198], and for the CPCl-Hex system the I-N transition was supposed to result from flow-concentration coupling [198].

NMR spectroscopy is also useful to probe the local microstructure. It allows one to resolve spatially the spectral splitting associated with the quadrupolar interactions of the deuteron nuclei with the local electric-field gradient. This splitting is actually proportional to the order parameter of the phase that is initiated. Should this splitting be zero, the phase is disordered; should it be nonzero, the phase is nematic. The splitting is actually due to the fact that, in an oriented nematic phase of micelles, the D_2O molecules of the solvent inherit the alignment of the cylindrical structures. For a detailed description of this technique, the reader can refer to [249, 256]. NMR spectroscopy brought confirmation about the nematic order of the induced phase in the $C_{16}TAB/D_2O$ concentrated sample (20 wt. %) as illustrated in Fig. 22 [169, 170]. At a given shear rate, the splitting characteristic of an ordered phase is clearly visible near the inner moving cylinder, while the spectra at the fixed wall are composed of a single peak, indicative of isotropic phase. The completely ordered and isotropic phases are separated by a mixed region. The existence of broad isotropic and nematic bands is compatible with birefringence observations on the same system [168]. Note that, in contrast, the corresponding NMR velocity profiles do not seem to be correlated in an obvious way with this simple picture (see Sect. 3.3.1). Notwithstanding, velocity profiles measured using USV seem in reasonable agreement with ordering profiles [172].

Relative volume fractions of each phase could be computed from the NMR spectra and were found in remarkable agreement with the SANS data.

Semidilute Systems

For semidilute micellar solutions at concentrations far from the isotropic-to-nematic boundary at rest, the situation is less clear, insofar as the set of structural data on different standard systems available in the literature is reduced, making a definite conclusion about the nature of the induced structures difficult.

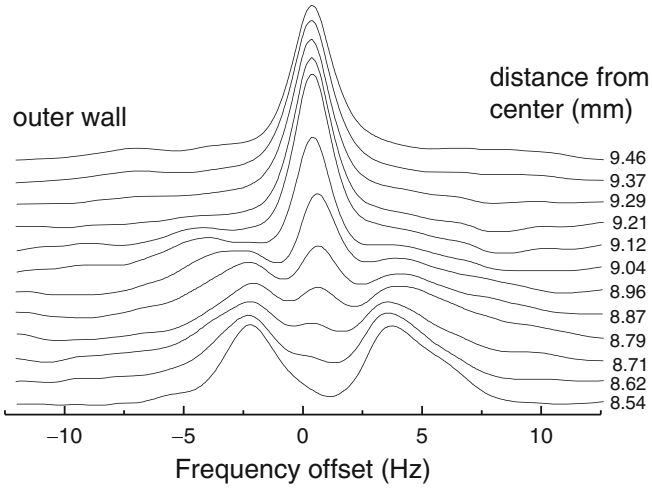

Fig. 22 ^{2}H NMR spectra obtained from 20 wt. % $C_{16}TAB/D_2O$ (41 °C) at different positions across the gap of a cylindrical Couette cell. The applied shear rate is 20 s^{-1}. Near the inner wall, a quadrupole splitting is observed, consistent with a nematic phase, while near the outer wall the single peak of an isotropic phase is seen. Both regions are separated by a mixed phase. Reprinted with permission from Fischer et al. [169]

NMR spectroscopy has been used to investigate the local structure of the 10 wt. % CPCl/NaSal (molar ratio 2:1) in 0.5 M NaCl brine [161, 250]. The shear-induced alignment of the micelles was measured by introducing a deuterated dodecane probe molecule into the micellar core. For applied shear rates belonging to the plateau region, splitting of the NMR spectra were observed, indicating a nonzero order parameter, strongly suggestive of nematic order. The volume fraction of the shear-induced nematic phase was found to increase linearly with the mean shear rate and seemed then to follow a simple lever rule. Moreover, proton NMR spectroscopy revealed a strong correlation between molecular orientational dynamics and shear stress.

Shear-induced isotropic to nematic phase transition has also been reported in semidilute wormlike micelles solutions with excess of salt or strongly binding counterions, forming multiconnected networks [182, 214]. Such a string-like phase has been observed using polarized SALS under shear and manifests itself by anisotropic SALS patterns characterized by butterfly or tulip-like shapes with enhanced scattering in the flow direction superimposed to bright streak perpendicular to the flow direction [178–181]. These features of the scattering patterns indicate shear-enhanced concentration fluctuations [257] at different length scales and are usually accompanied by turbidity and flow dichroism [214]. Recent pointwise SANS experiments on these systems suggested that the high shear rate band, which was turbid and appears strongly striated, was composed of a highly branched concentrated micellar solution coexisting with a nearly isotropic, brine phase [258].

Such SALS patterns and shear-induced turbidity have been highlighted in the equimolar CPCl/NaSal system exhibiting vorticity banding (see Sect. 3.2.2) [222, 226,227], but also in more classical semidilute systems [144,157,177,194–196,200, 236, 253]. In those cases, these phenomena are strongly time- and space-dependent and will be addressed in the following section.

3.4.2 Time-Dependent Behaviors

Transient Behaviors

The formation of the banding structure has been explored using FB, direct visualisations, SALS and turbidity measurements in various semidilute wormlike micelles systems including C_{16}TAB/NaSal, C_{16}TAB/KBr, C_{16}TAB/$NaNO_3$, CPCl/NaSal in brine [144, 153, 157, 158, 177, 191, 194–196]. Note that, in each case, the transient rheology after a sudden step shear rate in the coexistence zone followed the "standard behavior" evoked in Sect. 3.2.2. Interestingly, the temporal evolution of the birefringence intensity and extinction angle, averaged over the gap thickness, showed strong quantitative analogies with that of the shear stress.

The short-time response was dominated by an overshoot and was followed by a stretched exponential or damped oscillations depending on the applied shear rate. The subsequent behavior was a slow variation towards steady state that could be related to the small undershoot observed in $\sigma(t)$ [144, 191].

Figure 23 illustrates the main stages of formation of the banding state for a semidilute mixture of C_{16}TAB (0.3 M) with $NaNO_3$ (0.405 M) ($c = 11$ wt. %) under controlled shear rate.

- *Step 1*: At the onset of the simple shear flow, the entire gap becomes turbid (photo 2). The maximum of scattered intensity is reached when the overshoot in σ, Δn, and χ occurs. The observed turbidity is then supposed to result from the orientation and the stretching of the micellar network [144, 177, 191, 194], generating concentration fluctuations along the flow direction [257] as suggested by butterfly patterns observed using two-dimensional SALS experiments under shear [157, 194]. At this time, all the new phase is nucleated but not arranged into a macroscopic band.
- *Step 2*: The building of the banding structure starts with the relaxation of the stress overshoot. One can observe the formation of a diffuse interface that migrates from the fixed wall towards its stationary position in the gap and progressively sharpens (see photos 3–5). The corresponding behavior in the shear stress response is the sigmoidal relaxation or the damped oscillations depending on the magnitude of the averaged shear rate.
- *Step 3*: When the front is sharp and has reached its equilibrium position, first signs of interface destabilization along the vorticity direction are observed (photo 6). The instability grows with time and finally saturates (photos 7–9). The final state corresponds to the coexistence of a turbid band with a nonturbid band, separated by an undulating interface with well-defined wavelength and finite

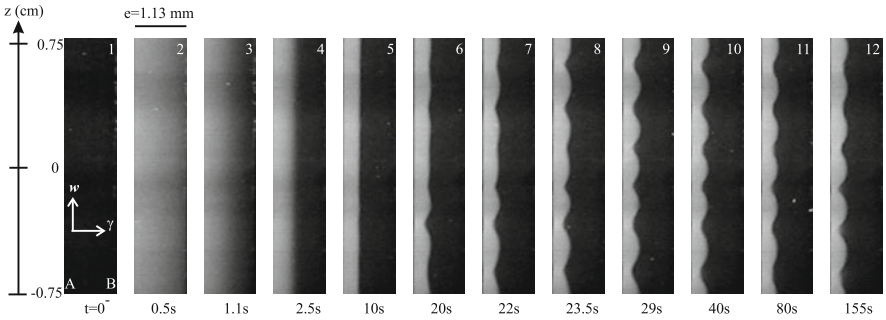

Fig. 23 Views of the 1.13-mm gap in the plane velocity gradient/vorticity taken out from the recording of the scattered intensity at different times during the formation of the induced band at a shear rate of $30\,s^{-1}$. The sample made of $C_{16}TAB$ (0.3 M) and $NaNO_3$ (0.405 M) ($c = 11$ wt. %) at $T = 30°C$ is initially at rest and does not scatter the laser light (photo 1). The experimental configuration is as follows: a transparent Couette cell is illuminated with a thin laser sheet propagating along the velocity gradient direction and the intensity scattered at 90° of the incident beam is recorded on a digital camera. The scattering signal is gathered simultaneously with the temporal stress evolution allowing precise correlation of the structural and mechanical responses. The left and right sides of each picture correspond respectively to the inner and the outer cylinders. Due to the compromise between the spatial resolution and the size of the field of observation, this latter is limited to 1.5 cm in height (the total height of the inner cylinder is 4 cm) and centered at halfway of the cell. Reprinted from Lerouge et al. [195]

amplitude (photo 12). Note that such different scattering properties in each band have also been reported in [153,157] using polarized SALS. The part of the stress dynamics corresponding to the appearance and the development of the interface instability is the small undershoot that precedes steady-state [195,196].

A crucial point in this time sequence is that the small undershoot in the $\sigma(t)$ curve appears as the mechanical signature of the interface instability. Since the undershoot has been detected on other semidilute systems (see Sect. 3.2.2), this suggests that the interfacial instability is presumably not inherent to this particular solution.

Dynamics of the Banding Structure

If the early stages of formation of the banding structure seem to be common to various semidilute solutions, the space and long-time responses strongly differ from one sample to another.

Figure 24 displays, for example, the long-time dynamics of a $C_{16}TAB/NaNO_3$ solution ($c = 11$ wt. %) sheared at $\dot{\gamma} = 8\,s^{-1}$ in a 1.5-mm gap of a Couette cell and observed between crossed polarizers. For reference, the critical shear rates for this sample are $\dot{\gamma}_1 = 5\,s^{-1}$ and $\dot{\gamma}_2 \simeq 110\,s^{-1}$. As expected along the stress plateau, the fluid is split into two bands of strongly differing optical properties. The band located against the fixed cylinder is homogeneous. However, a careful examination of the induced band reveals additional features: the latter appears striated and is composed of

Fig. 24 Illustration of fluctuating behavior of the banding structure on long time scale. The sample, made of C_{16}TAB (0.3 M) and $NaNO_3$ (1.79 M) ($c = 11$ wt. %) is sheared at $\dot{\gamma} = 8\ s^{-1}$ in the annular gap of a Couette cell placed between crossed polarizers and illuminated by a source of white light. The temperature is fixed at 30 °C. The observation is realized in the $(\mathbf{v}, \nabla v)$-plane. The inner rotating cylinder and the outer fixed wall of the Couette cell are indicated by the letters **a** and **b**, respectively. Reprinted from Lerouge et al. [144]

fine sub-bands, the typical thickness of which is estimated to be 100–150 µm. These sub-bands are characterized by differing refraction index. They continuously nucleate from the inner rotating cylinder and migrate towards the outer fixed wall. The interface between the two macroscopic bands seems unstable and shows fluctuations of position, reminiscent of the pictures observed in velocimetry (see Sect. 3.3.2). Note that the striations extend over approximately half of the gap width. Taking into account the boundaries of the stress plateau, the birefringence bands observed here do not follow a simple lever rule.

This type of dynamical behavior has also been reported in various CPCl/NaSal solutions using FB and SALS [138, 153, 157]. Hu and Lips [157] also brought new insights about the fine structuring of the induced band. The simultaneous recording of the velocity profiles showed that the sub-bands support the same local shear rate. Besides, cessation of flow experiments suggested that the sub-bands relaxation time was larger than the macroscopic shear bands lifetime.

The fluctuating character of the interface between bands highlighted from space- and time-resolved velocimetry and optical experiments, appears then as a robust feature of the shear-banding flow in giant micelles systems. With regard to one-dimensional velocimetry measurements, the experimental configuration of Fig. 23 enables to follow the spatiotemporal dynamics of the interface using two-dimensional scattering in the velocity gradient-vorticity plane.

Three main regimes of dynamics have been highlighted along the stress plateau as illustrated in Fig. 25 where the gray levels materialize the position of the interface in the gap. Figure 25a displays a typical spatiotemporal sequence at low shear rates. After a transient including construction, sharpening and migration of the interface, the pattern exhibits, on large scale, a well-defined wavelength of approximately half of the gap width. At smaller scale the dynamics is more complex: the pattern oscillates along the vertical direction of the cell and waves propagate towards the bottom and the top of the cell. At intermediate imposed shear rates in the coexistence zone, the interface keeps a spatially stable profile over very long times. The wavelength of the interface undulation is about three times the gap width (Fig. 25b). The amplitude of the interface profile is modulated in course of time.

For the highest shear rates in the plateau region, emergence of complex dynamics of the interface is observed (cf. Fig. 25c). After a transient slightly under 200 s,

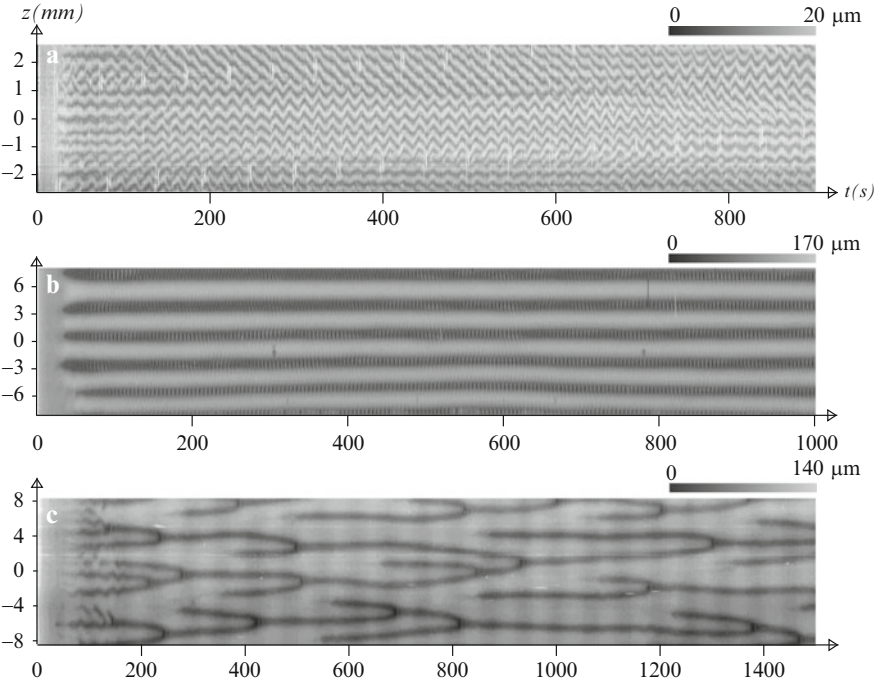

Fig. 25 Spatiotemporal evolution of the interface position in the gap of the Couette cell during a step shear rate from rest to (**a**) $\dot{\gamma} = 6.5\,s^{-1}$, (**b**) $\dot{\gamma} = 30\,s^{-1}$, (**c**) $\dot{\gamma} = 70\,s^{-1}$. The position of the interface in the gap is given in *gray scale*, the origin being taken at the inner moving wall so that *dark gray regions* correspond to positions of the interface nearer to the inner cylinder than *light gray regions*. The z-axis represents the spatial coordinate along the cylinder axis. The sample is made of C_{16}TAB (0.3 M) and $NaNO_3$ (0.405 M) ($c = 11$ wt. %) at $T = 28°C$. Reprinted from Lerouge et al. [196]

the amplitude of the interface profile saturates while the wavelength continuously evolves over time: two neighboring minima have a tendency to merge and when the distance between a pair of minima increases, several other minima close to this pair nucleate and finally merge again with a minimum of longer lifetime. The system does not seem to tend toward a stationary situation and the spatiotemporal diagram strongly suggests chaotic dynamics.

Case of Vorticity Banding

In Sect. 3.2.2, we mentioned the particular time-dependent rheological behavior of an equimolar solution of CPCl/NaSal ($c = 2.1$ wt. %). The shear-thickening transition was characterized by strong oscillations as a function of time in the shear and normal stresses at fixed shear rate (or vice versa). Using direct visualizations and SALS experiments, the authors showed that these oscillations were correlated

with the existence of a pattern made of clear and turbid rings stacked along the vorticity direction, the position and intensity of which alternate in course of time [169, 222, 226, 227]. This complex dynamics, where formation and destruction of shear-induced structures couple with flow instabilities, has been observed in parallel plate, cone and plate and Taylor–Couette cells. Although the development of these spatiotemporal patterns was robust in reference to the flow geometry, the frequency and the amplitude of the oscillations in the bulk rheology were found to depend on the gap width [227], suggesting that the shear induced structures need some space to develop fully. Recent pointwise SANS and video imaging experiments revealed that both clear and turbid bands contain strongly aligned structures [228]. Note that vorticity structuring has also been observed in shear-thickening polymer solutions [259] and in shear-thinning viral suspensions [125, 260, 261].

3.5 Conclusion

In this part we have described the nonlinear behavior of semidilute and concentrated wormlike micelles under simple shear flow. Taking into account the list established in Table 2, we can argue that most surfactant wormlike micelles present a "standard rheological behavior" at steady state, characterized by the existence of a stress plateau in the flow curve. The results accumulated during the last two decades using different velocimetry and optical techniques show unambiguously that the stress plateau is associated with a shear-banding transition. Probing the flow field and the local structure in the $(\mathbf{v}, \nabla v)$-plane leads to a minimal one-dimensional scenario for the base flow, at least when time-averaged measurements are considered: all the velocimetry techniques (NMR imaging, DLS, PIV, PTV, and USV) show that, once the stress plateau is reached, the sample splits into two macroscopic layers bearing different shear rates and stacked along the velocity gradient direction. When the control parameter is increased, the high shear rate band progressively invades the gap of the shearing cell. Birefringence experiments also support this basic picture. The degree of orientation in each layer is very different and the induced structures in the high shear rate band are strongly aligned along the flow direction. For concentrated samples, SANS and NMR spectroscopy under shear indicate that the new phase exhibits long range orientational order of nematic type.

In addition to this simple picture, strongly fluctuating behaviors have been reported in many semidilute and concentrated surfactant systems, including irregular time variations of the bulk rheological signals indicative of chaotic dynamics and fluctuations of the flow field, mainly localized in the high shear rate band. New insights recently emerged from the development of rheo-optical and velocimetry tools with improved spatial and temporal resolution. One-dimensional NMR and USV velocimetry measurements in the $(\mathbf{v}, \nabla v)$-plane have evidenced, on some well-known systems, that the position of the interface between bands exhibits periodic or erratic fluctuations as a function of time, correlated with the slip at the moving wall. Two-dimensional optical visualizations in the $(\mathbf{v}, \omega)$-plane of one particular

semidilute sample revealed that the interface between bands is unstable with respect to wave-vector in the vorticity direction. Interestingly, this behavior is associated with a time-dependent mechanical signature shared by a great number of semidilute and concentrated systems, suggesting that such interfacial instability is potentially common to different wormlike micellar systems.

Note that, in a more marginal way, vorticity structuring has also been observed in semidilute giant micelles showing a shear-thinning to shear-thickening transition. This particular spatial organization also presents a complex dynamics.

From a theoretical point of view, the shear-banded base flow is a consequence of a non-monotonic constitutive relation between the shear stress and the shear rate. Such a relation has been formulated by Cates using a microscopic approach more than 15 years ago [262]. Substantial advances in the understanding of the shear-banding transition have been realized using phenomenological models. Such models derived with inclusion of non-local (or spatial gradient) terms in the equation of motion of the viscoelastic stress lead to a unique stress plateau, independent of flow history. They also allow a more realistic description of the interface between bands, taking into account its finite width [234, 235, 252, 263–269]. In the framework of such models, other issues have been addressed, such as the impact of the flow geometry [252, 269] and its interplay with the boundary conditions [270] on the banding structure, the role of flow-concentration coupling [142, 143, 271], and the effect of the control parameter [143, 264, 271].

Recently, a strong effort has also been made to rationalize the complex time-dependent behaviors observed experimentally. Using the diffusive Johnson-Segalman (DJS) model, Fielding et al. demonstrated that a coupling between mechanical and structural variables such as the concentration or the micellar length can qualitatively reproduce the irregular time-variations of the stress (or shear rate) leading to rheochaos [225, 238]. Note that complex dynamics and rheochaos have also been predicted in phenomenological models of vorticity banding [272, 273].

The stability of the one-dimensional planar shear-banding flow has also been examined within the DJS model. The interface between bands is found to be unstable with respect to small perturbations with wave-vector in the plane made by the flow and the vorticity directions [223, 224, 274]. In the asymptotic state, the interface presents undulations along the velocity and vorticity directions. Jumps in normal stresses and shear rate across the interface are supposed to be the parameters driving the instability. The nonlinear analysis reveals a complex spatio temporal dynamics of the interface with a transition from traveling to rippling waves depending on the ratio between the thickness of the interface and the length of the cell [275].

For details on the theoretical state of the art and exhaustive bibliography, the reader is invited to refer to recent reviews on shear-banding [119, 120, 225].

To conclude, the shear-banding transition in wormlike micelles exhibits complex features beyond the basic one-dimensional scenario. The recent results brought a large amount of new information and also opened promising perspectives that will require strong experimental and theoretical efforts to elucidate fully the underlying mechanisms. The open issues concern, among other things, the organization of the induced structures in the semidilute case, the origin of the turbidity and

consequently of microscopic length scales in these systems, the role of wall slip in the complex dynamics, the effect of the cell geometry and boundary conditions, the microscopic origin of non-local terms, and the mechanisms driving the interfacial instability. Determination of the complete three-dimensional velocity profiles is also a very challenging but exciting task for the near future.

4 Nematic Phases of Wormlike Micelles

4.1 Introduction

At surfactant concentrations above 20–30 wt. %, wormlike micellar solutions undergo equilibrium transitions from an isotropic state to nematic and hexagonal liquid crystalline states. Nematic phases exhibit long-range orientational order with no positional order, whereas hexagonal phases show both orientational and translational long range orders of the centers of mass of the micelles. From their orientation and texture properties, these lyotropic phases bear strong similarities to thermotropic liquid crystals [276]. However, with lyotropics the concentration remains the control parameter for the transitions between the orientationally disordered and ordered states. The nematic phase is characterized by a non-zero order parameter noted S, which describes the orientation state of the director [276–278]:

$$S = \left\langle \frac{1}{2}\left(3\cos^2\psi - 1\right)\right\rangle \tag{5}$$

In Eq. 5, the brackets indicate the averaging over the orientational distribution function, and ψ is the angle between the orientation of a micelle and that of the director. The order parameter is zero in the isotropic phase and equals unity in the fully aligned state. In contrast to the isotropic state, nematic and hexagonal phases are birefringent. Observed by optical microscopy between crossed polarizers, solutions exhibit a strong static birefringence associated with Schlieren (nematic) and fan-like (hexagonal) textures.

Since the work by Lawson and Flaut on sodium decylsulfate/decanol/water (SdS/Dec) [279], numerous surfactant solutions were found to display long range orientational order at high concentrations [12, 16–18, 166, 172, 173, 197, 280–286]. From magnetic susceptibility measurements [287], two different nematic phases were evidenced. One phase, called N_C for *nematic calamitic*, was found to be made of rodlike aggregates, whereas the second phase, called N_D for *discostic nematic*, displayed disk-like aggregates. As shown by structural studies on SdS/Dec, the anisotropy ratio in the N_C phase was estimated to be around 3, yielding a micellar length around 10 nm [288, 289]. Interestingly, Porte and coworkers mentioned that the nematic phases could also be obtained with long and flexible aggregates, such as in the system cetylpyridinium chloride/hexanol/brine 0.2 M NaCl (CPCl/Hex) [12, 16]. There, for a fixed cosurfactant/surfactant ratio, the

nematic phase formed a small island located between large isotropic and hexagonal areas. Hexadecyltrimethylammonium bromide (C_{16}TAB) and sodium dodecylsulfate/decanol (SDS/Dec) were also shown to display nematic wormlike micelles. These phases were later investigated by rheology [166, 168, 172, 284, 290].

For semiflexible chains characterized by contour length much larger than persistence length, Semenov and Kokhlov demonstrated that the values of the phase boundaries between the isotropic and nematic states, as well as the order parameter of the nematic phase could be predicted [291]. Following Onsager [277], it was shown that the boundary c_{I-N} depends only on the ratio between the radius and the persistence length [277, 291, 292]. For nematic wormlike micelles, this limit was found to vary between 20 and 45 wt. %, in fair agreement with the theoretical values [44].

At still higher concentration, around 40 wt. %, hexagonal phases occur. In hexagonal phases, the surfactant aggregates are assumed to be very long and arranged according to a sixfold symmetry structure. The translational order confers to these phases a property that is not present in isotropic and nematic phases. Hexagonal phases are strong elastic gels, and as such possess a yield stress [112]. The rheology of hexagonal phases will not be presented in the present review. One reason is the relative low number of papers dealing with shear-induced instabilities and transitions in hexagonal phases. The second reason concerns the nature of the surfactant systems that were examined. These were on the one hand nonionic surfactants such as penta(ethylene glycol) monododecyl ether ($C_{12}E_5$) [293–297], and on the other microemulsions in which the cylinders are swollen with an apolar solvent [298–300]. In terms of size, charge, and microstructure, these systems are different from those discussed so far. Moreover, the rheology of their dilute or semidilute phases was not extensively addressed. We refer to the above citations for details.

4.2 Rheology

4.2.1 Steady-State

Figure 26 displays the shear rate dependence of the viscosity at the stationary state for a CPCl/Hex nematic sample at concentration $c = 36$ wt. % and at molar ratio $R = [\text{Hex}]/[\text{CPCl}] = 0.49$ [283, 301]. Up to a shear rate of $1\,\text{s}^{-1}$ in Fig. 26, $\eta(\dot{\gamma})$ exhibits a "Newtonian" plateau around 6 Pa s, followed by a shear-thinning regime. This shear-thinning behavior is representative for this class of materials [166, 284, 285, 290]. From the early surveys, it was noted that the viscosity of the nematic phase was lower than that of the isotropic solutions located below the transition concentration, a result which is in agreement with theory [41]. In Fig. 26, the shear-thinning behavior was found to be weaker than that of the isotropic solutions. In its asymptotic high shear rate range, the continuous line in Fig. 26 corresponds to a shear-thinning behavior of the form $\eta \sim \dot{\gamma}^{-0.73}$ [301].

4.2.2 Transients, Flow Reversals, and Scaling Laws

Shearing nematic surfactant solutions has revealed complex transient responses [172,283,284,301,302]. When submitted to a step shear rate, nematic samples usually exhibit a transient regime characterized by oscillations of the stress, this regime being followed by a stationary state. The viscosity data in Fig. 26 were obtained from these steady state stress values. The main results were obtained on CPCl/Hex [283,301,302], C_{16}TAB [172], and on SDS/Dec [284,290,303] nematics. They can be summarized as follows:

1. The transient regime depends on the history experienced by the solution prior to the actual measurement. The stationary stress on the contrary is history independent. A convenient way to control the sample history consists in applying a shearing to the sample for a time that is long enough. History controlled procedures made use of preshearing rate $\dot{\gamma}_{Presh}$.
2. The time needed to reach the stationary state, t_{st}, varies inversely with the shear rate, indicating that whatever $\dot{\gamma}$, steady state is reached after a constant deformation. For both CPCl/Hex and SDS/Dec this deformation was of the order of 300 strain units [284,301]. Nematic surfactant solutions of micelles can be considered to have forgotten their shear history after having been sheared for more than a few hundreds strain units.

The transient responses of nematic wormlike micelles were examined by Berret and coworkers as functions of $\dot{\gamma}$ and $\dot{\gamma}_{\mathrm{Presh}}$ in the "Newtonian" and shear-thinning

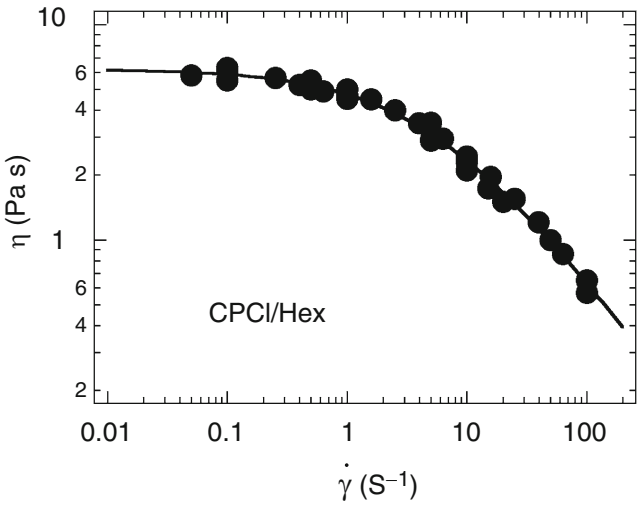

Fig. 26 Variation of the apparent shear viscosity $\eta = \sigma_{st}(\dot{\gamma})/\dot{\gamma}$ as a function of the shear rate for a solution of CPCl/Hex wormlike micelles in 0.2 M NaCl brine. The total concentration is $c = 36$ wt. % and the molar ratio [Hex]/[CPCl] = 0.49. The continuous line between the data points is a guide for the eyes. At high shear rates, the viscosity decreases according to a power law with exponent −0.73

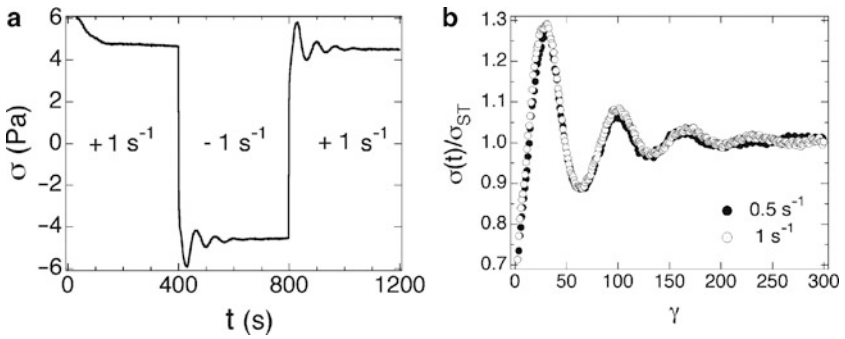

Fig. 27 (**a**) Shear stress response obtained from a flow reversal experiment in CPCl/Hex nematic wormlike micelles at total concentration $c = 37$ wt. % and molar ratio [Hex]/[CPCl]=0.49 [302]. In the flow reversal, the shear rate is changed stepwise from $+1\,s^{-1}$ (after sample loading) to -1 s^{-1} and then to $+1\,s^{-1}$. (**b**) Variation of the normalized shear stress $\sigma(t)/\sigma_{st}$ as a function of the total applied deformation for the same solution. Flow reversal experiments were carried out at $\dot{\gamma} = 0.5\,s^{-1}$ (*close circles*) and $1\,s^{-1}$ (*open circles*) and were found to be superimposed

regimes. In this context, flow reversal [302] and step shear rate [283] experiments were evaluated. In a flow reversal, the sample is first presheared at fixed rate $\dot{\gamma}_{Presh} = \dot{\gamma}_0$ until the steady state condition are reached. The direction of the shear flow is then switched abruptly from $+\dot{\gamma}_0$ to $-\dot{\gamma}_0$. In step shear rate experiments, only the amplitude of the shearing is changed, not the sense of rotation. Raw data of two consecutive flow reversals obtained on CPCl/Hex nematic solutions ($c = 37$ wt. % and [Hex]/[CPCl]=0.49) are displayed as a function of time in Fig. 27a ($\dot{\gamma}_0 = 1s^{-1}$). Upon flow inception, for a freshly loaded sample, the shear stress exhibited a large overshoot, then decreasing monotonously toward its stationary value. After reversing the flow direction, damped oscillations were observed in the stress responses, either in the negative or in the positive torque ranges. Similar oscillations were found in step shear rates [283].

The approach consisting of preshearing the solutions was actually inspired from the research on liquid crystalline polymers (LCP) [304, 305]. LCPs have attracted much attention during the past few decades because of their remarkable flow and mechanical properties. In LCPs, the competition between the local molecular relaxation of the polymers and the structure and orientations predicted by classical nematodynamics results in a very complex rheology, for which only mesoscopic theories exist [306]. It is out the scope of the present review to enter into the details of the mesoscopic approaches developed for LCPs, and the reader should refer to the seminal papers by Larson and Doi [306] and Srinivasarao [307]. The first experimental evidence of damped oscillations in the transient shear stress was due to Moldenaers et al. on poly(benzyl-L-glutamate solutions) (PBLG) of high molecular weights [305]. PBLG is a lyotropic liquid crystal, where nematogens arise from the hydrogen bonding helix conformation of the backbone. The stress oscillations were related by Larson and Doi to the tumbling instability of the nematic director in the flow [305]. A major property of the constitutive equations derived by Larson and

Doi was their scaling behavior. The model predicted that the time evolution of the shear stress is a function of only two parameters, the strain $\dot{\gamma}t$ applied to the sample and the ratio $\dot{\gamma}/\dot{\gamma}_{Presh}$ [306, 308], i.e.:

$$\frac{\sigma(t,\dot{\gamma},\dot{\gamma}_{\rm Presh})}{\sigma_{\rm st}} = F\left(\dot{\gamma}t, \frac{\dot{\gamma}}{\dot{\gamma}_{\rm Presh}}\right), \tag{6}$$

where $\dot{\gamma}/\dot{\gamma}_{\rm Presh} = -1$ for flow reversals.

Figure 27b displays the results of flow reversals obtained at two different shear rates ($\dot{\gamma} = 0.5$ and $\dot{\gamma} = 1\ s^{-1}$), where, to obey Eq. 6, the stress has been divided by the stationary value, and the time replaced by the deformation. The data at 0.5 and $1\ s^{-1}$ are found to be superimposed, demonstrating the scaling of the stress responses. Scaling laws were also obtained with nematic calamitic and discotic phases of SDS/Dec, although, with more complex patterns [284, 290, 309]. It is important to realize that the mechanical responses in Fig. 27 are very different from those of the isotropic phases, for which the scaling with deformation or the dependence on the shear history have not been observed [138].

As for CPCl/Hex, the conclusions are twofold:

1. Although polymers and wormlike micelles are very different in nature, the flow properties of their nematic phases are similar. This property was ascribed to the existence of textures at a mesoscopic scale, and to the fact that the dynamics of the textures dominate the mechanical responses of these fluids [310].
2. One of these similarities concerns the possibility for the nematic director to tumble in the flow. This tumbling is associated with the periodic oscillations of the stress, as seen in Fig. 27.

For tumbling nematics, the director is assumed to find no preferred orientation and hence to rotate indefinitely in the flow. Tumbling conditions are met for Ericksen numbers larger than a critical value of about 10 (the Ericksen number is defined as the ratio between the viscous and elastic torques) [311].

A second requirement for this instability to occur is that the two Leslie viscosity coefficients α_2 and α_3 are of opposite signs [276, 312]. If the ratio between the two viscosities is positive, the director exhibits different dynamics: it aligns with respect to the velocity at an angle θ_0 such that $\tan^2(\theta_0) = \alpha_2/\alpha_3$. Note finally that, despite a complex microstructure, the classification in terms of flow-aligning and tumbling nematics, as defined for low molecular weight liquid-crystals, still applied to lyotropic systems.

4.3 Textures and Microscopy

A great amount of experimental data using optical microscopy has shown the existence of textures in thermotropic, as well as in lyotropic liquid crystals [304, 313, 314]. These textures are in the micrometer range and are interpreted in terms of

spatial variations of the nematic director through the sample. At rest, the textures translate into a polydomain structure where the distribution of nematic directors remains constant within each domain. Few optical data have been gathered on surfactant nematics however. For the calamitic phase at rest, Schlieren textures with characteristic line and point defects were observed in various systems [12,15,16,172,284,288,301]. As samples were allowed to relax for some hours, the Schlieren textures coarsened and an alignment resulted due to the interactions with the glass surfaces of the cell.

Under shear, texture refinement was predicted, and observed for LCPs as resulting from the competition between the viscoelastic and the elastic Frank stresses. Here, the Frank stresses arise from the orientational heterogeneities of the director occurring at the transitions or walls from domain to domain. The balance between the elastic and viscous energy density allowed Marrucci to show that the texture lengths should decrease with the shear rate as $\dot{\gamma}^{-1/2}$. Roux et al. have performed rheo-optical measurements on CPCl/Hex nematics in order to assess these predictions [301]. At low shear rates, striped textures parallel to the flow could be identified. The texture lengths were estimated to be of the order of 5–10 µm, depending on the applied rate. A refinement of the stripes was also observed with increasing shear rate, but not estimated quantitatively. Stop-flow experiments on the same system were also carried out and allowed to confirm the predictions of the mesoscopic domain theory [306]. At the cessation of the flow, dark and bright stripes perpendicular to the flow velocity were found, with a band spacing growing as $\sim t^{1/2}$. Similar results were observed in LCPs [314]. In conclusion of this section, the rheo-optical data confirm a polydomain structure, the coupling of the textures to the flow, and the close analogy with liquid crystalline polymers.

4.4 Director Orientations Under Shear: Scattering and NMR

Small-angle neutron and X-ray scattering were undertaken in order to retrieve the local orientation of the micellar threads at rest and under shear. As shown on thermotropic [278] and lyotropic [12, 16, 288, 289] liquid crystals at rest, these two techniques provide unambiguous signatures of nematic long-range orientational order through the generation of a diffuse scattering patterns. For experiments at rest, the alignment of the nematic director was achieved using an externally applied magnetic field.

Under shear, Couette or cone-and-plate cells specifically designed for small-angle scattering [56, 315] were used at large scale facilities by many authors. With the help of two-dimensional detectors, the anisotropy in the forward scattering was targeted. This combined configuration of shearing and detection allowed one to observe the scattering in the three planes of the reciprocal space, ($\mathbf{q}_v$,$\mathbf{q}_{\nabla v}$), ($\mathbf{q}_v$,$\mathbf{q}_\omega$), and ($\mathbf{q}_{\nabla v}$,$\mathbf{q}_\omega$), where we recall that $\mathbf{q}_v$, $\mathbf{q}_{\nabla v}$, and $\mathbf{q}_\omega$ are the wavevectors parallel to the velocity, velocity gradient, and vorticity. Most of the data on nematic wormlike micelles were collected in the ($\mathbf{q}_v$,$\mathbf{q}_\omega$)- and ($\mathbf{q}_v$,$\mathbf{q}_{\nabla v}$)-planes

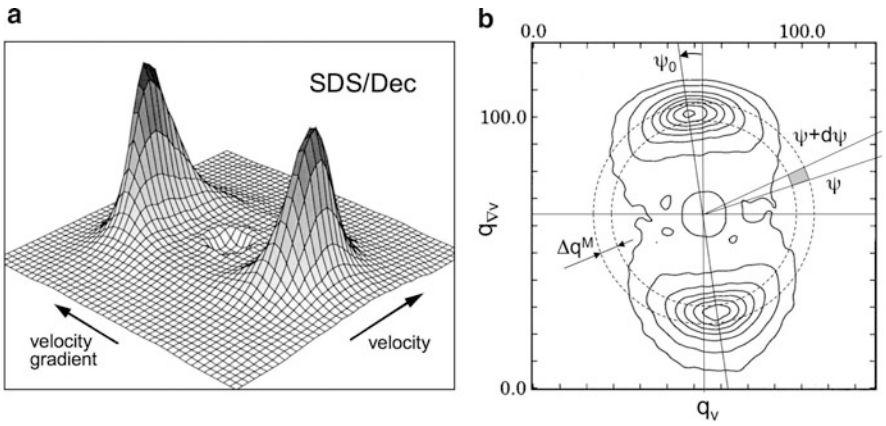

Fig. 28 (**a**) 3D-plot of the neutron scattering cross-section measured in the $(\mathbf{q}_v, \mathbf{q}_{\nabla v})$-vorticity plane for the SDS–Dec nematic calamitic phase. The SDS/Dec solution was prepared in D_2O for contrast reasons at total concentration $c = 29.5$ wt. % and molar ratio [Dec]/[SDS] = 0.33 [317]. The shear rate of the experiment was $\dot{\gamma} = 50\ s^{-1}$. (**b**) Iso-intensity contours obtained for the same conditions as in (**a**). Along the $\mathbf{q}_v$- and $\mathbf{q}_{\nabla v}$-axis, the wave-vector ranges from -0.16 to $+0.16\ Å^{-1}$. The *dashed circles* set the limits of the domain of integration for the data treatment (see text)

[33, 168, 172, 173, 301–303, 316]. Figure 28a displays a typical three-dimensional plot of the neutron intensity scattered by a nematic lyotropic solution in the $(\mathbf{q}_v,\mathbf{q}_{\nabla v})$-plane. The data were obtained on the SDS/Dec calamitic phase at $50\ s^{-1}$ (concentration $c = 29.5$ wt. % and $R = [\text{Dec}]/[\text{SDS}] = 0.33$). As shown in the iso-intensity contour plot (Fig. 28b), the patterns are characterized by two crescent-like peaks aside from the velocity axis. The maximum scattering corresponds to the first order of the structure factor, from which the distance between the center-of-mass of the micelles can be estimated (here 6 nm for a radius of $\sim$2 nm). The modulation of the azimuthal intensity is also of interest since it reflects the distribution of micellar orientations. The spectra were analyzed in terms of angular distribution of the scattered intensity. The scattering was integrated over an elementary surface $\mathrm{d}q_v\,\mathrm{d}q_{\nabla v} = q^{\mathrm{M}}\Delta q^{\mathrm{M}}\Delta\psi$, where Δq^{M} corresponds typically to the half width at half maximum of the peak. Plotted as a function of the azimuthal angle ψ, two parameters could be retrieved:

- The order parameter S of the nematic phase under shear (Eq. 5). The analytical technique to transform the azimuthal intensity into an orientational distribution has been quoted in several papers [109, 276, 278].
- The tilt angle ψ_0 of the scattering pattern with respect to the vertical axis. It was shown that the tilt angle angle ψ_0 was actually the orientation angle between the nematic director and the flow. By symmetry, it is zero in the $(\mathbf{q}_v,\mathbf{q}_\omega)$-plane, nonzero in $(\mathbf{q}_v,\mathbf{q}_{\nabla v})$-plane [290, 318], and changes sign by flow reversal [317].

In Fig. 29, the order parameter $S^{v,\omega}$ is shown as a function of the shear rate, together with characteristic SANS spectra obtained on CPCl/Hex nematic solution.

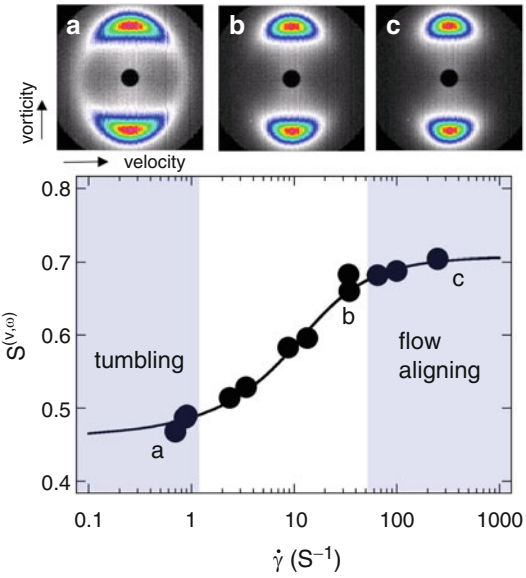

Fig. 29 *Upper panels*: Neutron scattering intensities obtained from a CPCl/Hex nematic micellar solution in the $(\mathbf{q}_v, \mathbf{q}_{\nabla v})$-plane at different shear rates: (**a**) $\dot{\gamma} = 0.94\ s^{-1}$, (**b**) $\dot{\gamma} = 34.5\ s^{-1}$, and (**c**) $\dot{\gamma} = 250\ s^{-1}$. The nematic phase was made in deuterated water at concentration $c = 35.2$ wt. % and molar ratio [Hex]/[CPCl] = 0.49 [301]. *Lower panel*: Shear rate dependence of the orientational order parameter $S^{v,\omega}$ (Eq. 5) obtained from the SANS cross-sections shown in the *upper panel*. The *continuous line* is a guide for the eyes. The increase of the order parameter was interpreted in terms of a transition between the tumbling and the flow-alignment regimes [290, 303]

It illustrates that shear orients the nematic phase steadily and that this process is concomitant to the shear-thinning behavior (Fig. 26). As recognized by Burghardt and coworkers [290, 303], bulk measurements of S reflect the distribution of micellar orientations around the local director as well as the distribution of director orientations in the polydomain sample. The progressive increase from $S^{v,\omega} = 0.45$ to $S^{v,\omega} = 0.70$ in Fig. 29 was ascribed to the transition between the polydomain tumbling regime toward the flow-alignment monodomain regime [290, 301, 303]. Using synchroton X-ray radiation, Caputo et al. reported the time dependence of the order parameter $S^{v,\nabla v}$ in the $(\mathbf{q}_v, \mathbf{q}_{\nabla v})$-plane [290, 303]. SAXS spectra were collected every second during step shear rate and flow reversal testing. It was shown by these authors that the orientational response of CPCl/Hex nematics was consistent with the Doi–Larson model developed for the LCPs, i.e. that the order parameter decreased after reversing the flow, a result that was not seen on classical LCPs.

The second surfactant nematics that was studied thoroughly, SDS/Dec, shows a different behavior. Although it is a textured material with a bulk shear-thinning rheology similar to CPCl/Hex or C_{16}TAB, this system exhibits what appears to be common characteristics of aligning nematics: (i) a constant orientation state and order parameter in steady shear, (ii) a single undershoot of long duration in average orientation upon flow reversal, and (iii) no significant orientation change upon step increase or decrease in shear rate or upon flow cessation [284, 290, 309, 317].

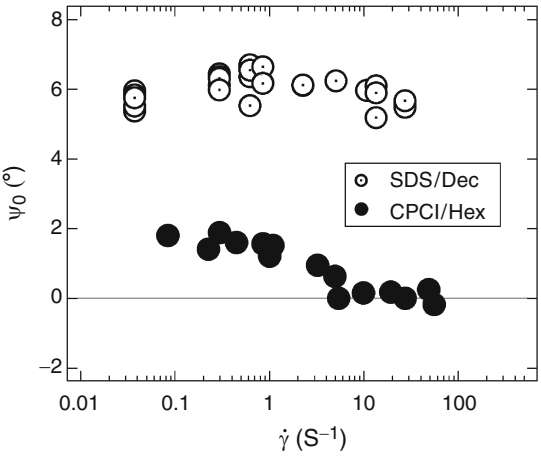

Fig. 30 Evolution of the orientation angle ψ_0 as a function of the shear rate for the SDS/Dec and CPCl/Hex nematics. Samples characteristics are those of Fig. 28 [317]

Caputo et al. concluded that this system followed the polydomain model predictions of transient orientation for aligning nematics [290]. As an illustration, Fig. 30 displays the evolution of the orientation angle ψ_0 as a function of the shear rate for both SDS/Dec and for CPCl/Hex [317]. For SDS/Dec, the orientation of the director with respect to the velocity remains unchanged at $\psi_0 = 6^\circ$ over three decades in shear rates. For the tumbling nematic micelles, the tilt angle has a nonzero value at low shear rates, $\psi_0 = 1.8^\circ$, but decreases to zero with increasing shear rates. The shear rates at which ψ_0 deviates from its low shear rate value corresponds to the upper limit of the tumbling regime. As the system enters into the flow alignment regime, the orientation angle ψ_0 decreases to zero, yielding a fully symmetric scattering pattern. These results are in qualitative agreement with those obtained on tumbling LCPs by flow birefringence [319].

Using ^{2}H NMR-spectroscopy under shear, the flow-aligning properties of SDS/Dec calamitic phase prepared in D_2O could be confirmed. In this experiment, the anisotropic motions of the D_2O molecules in contact with the micellar surfaces result in a small residual quadrupole coupling, which is related to the angle between the nematic director and the magnetic field [320]. The line splitting $\Delta\nu$ corresponding to this coupling is given by $\Delta\nu$=3/4 $\delta(3\cos^2\theta - 1)$ where δ is the quadrupole coupling constant. In the configuration adopted, the magnetic field was parallel to the velocity gradient, i.e. $\theta = \pi/2 - \psi$, where ψ is the tilt angle defined in Fig. 28b. Figure 31a illustrates a series of spectra obtained for the nematic calamitic sample at $\dot{\gamma} = 0.32\ s^{-1}$ and at different deformations γ after inception of shear. With increasing deformation, a decrease of the splitting is first observed. At $\gamma \sim 1.4$, the two resonance lines overlap at the magic angle ($\theta = 54.7^\circ$). When the deformation is further increased, the splitting stabilizes at the steady state value, which is slightly lower than half of the initial splitting. Beyond $\gamma = 15$, no change is observed, neither in the splitting nor in the line shape. The strain evolution in Fig. 31b shows an increase and a saturation at θ_0 = 78 $\pm$ 2°. This result is again a strong indication that the SDS/Dec nematic is flow-aligning. The flow-alignment behavior can be checked by

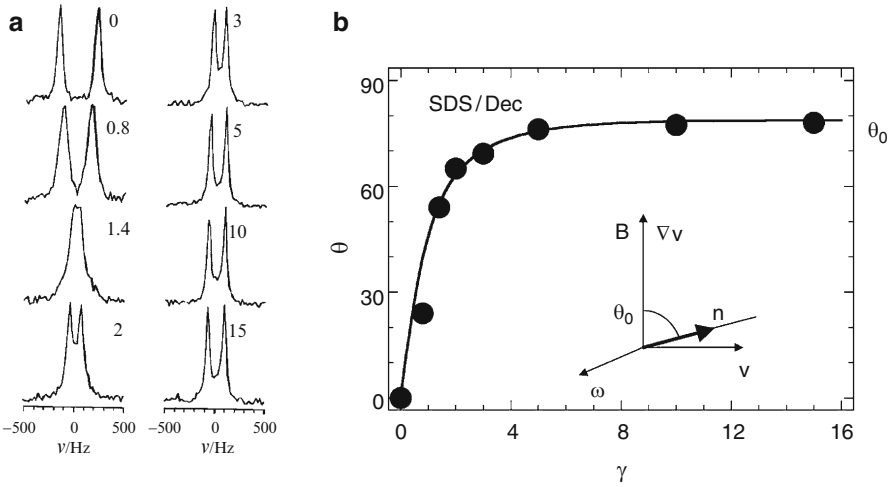

Fig. 31 (**a**) Transient behavior of the NMR splitting for an SDS/Dec nematic calamitic solution at concentration $c = 29.5$ wt. % and molar ratio [Dec]/[SDS] = 0.33 and sheared at $\dot{\gamma} = 0.32\,\mathrm{s}^{-1}$ [284]. (**b**) Evolution of the orientation angle of the nematic director with respect to the magnetic field as function of the strain. The symbols correspond to the spectra in (**a**), and the continuous line is determined from Eq. 7, yielding an asymptotic angle of $\theta_0 = 78 \pm 2°$. *Inset*: Orientation of the nematic director in presence of the flow and of the magnetic field

comparing the director orientation as a function of strain, $\theta(\dot{\gamma})$ as predicted by the Leslie–Ericksen continuum theory [112, 276]. Neglecting the effect of the magnetic field [321], the evolution of the director angle reads

$$\theta(\gamma) = \arctan\left[\sqrt{\frac{\alpha_2}{\alpha_3}}\tanh\left(\frac{\sqrt{\alpha_2\alpha_3}}{\alpha_3 - \alpha_2}\gamma\right)\right] \quad \text{with} \quad \alpha_2, \alpha_3 < 0 \tag{7}$$

where α_2 and α_3 are Leslie coefficients. The continuous line in Fig. 31b has been calculated using Eq. 7 with $\alpha_2/\alpha_3 = \tan^2(\theta_0) = 25$ as unique fitting parameter. The good agreement between the experimental and the calculated $\theta(\gamma)$ is a further indication of the flow-alignment character of the N_C phase. For a tumbling system a more complex transient evolution of the director orientation is expected, and was indeed observed for the tumbling PBLG [297].

4.5 Conclusion

Using scattering and spectroscopy experiments, it has been shown that the physical quantities characterizing the wormlike micellar nematics such as the order parameter, Leslie viscosities ratio, or alignment angles can be determined. The main result of this section is the analogy between the wormlike micelles and the liquid-crystalline polymers, as far as their nematic states are concerned. Because these

fluids are textured, their rheology is unique. This rheology is determined by the coupling between the spatial heterogeneities in the nematic director and the flow. Another interesting result concerns the evidence of the director tumbling instability found for CPCl/Hex or C_{16}TAB nematics. For a better description of these systems under shear, additional experiments should be performed, such as those on the texture dynamics, and on the measurements of the Franck (elastic) and Leslie (viscosity) coefficients.

5 Summary

In this review, we provided an overview of the nonlinear rheology of surfactant wormlike micelles, from dilute to liquid crystal states. The equilibrium phase diagram of these systems is extremely rich. We showed that this leads, under steady shear flow, to different rheological signatures such as shear-thickening, shear-thinning or a combination of the two. These nonlinear behaviors are associated with strong modifications both of the flow field and of the internal structure of the fluid. The dilute phases of wormlike micelles thicken under shear due to the growth of a viscous shear-induced structure. The semidilute and concentrated phases of giant micelles undergo a shear-banding transition, where phases of different fluidities, spatially organized, coexist. Finally, nematic phases of micelles present a tumbling instability of the director. All these transitions and instabilities share a common feature: they are characterized by extremely long transients compared to the intrinsic relaxation time of the system. These specific behaviors are related to rearrangements of the internal structure at the mesoscopic scale. Another crucial point that emerged from recent experiments is that these transitions result in a complex spatiotemporal dynamics of the flow, involving either bulk or interfacial instabilities, the driving parameters of which remain to determine.

Besides their practical interest in today's life, giant micelles are attractive, notably because of the accurate knowledge of their phase behavior and dynamical properties, the simplicity of their linear response, and their analogy with conventional polymers. The major interest comes from the large diversity of their flow behaviors that continue to fascinate lots of experimentalists and theoreticians, especially because they are representative of many phenomena encountered in other complex fluids.

Acknowledgements The present review would not have been possible without the extended network of colleagues and friends being, as we are, fascinated by this subject. It is a pleasure to acknowledge the collaborations and the fruitful discussions we had over the years with Jacqueline Appell, Wesley Burghardt, Olivier Cardoso, Jean-Louis Counord, Jean-Paul Decruppe, Marc-Antoine Fardin, Olivier Greffier, Guillaume Grégoire, Heinz Hoffmann, Sébastien Manneville, François Molino, Julian Oberdisse, Peter Olmsted, Grégoire Porte, Ovidiu Radulescu, Jean-Baptiste Salmon, Claudia Schmidt, Jean-François Tassin, and Lynn Walker. The Laboratoire Léon Brillouin (CEA, Saclay, France), the Institute Laue-Langevin, and the European Synchrotron Radiation Facilities (Grenoble, France) are also acknowledged for their technical and financial supports. We have also benefited from research organizations and fundings, such as the GDR

1081 “Rhéophysique des Colloides et Suspensions”, European TMR-Network “Rheology of Liquid Crystals” contract number FMRX-CT96-0003 (DG 12 - ORGS), Agence Nationale pour la Recherche (ANR JCJC-0020). We are finally very grateful to Sébastien Manneville for his comments on the first version of the manuscript.

References

1. Debye P, Anacker E (1951) Micelle shape from dissymetry measurements. J Phys Chem 55:644–655
2. Nash T (1958) The interaction of some naphtalene derivatives with a cationic soap below the critical micelle concentration. J Colloid Sci 13:134–139
3. Gravsholt S (1976) Viscoelasticity in highly dilute aqueous solutions of pure cationic detergents. J Colloid Interface Sci 57:575–577
4. Porte G, Appell J, Poggi Y (1980) Experimental investigations on the flexibility of elongated cetylpyridinium bromide micelles. J Phys Chem 84:3105–3110
5. Porte G, Appell J (1981) Growth and size distributions of cetylpyridinium bromide micelles in high ionic strength aqueous solutions. J Phys Chem 85:2511–2519
6. Ikeda S (1984) Sphere-rod transition of surfactant micelles and size distribution of rodlike micelles. J Phys Chem 88:2144–2149
7. Candau S, Hirsch E, Zana R (1985) Light scattering investigations of the behavior of semidilute aqueous micellar solutions of cetyltrimethylammonium bromide: analogy with semidilute polymer solutions. J Colloid Interface Sci 105:521–528
8. Imae T, Kamiya R, Ikeda S (1984) Electron microscopic observation of rodlike micelles of dimethyloleylamine oxide regenerated from its aqueous solutions. J Colloid Interface Sci 99(1):300–301
9. Imae T, Kamiya R, Ikeda S (1985) Formation of spherical and rodlike micelles of cetyltrimethylammonium bromide in aqueous nabr solutions. J Colloid Interface Sci 108(1):215–225
10. Imae T, Ikeda S (1986) Sphere-rod transition in micelles of tetradecyltrimethylammonium halides in aqueous sodium halide solutions and flexibility and entanglement of long rodlike micelles. J Phys Chem 90(1):5216–5223
11. Porte G, Poggi Y, Appell J, Maret G (1984) Large micelles in concentrated solutions. The second critical micellar concentration. J Phys Chem 88:5713–5720
12. Porte G, Gomati R, Elhaitamy O, Appell J, Marignan J (1986) Morphological transformations of the primary surfactant structures in brine-rich mixtures of ternary-systems (surfactant alcohol brine). J Phys Chem 90(22):5746–5751
13. Candau S, Hirsch E, Zana R (1984) New aspects of the behaviour of alkyltrimethylammonium bromide micelles: light scattering and viscometric studies. J Phys 45:1263–1270
14. Candau S, Hirsch E, Zana R, Adam M (1988) Network properties of semidilute kbr solutions of cetyltrimetylammonium bromide. J Colloid Interface Sci 122:430–440
15. Amaral L, Helene M, Bittencourt D, Itri R (1987) New nematic lyomesophase of sodium dodecyl sulfate. J Phys Chem 91:5949–5953
16. Gomati R, Appell J, Bassereau P, Marignan J, Porte G (1987) Influence of the nature of the counterion and of hexanol on the phase behavior of the dilute ternary systems: cetylpyridinium bromide or chloride-hexanol-brine. J Phys Chem 91:6203–6210
17. Amaral L, Helene MM (1988) Nematic domain in the sodium lauryl sulfate/water/decanol system. J Phys Chem 92:6094–6098
18. Hertel G, Hoffmann H (1988) Lyotropic nematic phases of double chain surfactants. Trends Colloid Interface Sci 4:123–131
19. Hoffmann H, Löbl H, Rehage H, Wunderlich I (1985) Rheology of surfactant solutions. Tenside Detergents 22:290–298

20. Shikata T, Hirata K, Kotaka T (1987) Micelle formation of detergent molecules in aqueous media. 1. viscoelastic properties of aqueous cetyltrimethylammonium bromide solutions. Langmuir 3:1081–1086
21. Rehage H, Hoffmann H (1988a) Rheological properties of viscoelastic surfactant systems. J Phys Chem 92:4712–4719
22. Shikata T, Hirata K, Kotaka T (1988b) Micelle formation of detergent molecules in aqueous media. 2. role of free salicylate ions on viscoelastic properties of aqueous cetyltrimethylammonium bromide-sodium salicylate solutions. Langmuir 4:354–359
23. Shikata T, Hirata H, Takatori E, Osaki K (1988a) Nonlinear viscoelastic behavior of aqueous detergent solutions. J Non-Newt Fluid Mech 28(2):171–182
24. Shikata T, Hirata K, Kotaka T (1989) Micelle formation of detergent molecules in aqueous media. 3. viscoelastic properties of aqueous cetyltrimethylammonium bromide-salicylic acid solutions. Langmuir 5:398–405
25. Cates ME, Candau SJ (1990) Statics and dynamics of wormlike surfactant micelles. J Phys Cond Matt 2(33):6869–6892
26. Shikata T, Hirata K, Kotaka T (1990) Micelle formation of detergent molecules in aqueous media. 4. electrostatic features and phase behavior of cetyltrimethylammonium bromide:salicylic acid micellar solutions. J Phys Chem 94:3702–3706
27. Kern F, Zana R, Candau SJ (1991) Rheological properties of semidilute and concentrated aqueous-solutions of cetyltrimethylammonium chloride in the presence of sodium-salicylate and sodium-chloride. Langmuir 7(7):1344–1351
28. Rehage H, Hoffmann H (1991) Viscoelastic surfactant solutions – model systems for rheological research. Mol Phys 74(5):933–973
29. Clausen TM, Vinson PK, Minter JR, Davis HT, Talmon Y, Miller WG (1992) Viscoelastic micellar solutions – microscopy and rheology. J Phys Chem 96(1):474–484
30. Khatory A, Lequeux F, Kern F, Candau SJ (1993b) Linear and nonlinear viscoelasticity of semidilute solutions of wormlike micelles at high-salt content. Langmuir 9(6):1456–1464
31. Khatory A, Kern F, Lequeux F, Appell J, Porte G, Morie N, Ott A, Urbach W (1993a) Entangled versus multiconnected network of wormlike micelles. Langmuir 9(4):933–939
32. Berret JF, Appell J, Porte G (1993) Linear rheology of entangled wormlike micelles. Langmuir 9(11):2851–2854
33. Berret JF, Roux DC, Porte G (1994a) Isotropic-to-nematic transition in wormlike micelles under shear. J Phys II (France) 4(8):1261–1279
34. Smolka LB, Belmonte A (2003) Drop pinch-off and filament dynamics of wormlike micellar fluids. J Non-Newt Fluid Mech 115(1):1–25
35. Bellour M, Skouri M, Munch JP, Hébraud P (2002) Brownian motion of particles embedded in a solution of giant micelles. Eur Phys J E 8:431–436
36. Buchanan M, Atakhorrami M, Palierne JF, MacKintosh FC, Schmidt CF (2005) High-frequency microrheology of wormlike micelles. Phys Rev E 72(1):011,504
37. Willenbacher N, Oelschlaeger C, Schopferer M, Fischer P, Cardinaux F, Scheffold F (2007) Broad bandwidth optical and mechanical rheometry of wormlike micelle solutions. Phys Rev Lett 99(6):068,302
38. Cappallo N, Lapointe C, Reich DH, Leheny RL (2007) Nonlinear microrheology of wormlike micelle solutions using ferromagnetic nanowire probes. Phys Rev E 76(3)
39. Raudsepp A, Callaghan P, Hemar Y (2008) A study of the nonlinear rheology of complex fluids using diffusing wave spectroscopy. J Rheol 52(5):1113–1129
40. Cates ME (1988) Dynamics of living polymers and flexible surfactant micelles – scaling laws for dilution. J Phys 49(9):1593–1600
41. Doi M, Edwards S (1986) The theory of polymer dynamics. Oxford, Clarendon
42. Lequeux F, Candau S (1994) Dynamical properties of wormlike micelles. In: Herb C, Prud'homme R (eds) Structure and flow in surfactant solutions. ACS Symposium Series 578. American Chemical Society, Washington, DC, pp 51–62
43. Walker LM (2001) Rheology and structure of wormlike micelles. Curr Opin Colloid Inter Sci 6(5–6):451–456

44. Berret JF (2005) Rheology of wormlike micelles: equilibrium properties and shear-banding transition. In: Molecular gels, Elsevier, Dordrecht
45. Prudhomme RK, Warr GG (1994) Elongational flow of solutions of rodlike micelles. Langmuir 10(10):3419–3426
46. Walker LM, Moldenaers P, Berret JF (1996) Macroscopic response of wormlike micelles to elongational flow. Langmuir 12(26):6309–6314
47. Chen CM, Warr GG (1997) Light scattering from wormlike micelles in an elongational field. Langmuir 13(6):1374–1376
48. Rothstein JP (2003) Transient extensional rheology of wormlike micelle solutions. J Rheol 47(5):1227–1247
49. Yesilata B, Clasen C, McKinley GH (2006) Nonlinear shear and extensional flow dynamics of wormlike surfactant solutions. J Non-Newt Fluid Mech 133(2–3):73–90
50. Andereck D, Liu S, Swinney H (1986) Flow regimes in a circular Couette system with independently rotating cylinders. J Fluid Mech 164:155–183
51. Rehage H, Hoffmann H (1982) Shear induced phase transitions in highly dilute aqueous detergent solutions. Rheol Acta 21:561–563
52. Hoffmann H, Platz G, Rehage H, Schorr W, Ulbricht W (1981b) Viskoelastische tensidlösungen. Ber Bunsenges Phys Chem 85:255–266
53. Shenoy A (1984) A review on drag reduction with special reference to micellar systems. Colloid Polym Sci 262:319–337
54. Bewersdorff HW, Frings B, Lindner P, Oberthür RC (1986) The conformation of drag reducing micelles from small-angle-neutron-scattering experiments. Rheol Acta 25(6):642–646
55. Ohlendorf D, Interthal W, Hoffmann H (1986) Surfactant systems for drag reduction: physicochemical properties and rheological behaviour. Rheol Acta 25(5):468–486
56. Lindner P, Bewersdorff H, Heen R, Sittart P, Thiel H, Langowski J, Oberthür R (1990) Drag-reducing surfactant solutions in laminar and turbulent flow investigated by small-angle neutron scattering and light scattering. Trends Colloid Interface Sci 4:107–112
57. Boltenhagen P, Hu YT, Matthys EF, Pine DJ (1997b) Observation of bulk phase separation and coexistence in a sheared micellar solution. Phys Rev Lett 79(12):2359–2362
58. Sung K, Han MS, Kim C (2003) Rheological behavior and wall slip of dilute and semidilute CPyCl/NaSal surfactant solutions. Korea-Australia Rheol J 15(3):151–156
59. Wunderlich I, Hoffmann H, Rehage H (1987) Flow birefringence and rheological measurements on shear induced micellar structures. Rheol Acta 26(6):532–542
60. Koch S, Schneider T, Küter W (1998) The velocity field of dilute cationic surfactant solutions in a couette-viscometer. J Non-Newtonian Fluid Mech 78(1):47–59
61. Dehmoune J, Decruppe J, Greffier O, Xu H (2007) Rheometric and rheo-optical investigation on the effect of the aliphatic chain length of the surfactant on the shear thickening of dilute wormlike micellar solutions. Rheol Acta 46(8):1121–1129
62. Wunderlich A, Brunn P (1989) The complex rheological behavior of an aqueous cationic surfactant solution investigated in a couette-type viscosimeter. Colloid Polym Sci 267:627–636
63. Hu YT, Wang SQ, Jamieson AM (1993b) Rheological and flow birefringence studies of a shear-thickening complex fluid – a surfactant model system. J Rheol 37(3):531–546
64. Liu CH, Pine DJ (1996) Shear-induced gelation and fracture in micellar solutions. Phys Rev Lett 77(10):2121–2124
65. Vasudevan M, Shen A, Khomami B, Sureshkumar R (2008) Self-similar shear thickening behavior in ctab/nasal surfactant solutions. J Rheol 52(2):527–550
66. Cressely R, Hartmann V (1998) Rheological behaviour and shear thickening exhibited by aqueous ctab micellar solutions. Eur Phys J B 6(1):57–62
67. Hartmann V, Cressely R (1998) Occurrence of shear thickening in aqueous micellar solutions of CTAB with some added organic counterions. Colloid Polym Sci 276(2):169–175
68. Hartmann V, Cressely R (1997b) Simple salts effects on the characteristics of the shear thickening exhibited by an aqueous micellar solution of CTAT/NaSal. Europhys Lett 40:691–696
69. Rose GD, Foster KL (1989) Drag reduction and rheological properties of cationic viscoelastic surfactant formulations. J Non-Newt Fluid Mech 31(1):59–85

70. Hu Y, Rajaram CV, Wang SQ, Jamieson AM (1994) Shear thickening behavior of a rheopectic micellar solution – salt effects. Langmuir 10(1):80–85
71. Hartmann V, Cressely R (1997a) Shear-thickening of an aqueous micellar solution of cetyltrimethylammonium bromide and sodium tosylate. J Phys II France 7:1087–1098
72. Kim WJ, Yang SM (2000) Effects of sodium salicylate on the microstructure of an aqueous micellar solution and its rheological responses. J Colloid Interface Sci 232(2):225–234
73. Kim WJ, Yang SM (2001) Flow-induced microstructure in aqueous cationic surfactant solution in the presence of structure-enhancing additives. J Chem Eng Jpn 34(2):227–231
74. Hu H, Larson RG, Magda JJ (2002) Measurement of wall-slip-layer rheology in shear-thickening wormy micelle solutions. J Rheol 46(4):1001–1021
75. Gamez-Corrales R, Berret JF, Walker L, Oberdisse J (1999) Shear-thickening dilute surfactant solutions: the equilibrium structure as studied by small-angle neutron scattering. Langmuir 15:6755–6763
76. Truong M, Walker L (2002) Quantifying the importance of micellar microstructure and electrostatic interactions on the shear-induced structural transition of cylindrical micelles. Langmuir 18(6):2024–2031
77. Berret JF, Lerouge S, Decruppe J (2002) Kinetics of the shear-thickening transition observed in dilute surfactant solutions and investigated by flow birefringence. Langmuir 18:7279–7286
78. Berret JF, Gamez-Corrales R, Lerouge S, Decruppe J (2000a) Shear-thickening transition in surfactant solutions: new experimental features from rheology and flow birefringence. Eur Phys J E 2:343–350
79. Berret JF, Gamez-Corrales R, Séréro Y, Molino F, Lindner P (2001) Shear-induced micellar growth in dilute surfactant solutions. Europhys Lett 54:605–611
80. Bandyopadhyay R, Basappa G, Sood AK (2000) Observation of chaotic dynamics in dilute sheared aqueous solutions of ctat. Phys Rev Lett 84(9):2022–2025
81. Macias ER, Bautista F, Soltero JFA, Puig JE, Attane P, Manero O (2003) On the shear thickening flow of dilute ctat wormlike micellar solutions. J Rheol 47(3):643–658
82. Torres MF, Gonzalez JM, Rojas MR, Muller AJ, Saez AE, Lof D, Schillen K (2007) Effect of ionic strength on the rheological behavior of aqueous cetyltrimethylammonium p-toluene sulfonate solutions. J Colloid Interface Sci 307(1):221–228
83. Lu B, Li X, Scriven L, Davis H, Talmon Y, Zakin J (1998) Effect of chemical structure on viscoelasticity and extensional viscosity of drag-reducing cationic surfactant solutions. Langmuir 14:8–16
84. Qi Y, Zakin J (2002) Chemical and rheological characterization of drag-reducing cationic surfactant systems. Ind Eng Chem Res 41(25):6326–6336
85. Hofmann S, Rauscher A, Hoffmann H (1991) Shear induced micellar structures. Ber Bunsenges Phys Chem 95(2):153–164
86. Hu Y, Wang S, Jamieson A (1993a) Kinetic studies of a shear thickening micellar solution. J Colloid Interface Sci 156(1):31–37
87. Prötzl B, Springer J (1997) Light scattering experiments on shear induced structures of micellar solutions. J Colloid Interface Sci 190:327–333
88. Schmitt V, Schosseler F, Lequeux F (1995b) Structure of salt-free wormlike micelles – signature by sans at rest and under shear. Europhys Lett 30(1):31–36
89. Oda R, Panizzza P, Schmutz M, Lequeux F (1997) Direct evidence of the shear-induced structure of wormlike micelles: gemini 12-2-12. Langmuir 13:6407–6412
90. Oda R, Weber V, Lindner P, Pine D, Mendes E, Schloesser F (2000) Time-resolved small-angle neutron scattering study of shear-thickening surfactant solutions after the cessation of flow. Langmuir 14:4859–4863
91. Weber V, Schosseler F (2002) Shear-thickening in salt-free aqueous solutions of a gemini cationic surfactant: A study by small angle light scattering. Langmuir 18(25):9705–9712
92. Weber V, Narayanan T, Mendes E, Schosseler F (2003) Micellar growth in salt-free aqueous solutions of a gemini cationic surfactant: evidence for a multimodal population of aggregates. Langmuir 19(4):992–1000

93. Oelschlaeger C, Waton G, Candau SJ, Cates ME (2002b) Structural, kinetics, and rheological properties of low ionic strength dilute solutions of a dimeric (gemini) surfactant. Langmuir 18(20):7265–7271
94. Oda R, Lequeux F, Mendes E (1996) Evidence for local orientational order in salt-free wormlike micelles: a transient electric birefingence study. J Phys II France 6:1429–1439
95. Oda R, Narayanan J, Hassan P, Manohar C, Salkar R, Kern F, Candau S (1998) Effect of the lipophilicity of the counterion on the viscoelasticity of micellar solutions of cationic surfactant. Langmuir 14:4364–4372
96. Hu YT, Boltenhagen P, Pine DJ (1998b) Shear thickening in low-concentration solutions of wormlike micelles. i. direct visualization of transient behavior and phase transitions. J Rheol 42(5):1185–1208
97. Myska J, Stern P (1994) Properties of drag reducing micelle system. Colloid Polym Sci 272:542–547
98. Boltenhagen P, Hu YT, Matthys EF, Pine DJ (1997a) Inhomogeneous structure formation and shear-thickening in wormlike micellar solutions. Eur Phys Lett 38(5):389–394
99. Hu YT, Boltenhagen P, Matthys E, Pine DJ (1998a) Shear thickening in low-concentration solutions of wormlike micelles. ii. slip, fracture, and stability of the shear-induced phase. J Rheol 42(5):1209–1226
100. In M, Aguerre-Chariol O, Zana R (1999a) Closed-looped micelles in surfactant tetramer solutions. J Phys Chem B 103:7747–7750
101. In M, Aguerre-Chariol O, Zana R (1999b) Dynamics of branched threadlike micelles. Phys Rev lett 83:2278–2281
102. Lin Z, Zheng Y, Davis H, Scriven L, Talmon Y, Zakin J (2000) Unusual effects of counterion to surfactant concentration ratio on viscoelasticity of a cationic surfactant drag reducer. J Non-Newt Fluid Mech 93:363–373
103. Truong M, Walker L (2000) Controlling the shear-induced structural transition of rodlike micelles using nonionic polymer. Langmuir 16:7991–7998
104. Lee JY, Magda JJ, Hu H, Larson RG (2002) Cone angle effects, radial pressure profile, and second normal stress difference for shear-thickening wormlike micelles. J Rheol 46(1):195–208
105. Keller S, Boltenhagen P, Pine D, Zasadzinski J (1997) Direct observation of shear-induced structures in wormlike micellar solutions by freeze-fracture electron microscopy. Phys Rev Lett 80:2725–2728
106. Hoffmann H, Platz G, Rehage H, Schorr W (1981a) The influence of counter-ion concentration on the aggregation behaviour of viscoelastic detergents. Ber Bunsenges Phys Chem 85:877–882
107. Oelschlaeger C, Waton G, Candau S, Cates M (2002a) Structural, kinetics, and rheological properties of low ionic strength dilute solutions of a dimeric (gemini) surfactant. Langmuir 18(20):7265–7271
108. Berret JF, Gamez-Corrales R, Oberdisse J, Walker LM, Lindner P (1998a) Flow-structure relationship of shear-thickening surfactant solutions. Europhys Lett 41:677–682
109. Deutsch M (1991) Orientational order determination in liquid crystals by X-ray diffraction. Phys Rev A 44:8264–8270
110. Barentin C, Liu AJ (2001) Shear thickening in dilute solutions of wormlike micelles. Europhys Lett 55:432–438
111. Schmitt V, Lequeux F (1995) SANS spectra and elastic plateau modulus in a charged wormlike micelles solution – effect of salt. J Phys II (France) 5(2):193–197
112. Larson R (1999) The Structure and rheology of complex fluids. New York University press, New York
113. Larson R (1992) Instabilities in viscoelastic flows. Rheol Acta 31:213–263
114. Ajdari A (1998) Rheological behavior of a solution of particles aggregating on the containing walls. Phys Rev E 58(4):6294–6298
115. Goveas JL, Pine D (1999) A phenomenological model for shear-thickening in wormlike micelle solutions. Europhys Lett 48:706–712

116. Cates M, Turner M (1990) Flow-induced gelation of rodlike micelles. Europhys Lett 7: 681–686
117. Bruinsma R, Gelbart W, Ben-Shaul A (1992) Flow-induced gelation of living (micellar) polymers. J Chem Phys 96:7710–7727
118. Turner M, Cates M (1992) Flow-induced phase transition in rodlike micelles. J Phys Condens Matter 4:3719–3741
119. Cates ME, Fielding SM (2006) Rheology of giant micelles. Adv Phys 55(7–8):799–879
120. Olmsted PD (2008) Perspectives on shear-banding in complex fluids. Rheol Acta 47(3):283–300
121. Salmon JB, Manneville S, Colin A (2003b) Shear banding in a lyotropic lamellar phase. I. Time-averaged velocity profiles. Phys Rev E 68(5):051503
122. Salmon JB, Manneville S, Colin A (2003c) Shear banding in a lyotropic lamellar phase. II. Temporal fluctuations. Phys Rev E 68(5):051504
123. Berret JF, Serero Y (2001) Evidence of shear-induced fluid fracture in telechelic polymer networks. Phys Rev Lett 87(4):048303
124. Manneville S, Colin A, Waton G, Schosseler F (2007) Wall slip, shear banding, and instability in the flow of a triblock copolymer micellar solution. Phys Rev E 75(6):061502
125. Lettinga MP, Dhont JKG (2004) Non-equilibrium phase behaviour of rodlike viruses under shear flow. J Phys Cond Matt 16(38):S3929–S3939
126. Pujolle-Robic C, Noirez L (2001) Observation of shear-induced nematic-isotropic transition in side-chain liquid crystal polymers. Nature 409(6817):167–171
127. Volkova O, Cutillas S, Bossis G (1999) Shear banded flows and nematic-to-isotropic transition in ER and MR fluids. Phys Rev Lett 82(1):233–236
128. Coussot P, Raynaud JS, Bertrand F, Moucheront P, Guilbaud JP, Huynh HT, Jarny S, Lesueur D (2002) Coexistence of liquid and solid phases in flowing soft-glassy materials. Phys Rev Lett 88(21):218301
129. Losert W, Bocquet L, Lubensky TC, Gollub JP (2000) Particle dynamics in sheared granular matter. Phys Rev Lett 85(7):1428–1431
130. Mueth DM, Debregeas GF, Karczmar GS, Eng PJ, Nagel SR, Jaeger HM (2000) Signatures of granular microstructure in dense shear flows. Nature 406(6794):385–389
131. Debregeas G, Tabuteau H, di Meglio JM (2001) Deformation and flow of a two-dimensional foam under continuous shear. Phys Rev Lett 87(17):178305
132. Lauridsen J, Chanan G, Dennin M (2004) Velocity profiles in slowly sheared bubble rafts. Phys Rev Lett 93(1):018303
133. Gilbreth C, Sullivan S, Dennin M (2006) Flow transitions in two-dimensional foams. Phys Rev E 74(5):051406
134. Cates ME, McLeish TCB, Marrucci G (1993) The rheology of entangled polymers at very high shear rates. Europhys Lett 21(4):451–456
135. Callaghan PT, Cates ME, Rofe CJ, Smeulders J (1996) A study of the "spurt effect" in wormlike micelles using nuclear magnetic resonance microscopy. J Phys II 6(3):375–393
136. Rehage H, Hoffmann H (1988b) Rheological properties of viscoelastic surfactant systems. J Phys Chem 92(16):4712–4719
137. Berret JF, Porte G, Decruppe JP (1997) Inhomogeneous shear flows of wormlike micelles: a master dynamic phase diagram. Phys Rev E 55(2):1668–1676
138. Berret JF (1997) Transient rheology of wormlike micelles. Langmuir 13(8):2227–2234
139. Britton MM, Mair RW, Lambert RK, Callaghan PT (1999) Transition to shear banding in pipe and couette flow of wormlike micellar solutions. J Rheol 43(4):897–909
140. Grand C, Arrault J, Cates ME (1997) Slow transients and metastability in wormlike micelle rheology. J Phys II 7(8):1071–1086
141. Mendez-Sanchez AF, Lopez-Gonzalez MR, Rolon-Garrido VH, Perez-Gonzalez J, de Vargas L (2003a) Instabilities of micellar systems under homogeneous and non-homogeneous flow conditions. Rheol Acta 42(1–2):56–63
142. Schmitt V, Marques CM, Lequeux F (1995a) Shear-induced phase-separation of complex fluids – the role of flow-concentration coupling. Phys Rev E 52(4):4009–4015

143. Fielding SM, Olmsted PD (2003) Flow phase diagrams for concentration-coupled shear banding. Eur Phys J E 11(1):65–83
144. Lerouge S, Decruppe JP, Berret JF (2000) Correlations between rheological and optical properties of a micellar solution under shear banding flow. Langmuir 16(16):6464–6474
145. Mair RW, Callaghan PT (1996) Observation of shear banding in wormlike micelles by nmr velocity imaging. Eur Phys Lett 36(9):719–724
146. Mair RW, Callaghan PT (1997) Shear flow of wormlike micelles in pipe and cylindrical Couette geometries as studied by nuclear magnetic resonance microscopy. J Rheol 41(4):901–924
147. Britton MM, Callaghan PT (1997a) Nuclear magnetic resonance visualization of anomalous flow in cone-and-plate rheometry. J Rheol 41(6):1365–1386
148. Britton MM, Callaghan PT (1997b) Two-phase shear band structures at uniform stress. Phys Rev Lett 78(26):4930–4933
149. Fischer P, Rehage H (1997) Non-linear flow properties of viscoelastic surfactant solutions. Rheol Acta 36(1):13–27
150. Britton MM, Callaghan PT (1999) Shear banding instability in wormlike micellar solutions. Eur Phys J B 7(2):237–249
151. Porte G, Berret JF, Harden JL (1997) Inhomogeneous flows of complex fluids: mechanical instability versus non-equilibrium phase transition. J Phys II 7(3):459–472
152. Mendez-Sanchez AF, Perez-Gonzalez J, de Vargas L, Castrejon-Pita JR, Castrejon-Pita AA, Huelsz G (2003b) Particle image velocimetry of the unstable capillary flow of a micellar solution. J Rheol 47(6):1455–1466
153. Lee JY, Fuller GG, Hudson NE, Yuan XF (2005) Investigation of shear-banding structure in wormlike micellar solution by point-wise flow-induced birefringence measurements. J Rheol 49(2):537–550
154. Forster S, Konrad M, Lindner P (2005) Shear thinning and orientational ordering of wormlike micelles. Phys Rev Lett 94(1)
155. Manneville S, Salmon JB, Bécu L, Colin A, Molino F (2004b) Inhomogeneous flows in sheared complex fluids. Rheol Acta 43(5):408–416
156. Salmon JB, Colin A, Manneville S, Molino F (2003a) Velocity profiles in shear-banding wormlike micelles. Phys Rev Lett 90(22):228303
157. Hu YT, Lips A (2005) Kinetics and mechanism of shear banding in an entangled micellar solution. J Rheol 49(5):1001–1027
158. Miller E, Rothstein JP (2007) Transient evolution of shear-banding wormlike micellar solutions. J Non-Newt Fluid Mech 143(1):22–37
159. Holmes WM, Lopez-Gonzalez MR, Callaghan PT (2003) Fluctuations in shear-banded flow seen by nmr velocimetry. Eur Phys Lett 64(2):274–280
160. Lopez-Gonzalez MR, Holmes WM, Callaghan PT, Photinos PJ (2004) Shear banding fluctuations and nematic order in wormlike micelles. Phys Rev Lett 93(26):268302
161. Lopez-Gonzalez MR, Holmes WM, Callaghan PT (2006) Rheo-nmr phenomena of wormlike micelles. Soft Matter 2(10):855–869
162. Ballesta P, Lettinga MP, Manneville S (2007) Superposition rheology of shear-banding wormlike micelles. J Rheol 51(5):1047–1072
163. Ballesta P, Manneville S (2005) Signature of elasticity in the faraday instability. Phys Rev E 71:026308
164. Ballesta P, Manneville S (2007) The faraday instability in wormlike micelle solutions. J Non-Newt Fluid Mech 147(1–2):23–34
165. Masselon C, Salmon JB, Colin A (2008) Nonlocal effects in flows of wormlike micellar solutions. Phys Rev Lett 1(3):38301
166. Cappelaere E, Cressely R, Decruppe JP (1995) Linear and nonlinear rheological behavior of salt-free aqueous ctab solutions. Colloids Surf A Physicochem Eng Asp 104(2-3):353–374
167. Decruppe JP, Cressely R, Makhloufi R, Cappelaere E (1995) Flow birefringence experiments showing a shear-banding structure in a CTAB solution. Coll and Polym Sci 273(4):346–351
168. Cappelaere E, Berret JF, Decruppe JP, Cressely R, Lindner P (1997) Rheology, birefringence, and small-angle neutron scattering in a charged micellar system: evidence of a shear-induced phase transition. Phys Rev E 56(2):1869–1878

169. Fischer E, Callaghan PT (2000) Is a birefringence band a shear band? Europhys Lett 50(6):803–809
170. Fischer E, Callaghan PT (2001) Shear banding and the isotropic-to-nematic transition in wormlike micelles. Phys Rev E 64(1):011501
171. Bécu L, Manneville S, Colin A (2004) Spatiotemporal dynamics of wormlike micelles under shear. Phys Rev Lett 93(1):018301
172. Bécu L, Anache D, Manneville S, Colin A (2007) Evidence for three-dimensional unstable flows in shear-banding wormlike micelles. Phys Rev E 76(1):011503
173. Schmitt V, Lequeux F, Pousse A, Roux D (1994) Flow behavior and shear-induced transition near an isotropic-nematic transition in equilibrium polymers. Langmuir 10(3):955–961
174. Shikata T, Dahman SJ, Pearson DS (1994) Rheooptical behavior of wormlike micelles. Langmuir 10(10):3470–3476
175. Shikata T, Pearson DS (1994) Phase-transitions in entanglement networks of wormlike micelles. Langmuir 10(11):4027–4030
176. Fischer P, Fuller GG, Lin ZC (1997) Branched viscoelastic surfactant solutions and their response to elongational flow. Rheol Acta 36(6):632–638
177. Lerouge S, Decruppe JP, Humbert C (1998) Shear banding in a micellar solution under transient flow. Phys Rev Lett 81(24):5457–5460
178. Kadoma IA, vanEgmond JW (1996) "Tuliplike" scattering patterns in wormlike micelles under shear flow. Phys Rev Lett 76(23):4432–4435
179. Wheeler EK, Izu P, Fuller GG (1996) Structure and rheology of wormlike micelles. Rheol Acta 35(2):139–149
180. Kadoma IA, vanEgmond JW (1997) Shear-enhanced orientation and concentration fluctuations in wormlike micelles: effect of salt. Langmuir 13(17):4551–4561
181. Kadoma IA, Ylitalo C, vanEgmond JW (1997) Structural transitions in wormlike micelles. Rheol Acta 36(1):1–12
182. Kadoma IA, van Egmond JW (1998) Flow-induced nematic string phase in semidilute wormlike micelle solutions. Phys Rev Lett 80(25):5679–5682
183. Azzouzi H, Decruppe JP, Lerouge S, Greffier O (2005) Temporal oscillations of the shear stress and scattered light in a shear-banding-shear-thickening micellar solution. Eur Phys J E 17(4):507–514
184. Hashimoto T, Turukawa T, Mori N (2005) Flow property and micellar structures in capillary flows of surfactant solutions. Nihon Reoroji Gakkaishi 33(1):1–8
185. Inoue T, Inoue Y, Watanabe H (2005) Nonlinear rheology of ctab/nasal aqueous solutions: finite extensibility of a network of wormlike micelles. Langmuir 21(4):1201–1208
186. Drappier J, Bonn D, Meunier J, Lerouge S, Decruppe JP, Bertrand F (2006) Correlation between birefringent bands and shear bands in surfactant solutions. J Stat Mech-Theory Exp P04003
187. Decruppe JP, Greffier O, Manneville S, Lerouge S (2006) Local velocity measurements in heterogeneous and time-dependent flows of a micellar solution. Phys Rev E 73(6):061509
188. Decruppe JP, Cappelaere E, Cressely R (1997) Optical and rheological properties of a semidiluted equimolar solution of cetyltrimethylammonium bromide and potassium bromide. J Phys II (France) 7(2):257–270
189. Humbert C, Decruppe JP (1998b) Stress optical coefficient of viscoelastic solutions of cetyltrimethylammonium bromide and potassium bromide. Colloid Polym Sci 276(2):160–168
190. Radulescu O, Olmsted PD, Decruppe JP, Lerouge S, Berret JF, Porte G (2003) Time scales in shear banding of wormlike micelles. Europhys Lett 62(2):230–236
191. Lerouge S, Decruppe JP, Olmsted P (2004) Birefringence banding in a micellar solution or the complexity of heterogeneous flows. Langmuir 20(26):11,355–11,365
192. Cappelaere E, Cressely R (1997) Shear banding structure in viscoelastic micellar solutions. Colloid Polym Sci 275(5):407–418
193. Cappelaere E, Cressely R (1998) Rheological behavior of an elongated micellar solution at low and high salt concentrations. Colloid Polym Sci 276(11):1050–1056

194. Decruppe JP, Lerouge S, Berret JF (2001) Insight in shear banding under transient flow. Phys Rev E 63(2):022501
195. Lerouge S, Argentina M, Decruppe JP (2006) Interface instability in shear-banding flow. Phys Rev Lett 96(8):088301
196. Lerouge S, Fardin M, Argentina M, Gregoire G, Cardoso O (2008) Interface dynamics in shear-banding flow of giant micelles. Soft Matter 4(9):1808–1819
197. Berret JF, Roux DC, Porte G, Lindner P (1994b) Shear-induced isotropic-to-nematic phase-transition in equilibrium polymers. Europhys Lett 25(7):521–526
198. Berret JF, Roux DC, Lindner P (1998b) Structure and rheology of concentrated wormlike micelles at the shear-induced isotropic-to-nematic transition. Eur Phys J B 5(1):67–77
199. Berret JF, Porte G (1999) Metastable versus unstable transients at the onset of a shear-induced phase transition. Phys Rev E 60(4):4268–4271
200. Ganapathy R, Sood AK (2006a) Intermittency route to rheochaos in wormlike micelles with flow-concentration coupling. Phys Rev Lett 96(10):108301
201. Soltero JFA, Puig JE, Manero O, Schulz PC (1995) Rheology of cetyltrimethylammonium tosilate-water system .1. relation to phase-behavior. Langmuir 11(9):3337–3346
202. Soltero JFA, Puig JE, Manero O (1996) Rheology of cetyltrimethylammonium tosylate-water system .2. linear viscoelastic regime. Langmuir 12(9):2654–2662
203. Soltero JFA, Bautista F, Puig JE, Manero O (1999) Rheology of cetyltrimethylammonium p-toluenesulfonate-water system. 3. nonlinear viscoelasticity. Langmuir 15(5):1604–1612
204. Hernandez-Acosta S, Gonzalez-Alvarez A, Manero O, Sanchez AFM, Perez-Gonzalez J, de Vargas L (1999) Capillary rheometry of micellar aqueous solutions. J Non-Newt Fluid Mech 85(2–3):229–247
205. Bautista F, Soltero JFA, Macias ER, Puig JE, Manero O (2002) Irreversible thermodynamics approach and modeling of shear-banding flow of wormlike micelles. J Phys Chem B 106(50):13018–13026
206. Bandyopadhyay R, Sood AK (2003) Effect of screening of intermicellar interactions on the linear and nonlinear rheology of a viscoelastic gel. Langmuir 19(8):3121–3127
207. Ganapathy R, Sood AK (2006b) Tuning rheochaos by temperature in wormlike micelles. Langmuir 22(26):11,016–11,021
208. Makhloufi R, Decruppe JP, Aït-Ali A, Cressely R (1995) Rheooptical study of wormlike micelles undergoing a shear banding flow. Europhys Lett 32(3):253–258
209. Aït-Ali A, Makhloufi R (1997a) Linear and nonlinear rheology of an aqueous concentrated system of cetyltrimethylammonium chloride and sodium salicylate. Phys Rev E 56(4):4474–4478
210. Aït-Ali A, Makhloufi R (1997b) On the nonlinear rheology of wormlike micellar system in the presence of sodium salicylate salt. J Rheol 41(2):307–318
211. Decruppe JP, Ponton A (2003) Flow birefringence, stress optical rule and rheology of four micellar solutions with the same low shear viscosity. Eur Phys J E 10(3):201–207
212. Escalante JI, Macias ER, Bautista F, Perez-Lopez JH, Soltero JFA, Puig JE, Manero O (2003) Shear-banded flow and transient rheology of cationic wormlike micellar solutions. Langmuir 19(17):6620–6626
213. Angelescu D, Khan A, Caldararu H (2003) Viscoelastic properties of sodium dodecyl sulfate with aluminum salt in aqueous solution. Langmuir 19(22):9155–9161
214. Schubert BA, Wagner NJ, Kaler EW, Raghavan SR (2004) Shear-induced phase separation in solutions of wormlike micelles. Langmuir 20(9):3564–3573
215. Raghavan SR, Kaler EW (2001) Highly viscoelastic wormlike micellar solutions formed by cationic surfactants with long unsaturated tails. Langmuir 17(2):300–306
216. Hassan PA, Valaulikar BS, Manohar C, Kern F, Bourdieu L, Candau SJ (1996) Vesicle to micelle transition: rheological investigations. Langmuir 12(18):4350–4357
217. Koehler RD, Raghavan SR, Kaler EW (2000) Microstructure and dynamics of wormlike micellar solutions formed by mixing cationic and anionic surfactants. J Phys Chem B 104(47):11,035–11,044
218. Schubert BA, Kaler EW, Wagner NJ (2003) The microstructure and rheology of mixed cationic/anionic wormlike micelles. Langmuir 19(10):4079–4089

219. Mu JH, Li GZ, Jia XL, Wang HX, Zhang GY (2002) Rheological properties and microstructures of anionic micellar solutions in the presence of different inorganic salts. J Phys Chem B 106(44):11,685–11,693
220. Pimenta P, Pashkovski EE (2006) Rheology of viscoelastic mixed surfactant solutions: effect of scission on nonlinear flow and rheochaos. Langmuir 22(9):3980–3987
221. Soltero JFA, Alvarez-Ramirez JG, Fernandez VVA, Tepale N, Bautista F, Macias ER, Perez-Lopez JH, Schulz PC, Manero O, Solans C, Puig JE (2007) Phase and rheological behavior of the polymerizable surfactant CTAVB and water. J Colloid Interface Sci 312(1):130–138
222. Wheeler EK, Fischer P, Fuller GG (1998) Time-periodic flow induced structures and instabilities in a viscoelastic surfactant solution. J Non-Newt Fluid Mech 75(2–3):193–208
223. Fielding SM (2005) Linear instability of planar shear banded flow. Phys Rev Lett 95(13):134501
224. Fielding SM (2007b) Vorticity structuring and velocity rolls triggered by gradient shear bands. Phys Rev E 76(1):016311
225. Fielding SM (2007a) Complex dynamics of shear-banding flows. Soft Matter 3(1):1262–1279
226. Fischer P, Wheeler EK, Fuller GG (2002) Shear-banding structure orientated in the vorticity direction observed for equimolar micellar solution. Rheol Acta 41(1–2):35–44
227. Herle V, Fischer P, Windhab EJ (2005) Stress driven shear bands and the effect of confinement on their structures – a rheological, flow visualization, and rheo-sals study. Langmuir 21(20):9051–9057
228. Herle V, Kohlbrecher J, Pfister B, Fischer P, Windhab EJ (2007) Alternating vorticity bands in a solution of wormlike micelles. Phys Rev Lett 99(15):158,302
229. Herle V, Manneville S, Fischer P (2008) Alternating vorticity bands in a solution of wormlike micelles. Eur Phys J E 26(1):3–12
230. Marin-Santibanez BM, Perez-Gonzalez J, de Vargas L, Rodriguez-Gonzalez F, Huelsz G (2006) Rheometry – piv of shear-thickening wormlike micelles. Langmuir 22(9):4015–4026
231. Jindal V, Kalus J, Pilsl H, Hoffmann H, Lindner P (1990) Dynamic small angle neutron scattering study of rodlike micelles in surfactant solutions. J Phys Chem 94(7):3129–3138
232. Larson R (1988) Constitutive equations for polymer melt and solutions. Butterworth-Heinemann, UK
233. Menezes E, Graessley W (1982) Nonlinear rheological behavior of polymer systems for several shear-flow histories. J Polym Sci 20(10):1817–1833
234. Spenley NA, Yuan XF, Cates ME (1996) Nonmonotonic constitutive laws and the formation of shear-banded flows. J Phys II 6(4):551–571
235. Olmsted PD, Lu CYD (1997) Coexistence and phase separation in sheared complex fluids. Phys Rev E 56(1):R55–R58
236. Ganapathy R, Sood AK (2008) Nonlinear flow of wormlike micellar gels: regular and chaotic time-dependence of stress, normal force and nematic ordering. J Non-Newt Fluid Mech 149(1–3):78–86
237. Ott E (1993) Chaos in dynamical systems. Cambridge University Press, England
238. Fielding SM, Olmsted PD (2004) Spatiotemporal oscillations and rheochaos in a simple model of shear banding. Phys Rev Lett 92(8):084502
239. Bandyopadhyay R, Sood AK (2001) Chaotic dynamics in shear-thickening surfactant solutions. Europhys Lett 56(3):447–453
240. Salmon JB, Colin A, Roux D (2002) Dynamical behavior of a complex fluid near an out-of-equilibrium transition: approaching simple rheological chaos. Phys Rev E 66(3):031505
241. Manneville S, Salmon JB, Colin A (2004c) A spatio-temporal study of rheo-oscillations in a sheared lamellar phase using ultrasound. Eur Phys J E 13(2):197–212
242. Wunenburger AS, Colin A, Leng J, Arneodo A, Roux D (2001) Oscillating viscosity in a lyotropic lamellar phase under shear flow. Phys Rev Lett 86(7):1374–1377
243. Courbin L, Panizza P, Salmon JB (2004) Observation of droplet size oscillations in a two-phase fluid under shear flow. Phys Rev Lett 92(1):018305
244. Lootens D, Van Damme H, Hebraud P (2003) Giant stress fluctuations at the jamming transition. Phys Rev Lett 90(17):178301

245. Manneville S (2008) Recent experimental probes of shear banding. Rheol Acta 47(3): 301–318
246. Callaghan PT (2008) Rheo nmr and shear banding. Rheol Acta 47(3):243–255
247. Salmon JB, Manneville S, Colin A, Pouligny B (2003d) An optical fiber based interferometer to measure velocity profiles in sheared complex fluids. Eur Phys J Appl Phys 22(2):143–154
248. Manneville S, Bécu L, Colin A (2004a) High-frequency ultrasonic speckle velocimetry in sheared complex fluids. Eur Phys J Appl Phys 28(3):361–373
249. Callaghan PT (2006) Rheo-nmr and velocity imaging. Curr Opin Colloid Interface Sci 11(1):13–18
250. Holmes WM, Lopez-Gonzalez MR, Callaghan PT (2004) Shear-induced constraint to amphiphile chain dynamics in wormlike micelles. Eur Phys Lett 66(1):132–138
251. Greco F, Ball RC (1997) Shear-band formation in a non-newtonian fluid model with a constitutive instability. J Non-Newt Fluid Mech 69(2–3):195–206
252. Olmsted PD, Radulescu O, Lu CYD (2000) Johnson-Segalman model with a diffusion term in cylindrical couette flow. J Rheol 44(2):257–275
253. Raudsepp A, Callaghan PT (2008) A rheo-optical study of shear rate and optical anisotropy in wormlike micelles solutions. Soft Matter 4(4):784–796
254. Fuller G (1995) Rheology of wormlike micelles: equilibrium properties and shear-banding transition In: Optical rheometry of complex fluids, Oxford University Press, New York
255. Humbert C, Decruppe JP (1998a) Flow birefringence and stress optical law of viscoelastic solutions of cationic surfactants and sodium salicylate. Eur Phys J B 6(4):511–518
256. Callaghan PT (1999) Rheo-nm nuclear magnetic resonance and the rheology of complex fluids. Rep on Prog in Phys 62(4):599–670
257. Helfand E, Fredrickson GH (1989) Large fluctuations in polymer-solutions under shear. Phys Rev Lett 62(21):2468–2471
258. Liberatore MW, Nettesheim F, Wagner NJ, Porcar L (2006) Spatially resolved small-angle neutron scattering in the 1-2 plane: a study of shear-induced phase-separating wormlike micelles. Phys Rev E 73(2):020504
259. Hilliou L, Vlassopoulos D (2002) Time-periodic structures and instabilities in shear-thickening polymer solutions. Ind Eng Chem Res 41(25):6246–6255
260. Dhont JKG, Lettinga MP, Dogic Z, Lenstra TAJ, Wang H, Rathgeber S, Carletto P, Willner L, Frielinghaus H, Lindner P (2003) Shear-banding and microstructure of colloids in shear flow. Faraday Discuss 123:157–172
261. Kang KG, Lettinga MP, Dogic Z, Dhont JKG (2006) Vorticity banding in rodlike virus suspensions. Phys Rev E 74(2):026307
262. Cates ME (1990) Nonlinear viscoelasticity of wormlike micelles (and other reversibly breakable polymers). J Phys Chem 94(1):371–375
263. Olmsted PD, Goldbart P (1990) Theory of the nonequilibrium phase-transition for nematic liquid-crystals under shear-flow. Phys Rev A 41(8):4578–4581
264. Dhont JKG (1999) A constitutive relation describing the shear-banding transition. Phys Rev E 60(4):4534–4544
265. Olmsted PD (1999a) Dynamics and flow-induced phase separation in polymeric fluids. Curr Opin Colloid Inter Sci 4(2):95–100
266. Radulescu O, Olmsted PD, Lu CYD (1999) Shear banding in reaction-diffusion models. Rheol Acta 38(6):606–613
267. Yuan XF (1999) Dynamics of a mechanical interface in shear-banded flow. Eur Phys Lett 46(4):542–548
268. Lu CYD, Olmsted PD, Ball RC (2000) Effects of nonlocal stress on the determination of shear banding flow. Phys Rev Lett 84(4):642–645
269. Radulescu O, Olmsted PD (2000) Matched asymptotic solutions for the steady banded flow of the diffusive johnson-segalman model in various geometries. J Non-Newt Fluid Mech 91(2–3):143–164
270. Adams J, Fielding S, Olmsted PD (2008) The interplay between boundary conditions and flow geometries in shear banding : hysteresis, band configurations, and surface transitions. J Non-Newt Fluid Mech 151(3):101–118

271. Olmsted PD (1999b) Two-state shear diagrams for complex fluids in shear flow. Europhys Lett 48(3):339–345
272. Aradian A, Cates ME (2005) Instability and spatiotemporal rheochaos in a shear-thickening fluid model. Eur Phys Lett 70(3):397–403
273. Aradian A, Cates ME (2006) Minimal model for chaotic shear banding in shear thickening fluids. Phys Rev E 73(4):041508
274. Wilson HJ (2006) Instabilities and constitutive modelling. Philos Trans R Soc A 364(1849):3267–3283
275. Fielding SM, Olmsted PD (2006) Nonlinear dynamics of an interface between shear bands. Phys Rev Lett 96(10):104502
276. Oswald P, Pieranski P (2000) Les cristaux liquides. Gordon and Breach, Amsterdam
277. Onsager L (1949) The effects of shape on the interaction of colloidal particles. Ann NY Acad Sci 51:627–649
278. Leadbetter A, Wrighton P (1979) Order parameters in sa, sc and n phases by X-ray diffraction. J Phys C3 40:234–242
279. Lawson K, Flautt T (1967) Magnetically oriented lyotropic liquid crystalline phase. J Am Chem Soc 89:5489–5491
280. Itri R, Amaral L (1990) Study of the isotropic-hexagonal transition in the system SLS/H2O. J Phys Chem 94:2198–2202
281. Quist PO, Halle B, Furo I (1992) Micelle size and order in lyotropic nematic phases from nuclear spin relaxation. J Chem Phys 96:3875–3891
282. Itri R, Amaral L (1993) Micellar-shape anisometry near isotropic-liquid-crystal phase transition. Phys Rev E 47:2551–2557
283. Berret JF, Roux DC (1995) Rheology of nematic wormlike micelles. J Rheol 39(4):725–741
284. Thiele T, Berret JF, Muller S, Schmidt C (2001) Rheology and nuclear magnetic resonance measurements under shear of sodium dodecyl sulfate/decanol/water nematics. J Rheol 45(1):29–48
285. Clawson JS, Holland GP, Alam TM (2006) Magnetic alignment of aqueous ctab in nematic and hexagonal liquid crystalline phases investigated by spin-1 nmr. Phys Chem Chem Phys 8(22):2635–2641
286. De Melo Filho AA, Amadeu NS, Fujiwara FY (2007) The phase diagram of the lyotropic nematic mesophase in the ttab/nabr/water system. Liq Crys 34(6):683–691
287. Chen DM, Fujiwara FY, Reeves LW (1977) Studies of behavior in magnetic-fields of some lyomesophase systems with respect to electrolyte additions. Can J Chem-Rev Can Chim 55(12):2396–2403
288. Hendrikx Y, Charvolin J (1981) Structural relations between lyotropic phases in the vicinity of the nematic phases. J Phys 42:1427–1440
289. Hendrikx Y, Charvolin J, Rawiso M, Liebert L, Holmes M (1983) Anisotropic aggregates of amphiphilic molecules in lyotropic nematic phases. J Phys Chem 87:3991–3999
290. Caputo FE, Ugaz VM, Burghardt WR, Berret JF (2002) Transient 1-2 plane small-angle X-ray scattering measurements of micellar orientation in aligning and tumbling nematic surfactant solutions. J Rheol 46(4):927–946
291. Semenov A, Khokhlov A (1988) Statistical physics of liquid-crystalline polymers. Sov Phys Usp 31:988–1014
292. Khokhlov A, Semenov A (1981) Liquid-crystalline ordering in the solution of long persistent chains. Physica A 108:546–556
293. Richtering W, Laeuger J, Linemann R (1994) Shear orientation of a micellar hexagonal liquid crystalline phase: a rheo and small angle light scattering study. Langmuir 10(11):4374–4379
294. Lukaschek M, Grabowski D, Schmidt C (1995) Shear-induced alignment of a hexagonal lyotropic liquid crystal as studied by rheo-nmr. Langmuir 11(9):3590–3594
295. Muller S, Fischer P, Schmidt C (1997) Solid-like director reorientation in sheared hexagonal lyotropic liquid crystals as studied by nuclear magnetic resonance. J Phys II France 7:421–432
296. Schmidt G, Muller S, Lindner P, Schmidt C, Richtering W (1998) Shear orientation of lyotropic hexagonal phases. J Phys Chem B 102(3):507–513

297. Schmidt C (2008) Rheo-nmr spectroscopy. Modern Magnetic Resonance 3:1515–1521
298. Ramos L, Molino F, Porte G (2000) Shear melting in lyotropic hexagonal phases. Langmuir 16(14):5846–5848
299. Ramos L (2001) Scaling with temperature and concentration of the nonlinear rheology of a soft hexagonal phase. Phys Rev E 64(6):061502
300. Ramos L, Molino F (2004) Shear melting of a hexagonal columnar crystal by proliferation of dislocations. Phys Rev Lett 92(1):018301
301. Roux DC, Berret JF, Porte G, Peuvrel-Disdier E, Lindner P (1995) Shear-induced orientations and textures of nematic wormlike micelles. Macromolecules 28(5):1681–1687
302. Berret JF, Roux DC, Porte G, Lindner P (1995) Tumbling behavior of nematic wormlike micelles under shear-flow. Europhys Lett 32(2):137–142
303. Caputo FE, Burghardt WR, Berret JF (1999) Tumbling dynamics in a nematic surfactant solution in transient shear flows. J Rheol 43(3):765–779
304. Burghardt W, Fuller G (1991) Role of director tumbling in the rheology of polymer liquid crystal solutions. Macromolecules 24(9):2546–2555
305. Moldenaers P, Yanase H, Mewis J (1991) Flow-induced anisotropy and its decay in polymeric liquid crystals. J Rheol 35(8):1681–1699
306. Larson R, Doi M (1991) Mesoscopic domain theory for textured liquid crystalline polymers. J Rheol 35:539–563
307. Srinivasarao M (1992) Rheology and rheo-optics of polymer liquid crystals: an overview of theory and experiment. Chemtracts Macromol Chem 3:149–178
308. Takahashi Y, Kurashima N, Noda I, Doi M (1994) Experimental tests of the scaling relation for textured materials in mixtures of two immiscible fluids. J Rheol 38(3):699–712
309. Thiele T, Berret JF, Mueller S, Schmidt C (1998) Rheology and nmr measurements on sds/decanol/water. In: 5th European Rheology Conference, Portoroz (Slovenia)
310. Doi M, Ohta T (1991) Dynamics and rheology of complex interfaces. I. J Chem Phys 95(2):1242–1248
311. Larson RG, Mead DW (1993) The ericksen number and deborah number cascades in sheared polymeric nematics. Liq Crys 15(2):151–169
312. Marrucci G (1985) Rheology of liquid crystalline polymers. Pure and Appl Chem 57:1545–1552
313. Larson R, Mead D (1992) Development of orientation and texture during shearing of liquid-crystalline polymers. Liq Cryst 12:751–768
314. Vermant J, Moldenaers P, Mewis J, Picken S (1994) Band formation upon cessation of flow in liquid-crystalline polymers. J Rheol 38:1571–1589
315. Noirez L, Lapp A (1997) Shear flow induced transition from liquid-crystalline to polymer behavior in side-chain liquid crystal polymers. Phys Rev lett 78:70–73
316. Zipfel J, Berghausen J, Lindner P, Richtering W (1999) Influence of shear on lyotropic lamellar phases with different membranes defects. J Phys Chem B 103:2841–2849
317. Berret JF, Vermant J, Noirez L (2000b) Lyotropic surfactant nematics under shear: neutron scattering in the vorticity plane. In: XIIIth international Congress on Rheology, Cambridge (UK), vol 3, pp 273–275
318. Ekwall P, Mandell L, Fontell K (1969) The cetyltrimethylammonium bromide-hexanol-water system. J Colloid Interface Sci 29(4):639–646
319. Hongladarom K, Burghardt W (1994) Measurements of the full refractive index tensor in sheared liquid-crystalline polymer solutions. Macromolecules 27:483–489
320. Grabowski D, Schmidt C (1994) Simultaneous measurements of shear viscosity and director orientation of a side-chain liquid crystalline polymer by rheo-NMR. Macromolecules 27:2632–2640
321. Siebert H, Grabowski D, Schmidt C (1997) Rheo-nmr study of non-flow-aligning side-chain liquid crystal polymer in nematic solution. Rheol Acta 36:618–627

Editor: J.-F. Joanny